Instituut voor Kern- en Stralingsfysica
Departement Natuurkunde en Sterrenkunde
Faculteit Wetenschappen

KATHOLIEKE UNIVERSITEIT
LEUVEN

Development of a Penning Trap based Set-up for Precision Tests of the Standard Model

Promotor:
Prof. Dr. N. Severijns

Proefschrift ingediend tot
het behalen van de graad van
doctor in de wetenschappen
door

Bavo Delauré

2004

Contents

List of Figures

Introduction

Ever since its discovery under the form of nuclear beta decay, the weak interaction has been shrouded in mystery, astonishment and excitement. In contrast to α and γ-decay the measured energy spectrum of the electron emitted in β-decay was not a mono-chromatic peak corresponding to the energy difference between the initial and final nuclear state but revealed a continuous distribution, violating the fundamental law of energy conservation. It was Pauli who postulated a massless, neutral spin 1/2-particle that would be emitted together with the beta particle, taking with it the missing energy. This undetectable particle saved conservation of energy and was given the name neutrino by Fermi. In 1956 Cowan *et al.* reported the direct detection of the neutrino, confirming the daring idea of Pauli.

Astonishment caught the physics community a second time shortly after. Lee and Yang noted in 1956 that no experiment had ever confirmed the weak interaction being unaffected by an inversion of the three spatial coordinates. Symmetry under the so-called parity operation was widely accepted and proven to be conserved in the other three fundamental interactions. The experiment of Wu *et al.* (1957) that measured the asymmetry of emitted β-particles with respect to the nuclear spin of ^{60}Co proved this common belief to be wrong.

At the end of the fifties the Conserved-Vector Current (CVC) theorem (Gell-Mann, 1958) suggested that there might be a link between the weak and the electromagnetic interaction. In the sixties Glashow, Weinberg and Salam (GWS) went one step further and proposed a unification scheme for the two interactions, which was shown to be renormalizable by 't Hooft in 1971 ('t Hooft, 1971a,b). The discovery of the $W^{\pm}$ and Z^0-gauge bosons by Rubbia at CERN in 1983 at the predicted masses was a persuasive evidence for the GWS model and can be considered as one of the greatest triumphs of modern physics.

Today the electroweak interaction is included together with the strong force in the Standard Model of particles and interactions, which has been highly successful over the last decades and agrees well with all experimental data. Still, it is generally believed not to be the ultimate theory describing nature and its forces. It contains a number of parameters that cannot be predicted by the model itself but have to be inserted from experimental data. Furthermore it does not answer fundamental questions like why/whether there are only three generations of leptons and quarks, what is the origin of parity violation, etc. leaving it unsatisfactory. At present a wide range of experiments is going on to test the Standard Model and search for new physics that would give a directional hint on how to improve it. Also the present experimental confirmation of the Vector minus Axial-vector (V-A) weak interaction adopted in the Standard Model still leaves room for exotic contributions like Scalar or Tensor interactions that appear in the most general Hamiltonian for nuclear beta decay as well as for a right-handed V+A interaction.

In the fifties and early sixties a lot of effort was spent on the study of the nature of the weak interaction by measuring the angular correlation between the β particle and the neutrino emitted in nuclear beta decay. The neutrino being hard to measure, this type of experiments needed a detection of the recoil nuclei, having however an energy of a few hundred eV at most. Besides scattering effects the recoil ions easily form chemical bindings with the host material of the source, complicating the measurement even more. Only a few successful experiments could be performed on the noble gas isotopes ^{6}He, ^{19}Ne, ^{23}Ne and ^{35}Ar being in gaseous state. This led in 1959 to the V-A determination of the weak interaction type (Allen *et al.*, 1959). Apart from a few experiments in the early sixties the attempts to improve the limits on possible Scalar and Tensor interaction components died a slow death.

Over the last decade the search for non-Standard Model contributions to the weak interaction has experienced a revival mainly triggered by two approaches to handle the problematic detection of low energy recoils.

First of all, in 1993 the experiment of Schardt and Riisager, performed at ISOLDE/CERN, showed that the broadening of the β-delayed proton peak following the superallowed $0^+ \rightarrow 0^+$ decay of ^{32}Ar was rather sensitive to the interaction type avoiding the need for direct detection of the recoil ion. This experiment was later on repeated in an improved version by Adelberger *et al.* (1999) yielding the current best limit of Scalar interaction of about 6% of the Vector strength at 68% CL.

The second and major boost for $\beta-\nu$ angular correlation measurements was of technological origin with the introduction of atom traps and ion traps (Paul and Penning) in the field of nuclear physics, after being used extensively already in atomic physics. Penning traps, for instance, entered the nuclear physics field in the beginning of the nineties in the scope of accurate mass measurements of radioactive isotopes and allowing the determination of nucleon binding energies. A pioneering role has been played in this respect by the ISOLTRAP mass spectrometer (Bollen *et al.*, 1996) at the ISOLDE/CERN-facility, where important technological developments were realized like the in-flight capture of externally produced ions in a Penning trap (Schnatz *et al.*, 1986) and the mass-selective buffer gas cooling technique (Savard *et al.*, 1991). Besides the achieved high accuracy mass determination, the storage features of the Penning trap opened new possibilities in the field of nuclear physics.

The Penning trap shares the capabilities with the Magneto-Optical atom Trap and the Paul trap of storing particles in a very well localized position in vacuum. In this way the difficulties in detecting the low energy recoils after beta decay that had been encountered in $\beta - \nu$ correlation measurements, could be overcome. At the same time the list of candidates, being restricted up to the nineties to mainly noble gases, could be extended now to alkali atoms in the case of atom traps and almost the whole chart of nuclides for ion traps. Over the last five years a number of new set-ups have been developed and taken into operation for measuring the $\beta - \nu$ correlation coefficient. It is expected that in the coming years a new boost of experimental data will allow to test the Standard Model V-A interaction at a more precise level and search for new physics beyond the Standard Model horizon.

WITCH, being the acronym for **W**eak **I**nteraction **T**rap for **CH**arged particles, is one of those new set-ups that have been designed for precision measurements of the $\beta - \nu$ angular correlation. This is realized by measuring the shape of the recoil energy of the daughter nuclei from nuclear β-decay. A scattering-free radioactive source is created by means of a Penning trap in a strong magnetic field. The recoil energy of the daughter nuclei is analyzed with a retardation spectrometer coupled to the Penning trap, forming a unique combination that has never been realized. The set-up is installed at ISOLDE/CERN which is the world leading facility when it comes to the intensity and diversity of radioactive beams, providing the set-up with a broad list of candidate isotopes. Presently the set-up is being tested with stable ions. The first experiment is expected for 2004. This work discusses the development of the WITCH set-up in detail.

The first two chapters focuss on the physics question to which the research program of the WITCH set-up is addressed in the first phase of its operation, i.e. search for Scalar interaction. First of all it will be a discussion on how the different interaction types can be distinguished from each other. This will be followed by an overview of the observables that nuclear beta decay provides to study the nature of the weak interaction. The second chapter will be fully dedicated to the $\beta - \nu$ angular correlation where an overview will be given of the different experimental approaches that are presently being used and the current status of the field.

The third chapter serves as an introduction into the principle of the WITCH set-up, giving an overview of the main building blocks of the set-up: REX-TRAP, the beamline system, the Penning trap structure and the retardation spectrometer. Each of these components will be the topic of a separate chapter (4-7) in which they are explained in detail. Furthermore chapter three contains a discussion on the achievable statistical precision of the WITCH set-up as well as the possible isotope candidate for a search for a Scalar weak interaction component. Chapter eight can be interpreted as a sort of summary of the set-up, discussing the overall efficiency of the set-up and the measurement time that is needed to perform a precision experiment with WITCH. Chapter nine briefly touches some possible physics goals that might be pursued with WITCH in future. Finally, the work is concluded by a brief summary of what has been achieved to date. A short outlook will be given on critical aspects of the WITCH set-up that should be addressed with special care to achieve the goal WITCH is aiming at: performing precision tests of the Standard Model.

Chapter 1

Standard Model and nuclear beta decay

The Standard Model describes the building blocks of the universe as well as how they interact with each other. After a short introduction on the most important aspects of the Standard Model relevant for this work, the attention will be focussed on the V-A nature of the weak interaction in nuclear beta decay. First the construction of the most general interaction Hamiltonian will be discussed that contain the exotic Scalar, Tensor and Pseudo-scalar interaction types besides the well-known Vector and Axial-vector contributions. After noting how those non-Standard Model interactions can be distinguished from the ”normal” ones the influence of the quark structure inside the nucleon will be briefly touched. The link between theory and experiment is provided by the section where the nuclear beta decay observables are discussed that allow a test of the V-A Standard Model assumption. The chapter will be concluded by an introduction in the rearrangement and loss of orbital electrons, better known as electron shake-off.

1.1 Standard Model

A detailed overview of the unification of the weak and electromagnetic interaction and the birth of the Standard Model falls beyond the scope of this work and will not be discussed. In stead the Standard Model elements that are relevant for the study of the weak interaction type will be mentioned. Lai (1981) gives reprints of the most fundamental papers in modern weak interaction.

The Standard Model was created shortly after the unfication of the weak and electromagnetic gauge theories by Glashow (1961), Weinberg (1967) and Salam. They predicted that the gauge transformations for the electro-weak interaction are

$$SU(2)_L \otimes U(1) \tag{1.1}$$

where both $SU(2)_L$ and $U(1)$ are spontaneously broken. The weak interaction is mediated by the charged $W^{\pm}$ and the neutral Z_0 gauge bosons. They acquire mass through the symmetry breaking by the scalar Higgs field. Their masses are $M_W \approx 80$ Gev and $M_Z \approx 90$ GeV explaining the short range of the weak interaction. For the electromagnetic interaction the massless photon is the force carrying particle for the electromagnetic interaction acting over an infinite range. Today the Standard Model also includes the strong interaction. This interaction is mediated by eight socalled-gluons. In this work the focus will be restricted to the weak part of the Standard Model.

The Standard Model predicts that the weak interaction is of the $V - A$-type (**V**ector and **A**xial-Vector). Other interaction types like Scalar, Pseudo-scalar or Tensor that are present in the most general weak interaction Hamiltonian (as will be discussed in the next section) are excluded. Experimentally those exotic interaction types are only ruled out down to the level of 10%. Furthermore it assumes that the weak interaction is invariant under time reversal but that parity is maximally violated. Only lefthanded particles take part in the weak interaction.

All particles that are presently known can be built up out of a small collection of 12 elementary particles: six quarks and six leptons. Those fermions can be divided into three generations. To account for the maximal parity violation the particles are grouped in left-handed doublets and right-handed singlets. The doublets are:

$$\begin{array}{ll} \textit{quarks} & \left\{ \begin{pmatrix} u \\ d \end{pmatrix}_L, \begin{pmatrix} c \\ s \end{pmatrix}_L, \begin{pmatrix} t \\ b \end{pmatrix}_L \right\} \\ \textit{leptons} & \left\{ \begin{pmatrix} \nu_e \\ e \end{pmatrix}_L, \begin{pmatrix} \nu_\mu \\ \mu \end{pmatrix}_L, \begin{pmatrix} \nu_\tau \\ \tau \end{pmatrix}_L \right\} \end{array}$$

The weak interaction transforms one particle of the doublet into the other. The right-handed particles are organized in $SU(2)$ singlets and do not take part in the weak interaction

$$\begin{aligned} \{u_R, c_R, t_R\} \\ \{d_R, s_R, b_R\} \\ \{\nu_{eR}, \nu_{\mu R}, \nu_{\tau R}\} \\ \{e_R, \mu_R, \tau_R\} \end{aligned}$$

1.2 The 4-fermion contact interaction for nuclear β-decay

Nuclear β-decay occurs when one of the nucleons in the nucleus transforms into its isospin partner accompanied by the emission of two leptons: a β particle and an (anti)neutrino. Depending on the charge of the emitted β-particle the decay is called β^- or β^+ decay. The electron capture (EC) process is the same process as β^+ decay but an orbital electron is captured instead of the emission of a β^+ particle. At the nucleon level the three decays can be written as:

$$n \rightarrow p + \beta^- + \overline{\nu_e}, \tag{1.2}$$

$$p \rightarrow n + \beta^+ + \nu_e, \tag{1.3}$$

$$e^- + p \rightarrow n + \nu_e. \tag{1.4}$$

Note that the kinematics of an EC transition differs drastically from the β decays. The presence of only two particles after the decay implies that they exhibit a discrete energy spectrum (i.e. their energy distribution is peaked around a fixed value) in stead of the continuous spectrum of the two β-decays.

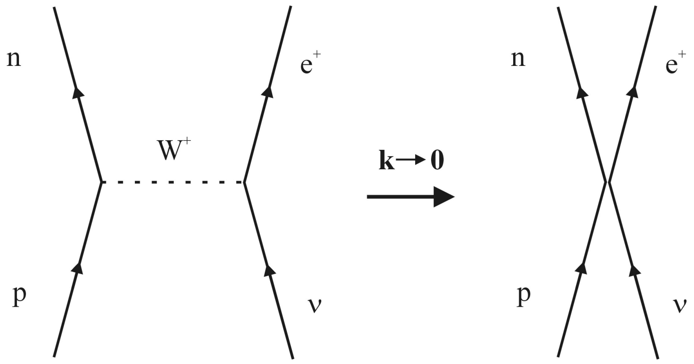

Figure 1.1: Feynmann diagram for a nuclear beta decay mediated by a W^+ boson (a) and as a point interaction (b).

1.2.1 From gauge boson to contact interaction

Although the weak interaction is mediated by a $W^\pm$ or a Z^0 boson, the Hamiltonian of the process can be approximated by a point interaction under the condition that the momentum transfer **k** between the hadrons and leptons is small compared to the mass of the gauge boson. In nuclear beta decay typical decay energies are of the order of a few MeV only. This allows to approximate the propagator describing the vector boson exchange in the Feynmann diagram of figure 1.1

$$\frac{-g^{\mu\nu} + \frac{k^\mu k^\nu}{M_W^2}}{k^2 - M_W^2} \rightarrow \frac{g^{\mu\nu}}{M_W^2}. \tag{1.5}$$

In this way one can relate the interaction strength of the weak point interaction to the gauge boson mass by $G_F/\sqrt{2} = g^2/(8M_W^2)$. Therefore, throughout this work a four-fermion contact interaction will be used to describe nuclear beta decay.

1.2.2 Nuclear beta decay Hamiltonian

A quantum mechanical theory of nuclear beta decay was first developed by Enrico Fermi in 1934. By analogy with the Hamiltonian for the current-field interaction of electromagnetism he proposed a Hamiltonian describing nuclear beta decay as the interaction of two (vector) currents, a hadronic $(\bar{p}\gamma_\mu n)$ and a leptonic current $(\bar{e}\gamma_\mu \nu_e)$:

$$\mathcal{H}_\beta = \frac{G_F}{\sqrt{2}}(\bar{p}\gamma_\mu n)(\bar{e}\gamma^\mu \nu_e) + h.c. \tag{1.6}$$

Later on this approach was extended by Gamow and Teller to all possible Lorentz invariant current-current interactions, not restricting to vector currents only (Gamow and Teller, 1936). In 1956 Lee and Yang pointed out that parity conservation had never been tested for the weak interaction. The experiment of Wu *et al.* (1957) showed one year later that parity is indeed violated in the weak interaction.

The leptons that take part in nuclear beta decay should, however, be treated relativistically. Therefore a more general formalism was constructed in which both nucleons and leptons satisfy the Dirac equations having a 4-component spin wave function. By assuming that the interaction is invariant under all proper Lorentz transformations (i.e. pure Lorentz transformations as well as rotations but excluding space inversion and time reversal) the Hamiltonian density is given by Lee and Yang (1956)

$$\begin{aligned} \mathcal{H}_\beta \quad \propto \quad & (\bar{\psi}_p\psi_n)(C_S\bar{\psi}_\beta\psi_\nu + C'_S\bar{\psi}_\beta\gamma_5\psi_\nu) \\ & +(\bar{\psi}_p\gamma_\mu\psi_n)(C_V\bar{\psi}_\beta\gamma^\mu\psi_\nu + C'_V\bar{\psi}_\beta\gamma^\mu\gamma_5\psi_\nu) \\ & +\frac{1}{2}(\bar{\psi}_p\sigma_{\lambda\mu}\psi_n)(C_T\bar{\psi}_\beta\sigma^{\lambda\mu}\psi_\nu + C'_T\bar{\psi}_\beta\sigma^{\lambda\mu}\gamma_5\psi_\nu) \\ & +(\bar{\psi}_p\gamma_\mu\gamma_5\psi_n)(C_A\bar{\psi}_\beta\gamma^\mu\gamma_5\psi_\nu + C'_A\bar{\psi}_\beta\gamma^\mu\psi_\nu) \\ & +(\bar{\psi}_p\gamma_5\psi_n)(C_P\bar{\psi}_\beta\gamma_5\psi_\nu + C'_P\bar{\psi}_\beta\psi_\nu) \\ & +h.c. \end{aligned} \tag{1.7}$$

The γ_i matrices are defined as in Wu and Moszkowski (1966) which is also the definition used by Jackson *et al.* (1957a,b); Lee and Yang (1956), $\sigma_{\lambda\mu} = -\frac{1}{2}i(\gamma_\lambda\gamma_\mu - \gamma_\mu\gamma_\lambda)$ and $\bar{\psi} = \psi^\dagger\gamma_4$. The *h.c.* in equation 1.7 makes sure that also β^+ decay is taken into account. The Axial-Vector term has the plus sign in front which is opposite to the original papers of Jackson *et al.* (1957b); Lee and Yang (1956) but in agreement with more recent papers

The Hamiltonian density is built up out of a sum of five terms always containing the interaction between a hadronic and a leptonic current. The five different terms can be distinguished by the transformation properties of the operator in the hadronic part and are under this convention named as the Scalar(S), Vector(V), Tensor(T), Axial-Vector(A) and Pseudoscalar(P) contributions. The leptonic part consists of a sum of two terms which have opposite parity due to the presence of the γ_5-operator. In this way the Hamiltonian can account for the parity violation observed in nuclear beta decay. Maximal parity violation would correspond to $|C_i| = |C_i'|$, while parity invariance is described by the condition that $C_i = 0$ or $C_i' = 0$. The relative strength of the different interaction types is also contained in the coupling constants C_i and C_i' $(i = S, V, T, A, P)$. Since there is no reason why a certain interaction type would be preferred above another, all contributions should a priori be considered for a description of the weak interaction process.

The key to distinguish the different interaction types from each other is lying in the leptonic part of the Hamiltonian. To clarify this statement it will be assumed for a moment that the β particle is massless. However, it should be stressed that the distinction between the interaction types is more general. The assumption $m_\beta = 0$ allows to assign a well-defined helicity to the β particle. In this respect the helicity is defined to be positive when the particles spin and momentum vector are parallel and negative if they are anti-parallel.

One can rewrite the operator $C_i + C_i'\gamma_5$ inside the leptonic part as a sum of two projection operators

$$K_1\left(\frac{1+\gamma_5}{2}\right) + K_2\left(\frac{1-\gamma_5}{2}\right) \tag{1.8}$$

where the constants K_1 and K_2 equal the sum, respectively the difference of C_i and C_i'. As shown in appendix A $\frac{1+\gamma_5}{2}$ is the left-handed projection operator for Dirac particles in the positive energy state and the right-handed projection operator for the negative energy states. For $\frac{1-\gamma_5}{2}$ it is vice versa, meaning that it projects on the right-handed component of a Dirac particle in the positive energy state and on the left-handed component for the negative energy states. It is clear, however, that the operator between the brackets of the leptonic current is always a sum of helicity projection operators.

For the EC capture process both leptons are particles in the positive energy state. By making use of the anti-commutation relations of the γ_i-matrices it can be shown that the helicities of both leptons should be equal to have a non-vanishing interaction in the case of the Vector and Axial-vector contribution, while the helicities should be opposite in the case of Pseudoscalar, Scalar and Tensor interaction. For β^+ decay the situation is opposite since here the β^+ particle should be interpreted as a negative energy state of the electron. Therefore the Vector and Axial-Vector will couple only β^+ and ν_e with opposite helicity while for Pseudoscalar, Scalar and Tensor interactions the leptons should have different helicities. A similar reasoning can be applied to β^- decay. As was mentioned above the Standard Model only allows interactions between lefthanded particles and righthanded anti-particles. From what was mentioned above only Vector and Axial-Vector interactions are allowed under those assumptions.

The Standard Model assumptions can be translated into the following conditions for the coupling constants:

- $C_i = C_i'$, $i = V, A$ (maximal parity violation)
- C_i and C_i' real, $i = V, A$ (time reversal invariance)
- $C_S = C_S' = C_T = C_T' = C_P = C_P' = 0$ (no Scalar, Tensor or Pseudoscalar interaction)

Whereas the leptonic part of the Hamiltonian density allows to distinguish between Vector and Axial-vector from one hand and Scalar, Tensor and Pseudoscalar from the other hand the hadronic part splits up those two groups. In the case of nuclear beta decay the nucleons can be treated non-relativistically. This implies that the Pseudoscalar contribution is negligible in comparison to the other terms. Furthermore, the non-relativistic description implies that the hadronic current for the Vector and the Scalar interaction gets identical, as shown by Wu and Moszkowski (1966). Those two contributions will therefore only be present in Fermi transitions. In a similar way the hadronic current of the Axial-vector and Tensor interaction becomes identical and A and T will only contribute to Gamow-Teller decays. The selection rules for those two types of decays are given in table 1.1.

Table 1.1: Selection rules for allowed nuclear beta decay; I represents the nuclear spin, T the isospin and $\pi_{i,f}$ the parity of initial and final states.

	F	GT
ΔI	0	0,1 (no $0 \rightarrow 0$)
ΔT	0	0,1 (no $0 \rightarrow 0$)
$\pi_i \pi_f$	+	+

1.2.3 Hamilonian at quark level and renormalisation

As far as is presently known the nucleons are not elementary particles but consist out of three quarks. A nuclear beta decay is governed by a transformation of a u quark in the proton into a d quark in the neutron or vice versa. Also at the quark level, a general Hamiltonian can be created that is invariant under all proper Lorentz transformations and contains the five interaction types (Herfurth *et al.*, 2001).

For nuclear physics experiments the quark level formalism is of no direct practical use since the interacting quark is always embedded into a nucleon. On the other hand one should also take into account the effects originating from the fact that nucleons are built up out of three quarks. To accommodate for this, a formalism is used in which the nucleons are treated as elementary spin-1/2 like in the case of equation 1.7. The nucleon medium effects can then be described by modifying the elementary Hamiltonian. The Vector and Axial-vector hadronic currents are then given as (Holstein, 1974; Towner and Hardy, 1995)

$$\begin{aligned} V_\mu^h &= i\bar{\psi}_p \left[g_V(k^2)\gamma_\mu + \frac{g_M(k^2)}{2M}\sigma_{\mu\nu}k_\nu + ig_S(k^2)k_\mu \right] \psi_n \\ A_\mu^h &= i\bar{\psi}_p \left[g_A(k^2)\gamma_\mu\gamma_5 + \frac{g_T(k^2)}{2M}\sigma_{\mu\nu}k_\nu\gamma_5 + ig_P(k^2)k_\mu\gamma_5 \right] \psi_n \qquad (1.9) \end{aligned}$$

where k is the momentum transfer between the leptons and hadrons participating in the decay. The first terms are the actual Vector (g_V) and Axial-vector (g_A) contributions containing the same operators as the Hamiltonian of equation 1.7. In the case of the Vector current no renormalisation due to the nucleon medium takes place as suggested by the Conserved Vector Current hypothesis (Gell-Mann, 1958). This has been verified at the level of $3 \cdot 10^{-4}$ by comparing the ft values of different $0^+ \rightarrow 0^+$ superallowed beta transitions (Towner and Hardy, 2003). For this reason the value unity has been assigned to the Vector strength C_V. The axial vector current is renormalised inside the nucleon medium and has been determined in neutron decay from the ratio $\lambda = C_A/C_V = -1.2670 \pm 0.0035$ (Groom and coworkers, 2000). The other contributions are so-called induced currents and are labelled weak magnetism (g_M), induced Scalar (g_S), induced Tensor (g_T) and induced Pseudoscalar (g_P). Assuming absence of so-called second class currents, $g_S = 0$ from CVC (Holstein, 1974, 1984) and $g_T = 0$ (Holstein, 1974; Wilkinson, 2000) for analog transitions like $0^+ \rightarrow 0^+$ and mirror decays. Since the induced pseudoscalar contribution is too small to produce measurable effects in nuclear β-decay (Holstein, 1974; Wilkinson, 2000), weak magnetism will be the only contribution that has to be taken into account for the precise $\beta - \nu$ angular correlation measurements that will be discussed in this work and is of the order of a few promilles.

1.3 Nuclear beta decay: experimental observables

To study the weak interaction aspects of nuclear beta decay several experimental observables are available like the momenta of the leptons $\mathbf{p}_\beta$ and $\mathbf{p}_\nu$, the polarization of the β-particle $\boldsymbol{\sigma}$ and the nuclear polarization $\mathbf{J}$. The neutrino momentum can hardly be measured directly but can be determined by measuring the recoil momentum. It was shown by Jackson, Treiman and Wyld (without (Jackson *et al.*, 1957b) and with (Jackson *et al.*, 1957a) Coulomb corrections) that combining the above mentioned vector quantities in different vector products will render an experiment sensitive to the coupling constants of the nuclear beta decay Hamiltonian 1.7. In case one deals with a non-oriented ensemble of nuclei the distribution function in the β and ν directions and the β polarization $\boldsymbol{\sigma}$ for allowed beta decay is given by

$$
\begin{aligned}
&\omega(\sigma|E_\beta,\Omega_\beta,\Omega_\nu)dE_\beta d\Omega_\beta d\Omega_\nu = \\
&\quad \frac{F(\pm Z,E_\beta)}{(2\pi)^5} p_\beta E_\beta (E_0-E_\beta)^2\, dE_\beta d\Omega_\beta d\Omega_\nu \frac{\xi}{2}\left\{1+a\frac{\mathbf{p}_\beta\cdot\mathbf{p}_\nu}{E_\beta E_\nu}+b\frac{m_\beta}{E_\beta}\right. \\
&\quad \left. +\boldsymbol{\sigma}\cdot\left[G\frac{\mathbf{p}_\beta}{E_\beta}+H\frac{\mathbf{p}_\nu}{E_\nu}+K\frac{\mathbf{p}_\beta}{E_\beta+m_\beta}\left(\frac{\mathbf{p}_\beta\cdot\mathbf{p}_\nu}{E_\beta E_\nu}\right)+L\frac{\mathbf{p}_\beta\times\mathbf{p}_\nu}{E_\beta E_\nu}\right]\right\} \qquad (1.10)
\end{aligned}
$$

where ξ is proportional to the decay rate and contains the nuclear beta decay matrix elements M_F and M_{GT}:

$$
\begin{aligned}
\xi &= |M_F|^2\left(|C_S|^2+|C'_S|^2+|C_V|^2+|C'_V|^2\right) \\
&\quad +|M_{GT}|^2\left(|C_A|^2+|C'_A|^2+|C_T|^2+|C'_T|^2\right) \qquad (1.11)
\end{aligned}
$$

The upper signs refer to β^- decay, the lower to β^+ decay. Further $p_\beta E_\beta(E_0-E_\beta)^2$ is the lepton phase space factor while $F(\pm Z,E_\beta)$ represents the Fermi function with Z the total charge of the daughter that corrects for the Coulomb interaction between the β particle and the nuclear charge.

1.3.1 Correlation coefficients

The correlation coefficients a, b, G, H, K and L all depend on the coupling constants C_i and C'_i, so a measurement of the corresponding correlation allows to extract weak interaction information. The present best limits on both Scalar and Tensor type interaction are obtained by measurements of the $\beta-\nu$ angular correlation coefficient a as will be discussed in chapter 2. Although G, H, K and L can in principle also be used to search for a scalar interaction, in practice it is a more challenging task since one also has to measure the polarization of the β particle with high precision. Expressions for those coefficients are described by Jackson *et al.* (1957a). A similar distribution function as in equation 1.10 for oriented nuclei is calculated by Jackson *et al.* (1957a). Such an approach can also be used to search for Tensor currents as will be performed in the near future (Severijns, 2003). This will however not be discussed here.

Including Coulomb corrections, the $\beta - \nu$ angular correlation coefficient a can be calculated from

$$\begin{aligned} a\xi = |M_F|^2 &\left[|C_V|^2 + |C'_V|^2 - |C_S|^2 - |C'_S|^2 \mp \frac{\alpha Z m_e}{p_\beta} 2Im \left(C_S C_V^* + C'_S C'^*_V \right) \right] \\ + \frac{|M_{GT}|^2}{3} &\left[|C_T|^2 + |C'_T|^2 - |C_A|^2 - |C'_A|^2 \pm \frac{\alpha Z m_e}{p_\beta} 2Im \left(C_T C_A^* + C'_T C'^*_A \right) \right] \end{aligned} \tag{1.12}$$

The upper signs refer to β^- decay, the lower to β^+ decay. Explicit expressions for pure Fermi and mixed transitions will be given in chapter 2.

Apart from the unity term inside the brackets of equation 1.10 the third term, known as the Fierz interference term, is not linked to any product of the observable vector quantities and will occur in each correlation measurement. It depends on the coupling constants via the relation

$$b\xi = \pm 2\Gamma Re \left[|M_F|^2 \left(C_S C_V^* + C'_S C'^*_V \right) + |M_GT|^2 \left(C_T C_A^* + C'_T C'^*_A \right) \right] \tag{1.13}$$

with $\Gamma = \left(1 - \alpha^2 Z^2\right)^{\frac{1}{2}}$. The Standard Model predicts that $b = 0$.

Comparing the dependence of a and b on the interaction coupling constants in a time reversal invariant picture reveals that the former has a quadratic dependence while the latter is linear in C_i and C'_i. The more advantageous dependence of the Fierz parameter has the disadvantage that it depends on the parity properties of the Scalar interaction, as can be seen from the fact that b would vanish when $C_S = -C'_S$. This prevents a measurement of the b-parameter from restricting the possible presence of a Scalar interaction.

1.3.2 Corrections to nuclear β decay

Besides the weak interaction that occurs between the hadron and the lepton current a couple of processes come into play and affect nuclear β decay observables. When performing precision measurements one should correct the experimental parameters for those processes to get reliable results. A clear overview of corrections to nuclear beta decay in the scope of ft-value studies of a couple of superallowed $0^+ \rightarrow 0^+$ transitions is given by Hardy and Towner (1975).

The largest correction to the decay process compensates for the Coulomb interaction between the β particle and the nuclear charge and is described by the Fermi function $F(\pm Z, E)$. It changes the shape of the β spectrum and depends on the charge of the emitted β particle. The Coulomb interaction also destroys the isospin purity of the nuclear states. In this way the total decay rate is affected.

A second type of correction originates from the emission of Brehmstrahlung photons or the exchange of virtual photons between the particles taking part in the weak interaction. Those so-called radiative corrections can be divided into two groups depending on whether their evaluation depends on the details of the strong interaction as discussed by Sirlin (1967): model independent (MI) or outer radiative corrections and model dependent (MD) or inner radiative corrections.

The model independent radiative corrections are sensitive to the experimental details of the decay. This means that they are different for different transitions. Furthermore they influence the kinematics of the decaying particles implying that they change spectral shapes. The MD corrections do not change the kinematics of the reaction particles. Therefore it only affects the total decay rate but is independent of the specific decay. More details concerning those corrections are given by Glück (2004).

To conclude it is good to note that the expressions for a and b given by Jackson *et al.* (1957a) do not include induced currents nor recoil order corrections. For sub-percent precision experiments those effects have to be taken into account. Expression for the $\beta-\nu$ angular correlation coefficient can be calculated from Holstein (1974) and are given by Severijns *et al.* (2004).

1.3.3 The ft value

The ft-value of a certain β transition is defined as the product of the so-called statistical rate function f as defined by Wilkinson and Macefield (1974), which is basically the integral of the lepton phase space including the Fermi function

$F(Z, E_\beta)$, and the comparative half-life

$$t = t_{1/2}\left(\frac{1+P_{EC}}{BR}\right) \tag{1.14}$$

where BR is the branching ratio of the transition and P_{EC} is the electron capture rate. The ft-value allows to study how the decay probability depends on nuclear parameters (like the wave functions) but without being dependent on the lepton phase space or the Coulomb effects due to the nuclear charge. By integrating expression 1.10 one can derive an expression for the ft-value of a certain decay which includes the Fierz interference coefficient b.

Inside the Standard Model assumptions one can write the ft value for a mixed transition as

$$ft = \frac{2K}{G_F^2 V_{ud}^2}\frac{1}{(1+\delta_R)\,2\left[|M_F|^2 C_V^2(1-\delta_C)(1+\Delta_R) + |M_{GT}|^2 C_A^2\right]} \tag{1.15}$$

The isospin impurity of the nuclear states is taken into account by the Coulomb correction δ_C (Hardy and Towner, 1975). In the mass region up to $A = 50$ δ_C is of the order of 0.5%. The model independent radiative corrections are described by δ_R which amounts typically to about 3% for masses up to $A = 50$. Model dependent radiative corrections are introduced into equation 1.15 by Δ_R=0.0240(8) (Towner and Hardy, 2003).

The most precise experimental determination of the Fierz coefficient in Fermi decays is based on the ft values for nine superallowed $0^+ \rightarrow 0^+$ beta transitions and results in $b_F = -0.0027 \pm 0.0029$. This corresponds to an upper limit for $|b_F| < 0.0075$ at 90%CL (Towner and Hardy, 2003). Relating this to the coupling constants of the scalar interaction an upper limit can be placed on the sum of the couplings constants. This however does not restrict presence of the scalar interaction.

1.4 Electron shake-off after nuclear beta decay

1.4.1 What is electron shake-off?

Looking back to the three expressions 1.2 describing nuclear beta decay one can easily see that the charge of the daughter nucleus will depend on the decay type that has occurred. If the mother ion is in the charge state q then the daughter ion/atom would have charge $q-1$, q or $q+1$ for β^+ EC or β^- decay respectively. This nuclear transition can be accompanied by the excitation and/or loss of one or more orbital electrons which will modify the final daughter charge state. In general three processes can cause this ionization.

- sudden change of the nuclear charge
- direct collision between the β particle and the orbital electron
- recoil of the nucleus due to β-decay

The most dominant factor causing prompt ionization after the nuclear beta decay is the sudden change of the nuclear charge. The orbital mismatch of the electron wave functions in the initial and final state which is caused, can lead to single or multiple ionizations. The daughter nucleus shakes off most easily orbital electrons from the outer shells. This is shown by Carlson *et al.* (1968) where shake-off probabilities for the different orbital shells have been calculated for various β^- decaying elements ranging from $Z = 2$ to 92. In the region $Z = 10 - 24$ the probability decreases with a factor of 10 to 30 when going from the outermost shell to the K-shell.

A second ionizing mechanism is the direct collision (DC) between the emitted β particle and the orbital electrons. For a mean β kinetic energy $\bar{E}_\beta$, the ratio of K-shell electrons ejected per decay by direct collisions ($P_K(DC)$) over the K-shell shake-off probability due to the sudden nuclear charge change ($P_K(SO)$) was first estimated by Feinberg (1941) to be

$$\frac{P_K(DC)}{P_K(SO)} \approx \frac{B_K}{\bar{E}_\beta}, \tag{1.16}$$

with B_K the binding energy of an electron in the K-shell. Therefore it has been believed that the direct collision would only affect very low β endpoint decays and can be neglected in other cases. However, recent calculations (Batkin *et al.*, 1992; Intemann, 1983) indicate that the DC mechanism in β^+ decays with endpoints of $\sim$ 1 MeV is 15-20 times larger than the Feinberg estimate. A calculation for the case of ^{21}Na reveals a DC contribution to K-shell ionization of $\approx 1\%$ (Scielzo *et al.*, 2003).

The third ionization process comes from the recoil due to the emission of the two leptons. A recoil dependent ionization rate has been observed up to now only in the pure Gamow-Teller decay of ^{6}He (Carlson *et al.*, 1963). Separating the abundance of the charge states into a recoil energy dependent and independent part, revealed that the recoil energy contribution was 3% for charge 2^{+} and 55% for the 3^{+} state. In other β-decays no clear recoil shake-off has been observed yet (Carlson, 1963a; Scielzo *et al.*, 2003). One should note that the daughter nucleus of ^{6}He has a recoil energy of 1.5 keV which is very high in comparison to the typical few hundreds of eV in most other β decays. In the case of the ^{21}Na experiment the determined limits on the recoil dependence are however not stringent enough for current precision β decay experiments, as discussed by Scielzo *et al.* (2003). Therefore a more careful study of the recoil contribution in the shake-off process is necessary for high precision experiments $\beta-\nu$-angular correlation experiments.

Vacancies that are created in the orbital shells after nuclear beta decay can be refilled by electrons, accompanied by the emission of X-rays or Auger electrons. In the last case additional ionization can occur. Especially in the case of EC capture where an electron from the inner shells is typically captured, this can result in a drastic charge state distribution change.

1.4.2 Experimental data

In the fifties and sixties charge state distributions have been measured for β^{-} emission of a number of noble gases: ^{6}He (Carlson *et al.*, 1963), ^{23}Ne (Carlson, 1963a), ^{85}Kr (Snell and Pleasonton, 1957) and ^{41}Ar (Carlson, 1963b). These experiments showed that 80 to 90% of the nuclei ends up in the original 1^{+} charge state and less than 5% looses two or more electrons.

More recently, measurements have been performed in atom traps on the β^{+}-decay of ^{21}Na (Scielzo *et al.*, 2003) and ^{38m}K (Gorelov *et al.*, 2000). One would expect the β^{+} charge-state distribution to be similar to the β^{-} distribution shifted by a charge of +2 because of the difference in ΔZ. A charge state distribution comparison of ^{21}Na (β^{+}) with ^{23}Ne (β^{-}) and ^{38m}K (β^{+}) with ^{41}Ar (β^{-}) reveals that the first three charge states agree very well when shifting the distribution with one unit of charge. This implies that an extra electron, most

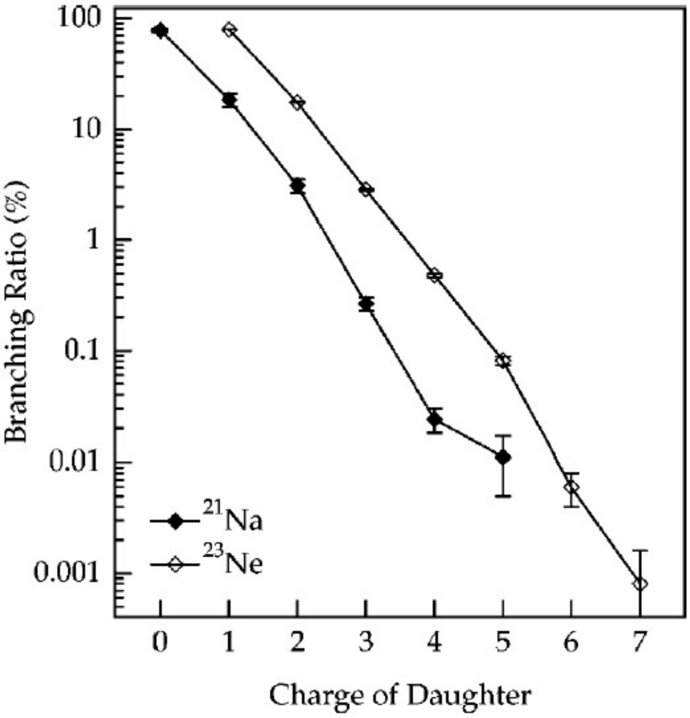

Figure 1.2: Charge state distribution of the daughter ion/atom after the β^+-decay of ^{21}Na and the β^--decay of ^{23}Ne (Scielzo *et al.*, 2003).

likely the valence electron, is frequently lost (Scielzo *et al.*, 2003). Figure 1.2 (Scielzo *et al.*, 2003) shows a comparison between the charge state distributions for the β^+ decay of ^{21}Na and the β^--decay of ^{23}Ne.

As discussed above, the charge state distribution changes more drastically in the case of EC-decay. Since the electron is with highest probability captured from the K-shell the rearrangement of the orbital electrons causes the charge state distribution not to be a monotonically decreasing function anymore as in the case of $\beta^{\pm}$-decay. The maximum is in general shifted to higher values. As an example the charge state distribution for ^{37}Ar (Snell and Pleasonton, 1955) is shown in figure 1.3. The most probable charge state of the ^{37}Cl ions is the 3^+ charge state corresponding to the loss of three orbital electrons.

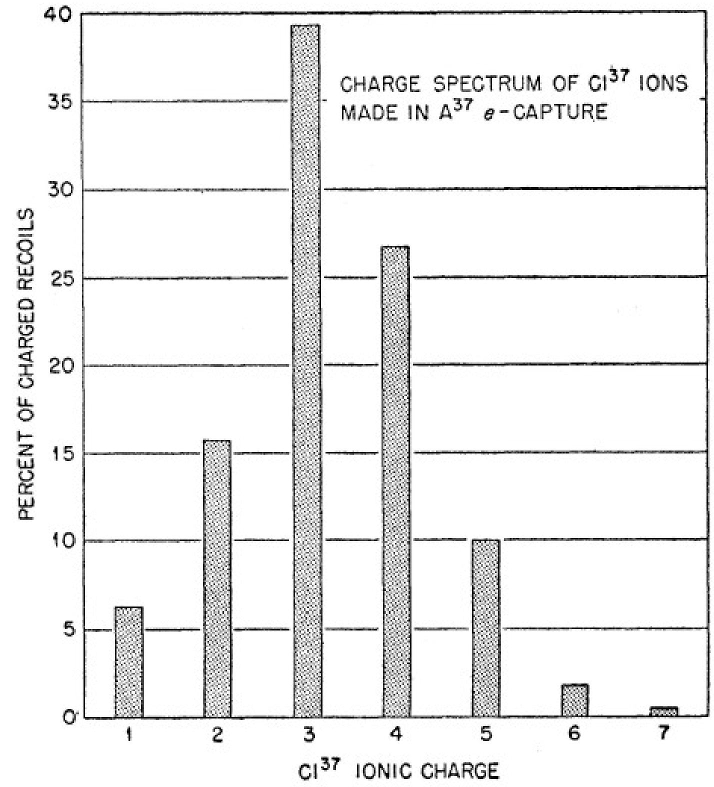

Figure 1.3: Charge state distribution of ^{37}Cl ions produced in ^{37}Ar EC decay (Snell and Pleasonton, 1955).

To conclude one should note that all measurements up to now have been performed with set-ups where the radioactive source contained neutral atoms.

Chapter 2

The β-ν angular correlation

The $\beta - \nu$ angular correlation is sensitive to the interaction type of the weak force and has led to the determination of the V-A structure in the fifties. In order to understand how this angular correlation can be used to investigate the interaction type first of all an intuitive picture will be presented. Confirmation of this reasoning will be provided by the expression for the so-called a parameter that describes the angular correlation. This will be followed by an overview of the different experimental approaches to study the angular correlation and how the use of atom and ion traps has initiated a new generation of experiments. Since the WITCH set-up will measure the recoil energy spectrum of the daughter nuclei, a discussion of the recoil energy spectrum will be held. All equations in this and the next chapters will assume time reversal invariance implying the coupling constants to be real. Since the first phase in the physics program will be focussed on a search for a scalar interaction, the most attention will go to pure Fermi transitions.

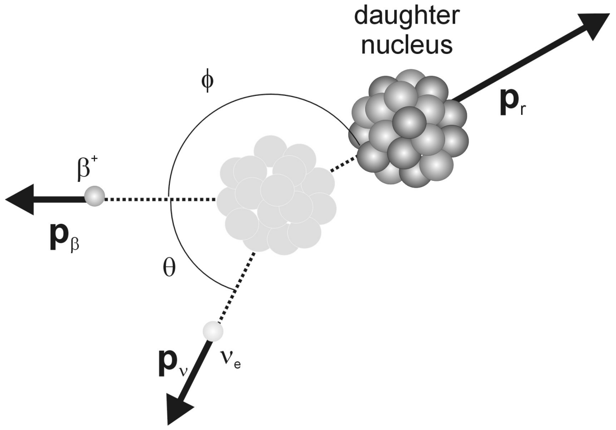

Figure 2.1: Schematic view of the $\beta - \nu$ angular correlation.

2.1 The β-ν angular correlation

2.1.1 Visualization

Assuming that the polarization of the β particle is not measured, equation 1.10 can be written as the distribution in angle θ between the propagation directions of the two leptons emitted in nuclear beta decay (see figure 2.1)

$$W(\theta) = 1 + \frac{\frac{\mathbf{p}\cdot\mathbf{q}}{E_\beta E_\nu} a}{1 + \frac{\Gamma m_e}{E_\beta} b}. \tag{2.1}$$

This angular correlation depends on both the $\beta - \nu$ angular correlation coefficient a as well as the Fierz interference parameter b.

As was shown in chapter 1 one can distinguish the two interaction types that can contribute in a pure Fermi transition (i.e. Vector and Scalar interaction) or a pure Gamow-Teller transition (i.e. Axial-vector and Tensor interactions) by the helicity coupling between the leptons. Considering a $0^+ \rightarrow 0^+$ β^+ transition the Vector contribution, as described in the Standard Model, would only couple a left-handed ν_e with a right-handed β^+ particle. The scalar interaction would only participate between those two leptons having equal helicity. Since there is no change of spin between initial and final nucleus the spins of the leptons

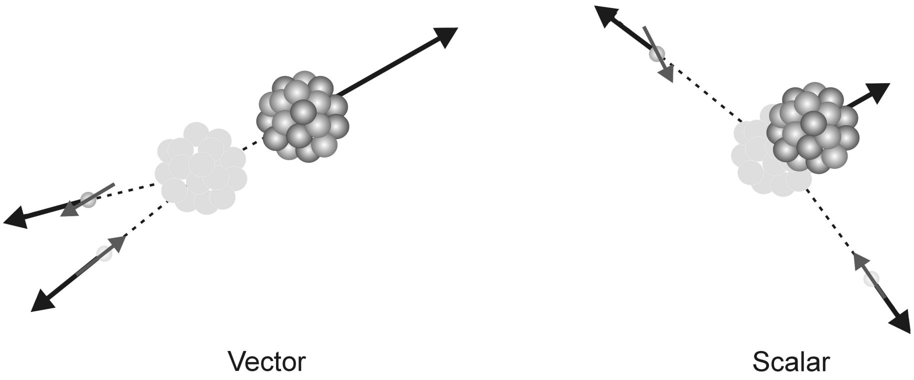

Figure 2.2: Propagation directions of the three reaction particles for a Vector and a Scalar-type weak decay.

should add up to zero. This implies that a Vector decay is characterized by leptons that are preferentially emitted parallel, while the Scalar case would result into back-to-back emission. Applying this reasoning onto equation 2.1 and assuming for a moment that $b = 0$, indicates that the Vector interaction is characterized by an a parameter that is positive while the scalar interaction would have a negative value for a. Since the momentum of the recoil nucleus is the vector sum of the two lepton momenta, the vector interaction will result on average into larger recoil momenta than the scalar one.

2.1.2 The a parameter

As was shown in section 1.3 the β-ν angular correlation of a beta transition depends on the strength of the different weak interaction type contributions. Before writing an explicit expression it is useful to introduce the Fermi to Gamow-Teller mixing ratio y that can be written as

$$y^2 = \frac{|M_F|^2}{|M_{GT}|^2} \frac{|C_S|^2 + |C'_S|^2 + |C_V|^2 + |C'_V|^2}{|C_A|^2 + |C'_A|^2 + |C_T|^2 + |C'_T|^2}. \tag{2.2}$$

For reasons of notational simplicity the positive quantity Y_i is defined that contains the coupling constants for the interaction type i as

$$Y_i^2 = |C_i|^2 + |C'_i|^2. \tag{2.3}$$

Table 2.1: Values for the $\beta-\nu$ correlation parameter a for the different weak interaction types.

Interaction	a
Scalar	-1
Vector	1
Axial-Vector	-1/3
Tensor	1/3

The value Y_i represents the strength of particular interaction-type independent of the helicity coupling involved and is an upper limit for the magnitude of both coupling constants C_i and C_i'. Combining equations 1.12 and 1.11 with 2.2 and 2.3 gives in a time reversal invariant situation (TRI)

$$\begin{aligned} a &= a_{SM} + \epsilon_{\beta\nu} \\ &= \frac{y^2 - \frac{1}{3}}{1+y^2} + \frac{2}{1+y^2}\left[-y^2 \frac{Y_S^2}{Y_S^2+Y_V^2} + \frac{1}{3}\frac{Y_T^2}{Y_T^2+Y_A^2}\right]. \end{aligned} \tag{2.4}$$

The a parameter has been separated into a Standard Model prediction a_{SM} and a possible anomaly $\epsilon_{\beta\nu}$ which is due to a Scalar or Tensor type weak interaction. One can determine the a parameter for a certain pure interaction type j by setting all coupling constants $C_i = 0$ for $i \neq j$. The result is summarized in table 2.1. Since a can be expressed in terms of the strength Y_S, a determination of the $\beta - \nu$ angular correlation coefficient allows to search for a Scalar interaction and this irrespective of the helicity properties of it.

Figure 2.3 shows the dependence of Y_S as a function of the β-ν anomaly $\epsilon_{\beta\nu}$ for different values of the Fermi to Gamow-Teller mixing ratio y. The case y=1000 can in to very good approximation be considered as a pure Fermi decay. This plot can be used to estimate the maximum scalar contribution that can be present if a measurement would obtain the Standard Model prediction a_{SM} with an experimental precision $\epsilon_{\beta\nu}$. For a pure Fermi decay a 1% precise measurement excludes a scalar interaction above the level of 10% of the Vector coupling constant at 68%CL. It is clear that the limit on a scalar interaction gets weaker when one has a mixed transition in comparison with a pure Fermi

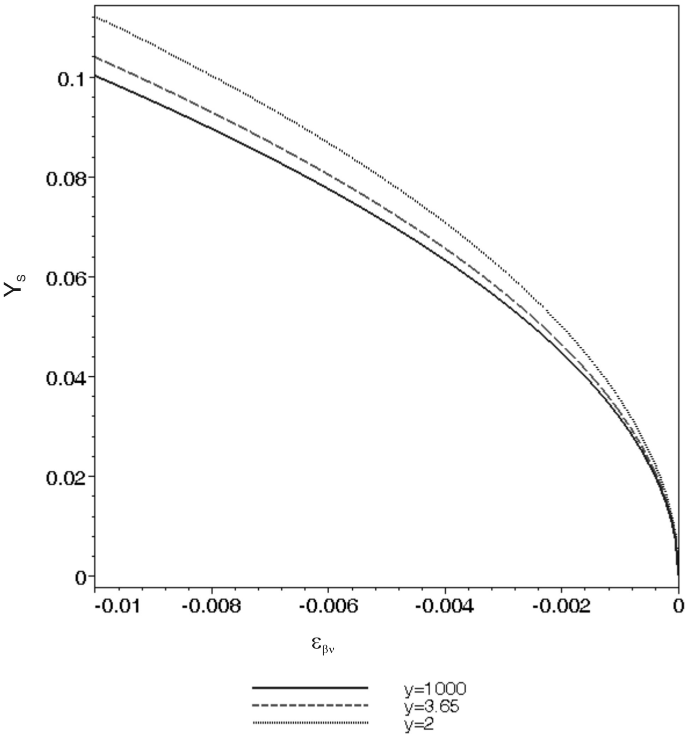

Figure 2.3: Dependence of Y_S on the anomaly $\epsilon_{\beta\nu}$ with $C_V = C'_V$=1. The Tensor contribution in $\epsilon_{\beta\nu}$ has been neglected.

decay.

As soon as one measures the $\beta - \nu$ angular correlation the experimental observables will also depend on the Fierz interference coefficient. By using the Fermi over Gamow-Teller mixing ratio y expression 1.13 can be rewritten as

$$b = \pm 2\Gamma \frac{1}{1+y^2} \left(y^2 \frac{C_S C_V + C'_S C'_V}{Y_V^2 + Y_S^2} + \frac{C_T C_A + C'_T C'_A}{Y_A^2 + Y_T^2} \right). \tag{2.5}$$

This indicates that the Fierz coefficient b depends linearly on the coupling constants. Figure 2.4 shows an exclusion plot for the coupling constants C_S and C'_S for the case that $b = 0 \pm 5 \cdot 10^{-3}$. A measurement of only the b parameter does not allow to restrict the presence of a scalar interaction in pure

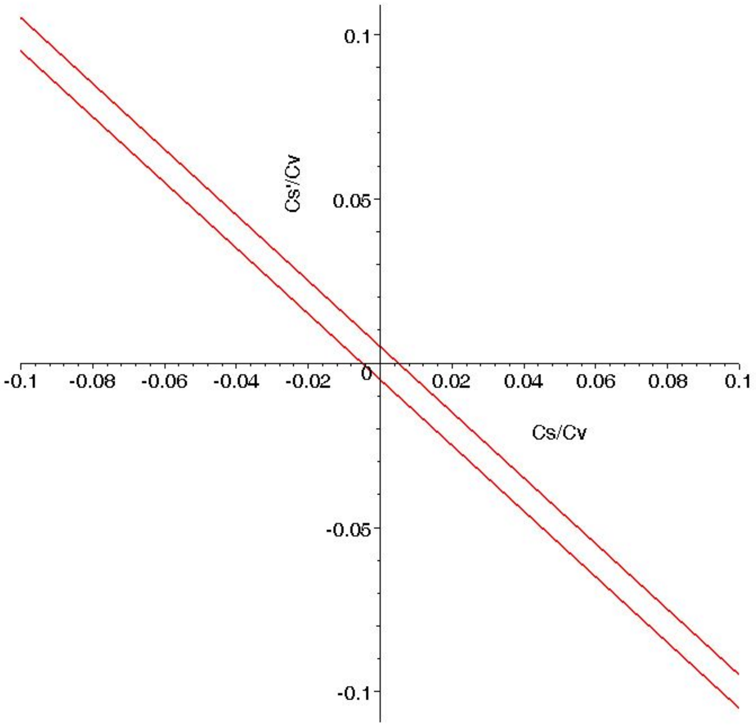

Figure 2.4: Exclusion plot from a measurement of the Fierz coefficient $b = 0 \pm 5 \cdot 10^{-3}$. The forbidden region is lying in between the two lines.

Fermi decay indicating that the a and the b parameters reveal complementary information.

2.2 Measuring the $\beta - \nu$ correlation coefficient

Since the kinematics of the decay process takes place in a two dimensional plane it is characterized by 5 parameters as shown in figure 2.1: the two angles θ and ϕ and the 3 momenta magnitudes p_β, p_ν and p_r. By using the laws of conservation of momentum and energy the number of free parameters can be reduced to two. The measurement of two variables thus allows to reconstruct the complete kinematics of each event and determine the value of a. Since the ν is difficult to detect the only three parameters that are accessible in practice are: p_r (or T_r), p_β (or E_β) and the angle between the β particle and the recoiling nucleus ϕ. Three experimental approaches are presently used to measure the $\beta - \nu$ angular correlation coefficient.

A measurement of the $\beta - \nu$ angular correlation coefficient is far from straightforward as can be seen from the few measurements that have been performed with good accuracy. This is mainly caused by the fact that the recoiling daughter should be detected, which has an energy of at best only a few hundreds of eV. The classical approach in nuclear beta decay experiments is to implant the activity into a foil with typically tens of keV energy. For α, β or γ detection this method works fine. The majority of low energy recoil ions originating from nuclear β decay will however not be able to escape from this host material and the minor fraction does escape will suffer a lot from scattering such that the kinematical information is totally lost. A second problem with the low energy recoils is that they easily participate in chemical bindings. Also in this case the recoil information ”disappears”.

2.2.1 Avoiding the scattering problem

A first approach that has been followed in the early days of $\beta - \nu$ angular correlation measurements consisted in using a gaseous source from which the recoil ion could easily escape without significant scattering. This explains why the measurements that experimentally revealed the V-A structure of the weak interaction (Allen *et al.*, 1959) in the fifties have all been performed on noble gases: ^{6}He, ^{19}Ne, ^{23}Ne and ^{35}Ar. The inertness of those elements also avoided the formation of chemical bounds with surrounding atoms or molecules. Using a gaseous source, however, strongly limits the number of candidates for an experiment. A second disadvantage is that one can not localize the radioactive species very well in space which is especially of importance for the β-recoil coincidence measurements. After a very active period in the fifties and early sixties, the field of $\beta - \nu$ correlation came to rest.

In the second half of the nineties a revival of the $\beta - \nu$ angular correlation measurements takes place when the advantages of traps are being recognized in the field of nuclear physics. Traps have the important advantage that the radioactive isotopes can be captured in a vacuum environment which reduces scattering to a minimum. Secondly the use of electromagnetic fields and/or laser beams (depending on the type of trap) allows to localize the source very precisely in space. One can distinguish two types of traps: atom traps and ion traps. An overview of trap facilities for $\beta - \nu$ correlation measurements can be found in Kluge (2002) and Behr (2003b).

The magneto-optical atom trap (MOT), consists of three orthogonal pairs of circularly polarized counter-propagating laser beams and a magnetic quadrupole field generated by two coils in anti-Helmholtz configuration, as shown in figure 2.5 (a). An atom approaching e.g. from the left passes through the trap until the increasing Zeeman effect shifts it into resonance with the σ_- laser from the right, see figure 2.5 (b). Since the laser is red-detuned, resting atoms in the center of the trap do not interact with the laser. However moving atoms are Doppler shifted into resonance due to their rest velocity and thus experience interaction leading to both cooling and trapping. Laser cooling of the atoms is a very powerful technique that allows to cool the particles to very low temperature and very high densities. Disadvantage of the atom trap is that the injection efficiency is very low (typically a couple of promilles) and that it is only possible to trap atoms that can be excited with a laser which are mostly alkalis.

In the category of ion traps one can distinguish two types which are schematically shown in figure 2.6: the Penning trap and the Paul trap. The Penning trap makes use of a strong magnetic field to confine the ions in the radial direction. An electrostatic quadrupole potential that is applied between the central ring electrode and the two end cap electrodes ensures axial confinement of the ion. The principle of a Penning trap will be discussed in more detail in chapter 6. The Paul trap uses an oscillatory radio-frequency quadrupole field for creating a pseudo-potential and confining the ions. In this way it does not require a magnetic field. This combination generates an electric pseudo-potential in which the charged particles can stay trapped. Ion traps have the advantage over the atom traps that in principle each element can be confined. Furthermore injection efficiencies of 50% and more can be achieved. A disadvantage of the Penning trap is the high cost of the super conducting magnet system that

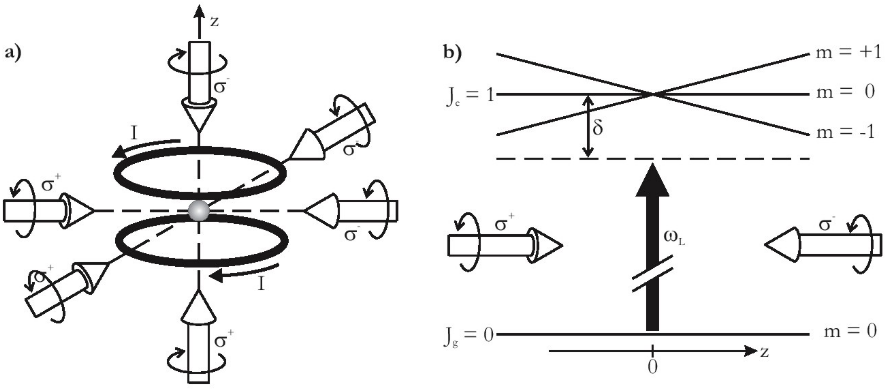

Figure 2.5: Schematic overview of a Magneto-Optical Trap (MOT) (from Grünert (2002)). a) two coils in anti-Helmholtz configuration creating the magnetic quadrupole field and three pairs of counter propagating laser beams b) excited state Zeeman shift of a two-level atom along one axis.

usually generates the strong magnetic field. In case of the Paul trap, the RF heating of the ions limits the minimal kinetic energy to which the ions can be cooled.

Since the trapping potential for all those traps mentioned above is rather small (typically smaller than 10 V) the daughter ions that have typically of the order of a few hundreds eV are able to escape out of the trap thus allowing energy analysis of the recoiling nucleus. Over the last 5 years a number of set-ups have been developed to perform $\beta - \nu$ angular correlation measurements with high precision using MOT's (Gorelov *et al.*, 2000; Scielzo, 2003), Penning traps (Beck *et al.*, 2003; Byrne *et al.*, 2002) or Paul traps (Delahaye *et al.*, 2000; Savard *et al.*, 1999).

2.2.2 Experimental approaches

In order to determine the $\beta - \nu$ angular correlation coefficient, different experimental approaches have been followed in the past and will be applied in future measurements. The techniques can be divided into three categories:

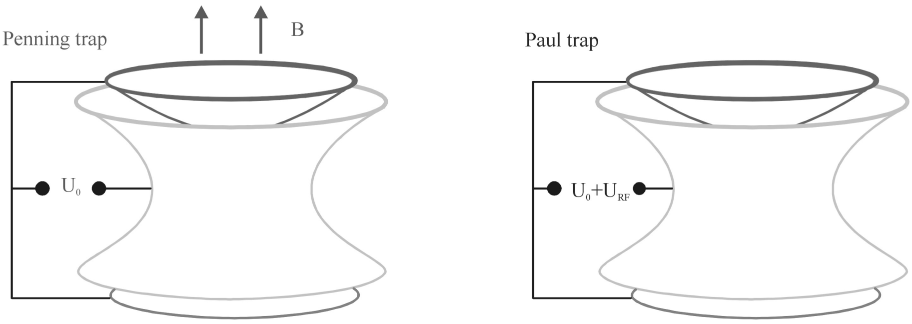

Figure 2.6: Schematic view on a Penning trap (left) and a Paul trap (right).

- β-recoil coincidence measurement
- direct measurement of recoil energy spectrum
- detection of secondary radiation

β-recoil coincidence measurements

In a β-recoil measurement two kinematical variables are measured allowing a complete reconstruction of the decay kinematics. Normally the β particle is used as a start trigger for the TOF measurement of the recoil ion, revealing the recoil momentum p_r. The β energy is the second observable being measured. This approach also allows to reconstruct the recoil energy spectrum that is sensitive to the a-parameter. Delahaye (2002) has shown that for the pure Gamow-Teller decay of ^{6}He the accuracy that can be obtained by fitting a from the $W(p_\beta, p_r)$ distribution, is the same as if one would use the reconstructed recoil energy spectrum for the same number of decays.

A β-recoil coincidence measurement is being performed on the pure Fermi decay of ^{38m}K with the TRINAT set-up at the /TRIUMF-facility (Vancouver), shown in figure 2.7. The ^{38m}K beam is neutralized and trapped in the first MOT. A push beam moves atoms to the second MOT where the β-recoil coincidence measurement takes place. The β^+ telescope is a Si strip detector which is backed by a plastic scintillator for the β energy determination. The recoil is

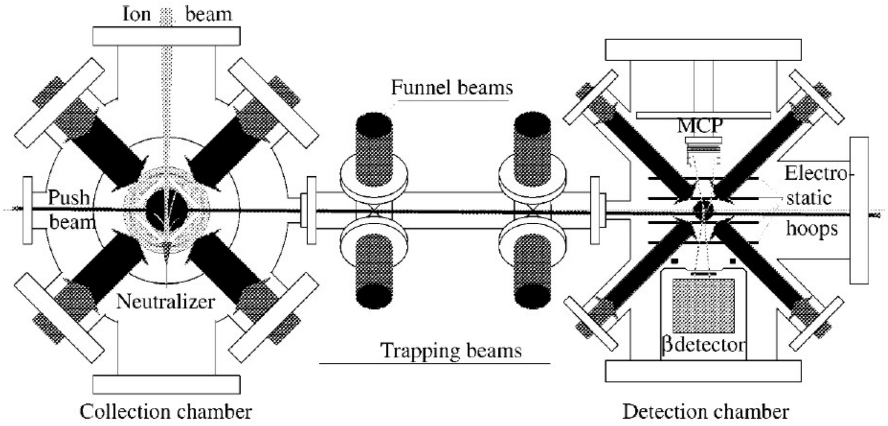

Figure 2.7: Top view of the TRINAT set-up at TRIUMF (see text).

detected with an MCP detector. Data is being analyzed providing a preliminary result of $a = 0.9974 \pm 0.0030 \pm 0.0040$ (Behr, 2003a).

Also at Berkeley a MOT is being used to perform β-recoil coincidence measurements, and first experiments have been performed. The analysis provided a value $a = 0.5243 \pm 0.0092$ which deviates 3.6σ from the Standard Model (Scielzo, 2003). Further analysis is going on to clarify this discrepancy which is believed to be caused by the branching ratio value used, that is suspect of not being reliable. At LPC/Caen a set-up is being tested to measure the β–^{6}Li coincidence after the pure Gamow-Teller decay of ^{6}He. The source is confined in a Paul trap (Delahaye, 2002; Delahaye *et al.*, 2000). First run is scheduled for 2004.

The advantage of the coincidence approach is that one has information of single events and that the background is very small. Furthermore the method allows a broad range of systematic checks. An unavoidable disadvantage is that the coincidence rate is relatively small: 0.5% for the Berkeley ^{21}Na experiment (Scielzo, 2003).

Direct measurement of recoil energy spectrum

Besides the TOF technique as used in the β-recoil coincidence experiments, it is possible to reconstruct the recoil energy spectrum by only detecting the recoil ions. The set-ups that have been built for this type of measurements, use electromagnetic fields to perform the recoil energy selection. The a-parameter of the pure Gamow-Teller decay of ^{6}He has been determined experimentally with the Oak Ridge spectrometer, which is shown in figure 2.8. The ^{6}He, produced in a reactor by the $^{9}\mathrm{Be}(n,\alpha)^{6}\mathrm{He}$ reaction, is carried by a continuous stream of water vapor to the laboratory where the vapor is removed and the ^{6}He is left to decay in the conical source volume. A magnetic analyzer was used to select recoil ions with a specific energy. An electrostatic analyzer installed further downstream allows to give complete q/m identification. The recoil ions are detected by a secondary-electron multiplier. The measurement on ^{6}He resulted in $a = -0.3343 \pm 0.0030$ (Johnson *et al.*, 1963). This provides the current best limit on the Tensor coupling constants C_T and C'_T for already 4 decades now(!).

The WITCH set-up will use a retardation spectrometer to measure the recoil energy spectrum. The principle of this type of spectrometer, which makes use of an electrostatic retardation to perform the energy analysis, will be discussed in chapter 7. To study the $\beta - \nu$ angular correlation in free neutron decay a similar approach is used in the aSPECT set-up (Zimmer *et al.*, 2000).

Doppler shift of secondary radiation

The last approach exploits the fact that the energy of β delayed p or γ radiation is Doppler shifted due to the recoil momentum of the β daughter. By measuring the Doppler shift one can access the β recoil information. Assuming the secondary radiation particle would have a momentum k then the ratio of the maximal shift ΔE_{rad} of the peak over the nuclear beta recoil energy T_r is given in first order as

$$\frac{\Delta E_{rad}}{T_r} \approx 4\frac{k}{p_r}, \tag{2.6}$$

showing that the Doppler shift is more pronounced for heavier secondary particles. An important requirement is off course that the β-daughter nucleus

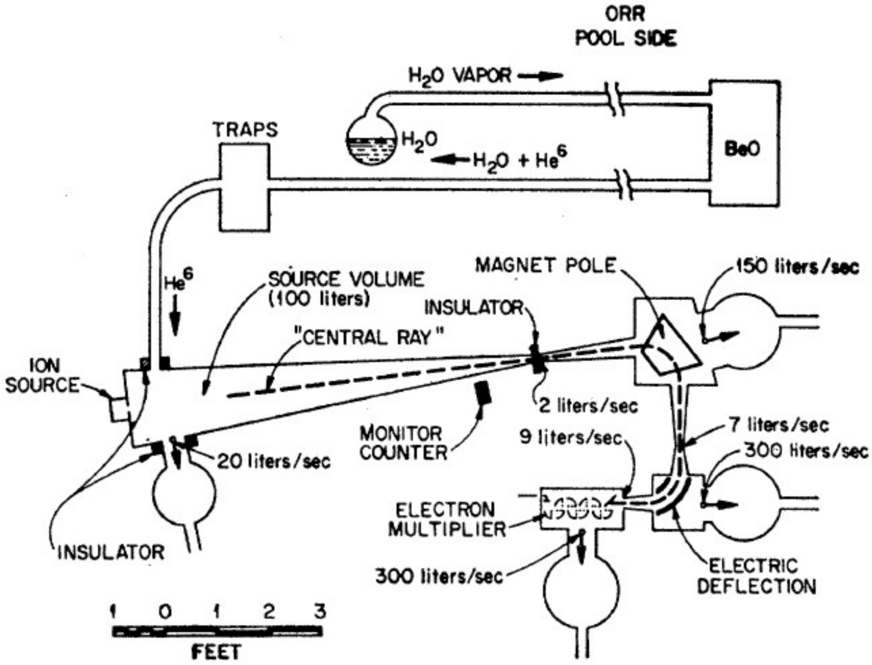

Figure 2.8: Experimental layout of the Oak Ridge recoil spectrometer (from Johnson *et al.* (1963)).

decays prompt such that no scattering or energy loss can deform the information that is transferred to the secondary particle. Two approaches are followed to exploit this Doppler shift for a determination of the $\beta-\nu$ angular correlation measurement.

If the β particle is not detected, the Doppler shift of the secondary radiation will result in a broadening of the peak that is measured. This approach has been followed at ISOLDE where the broadening of the β-delayed proton peak after the superallowed $0^+ \rightarrow 0^+$ decay of ^{32}Ar has been measured. The 60 keV ^{32}Ar-beam was implanted in a carbon foil. The protons were measured by $p-i-n$ diodes. To suppress the β background in the detectors the foil was placed in a 3.5 T super-conducting coil. A fit of the broadening of this proton peak to the a-parameter resulted in $a = 0.9989 \pm 0.0065$ at 68%CL (assuming $b = 0$) (Adelberger *et al.*, 1999). Reanalysis of this experiment is however necessary after it was demonstrated that the Q-value of the β transition (with quoted error of 2.2 keV) that has been used for the analysis (calculated from the isobaric-multiplet mass equation (IMME)), deviates by 5 keV from the experimental Q-value measured with the ISOLTRAP mass spectrometer (Blaum *et al.*, 2003).

A second approach consists in measuring the shift of the peak by performing a coincidence measurement between the β particle and the corresponding secondary for a certain detector geometry. This method has been applied to γ emission following the nuclear beta decay of ^{18}Ne (Egorov *et al.*, 1997) and ^{14}O (Vorobel *et al.*, 2003). The ^{18}Ne experiment suffered from low statistics (29% upper limit for S-interaction) but will be improved and repeated in the near future. In the second experiment the measurement accuracy is limited by the interatomic interaction taking place inside the gaseous target. This indicates the need for a trap system to avoid such problems. A $\beta - \nu$ angular correlation measurement of ^{14}O using a Paul trap is under development (Savard *et al.*, 1999). Also at GANIL near Caen, a proposal has been submitted to perform a measurement of the shift of the β-delayed proton peak of ^{32}Ar (Egorov *et al.*, 2001).

2.2.3 Current status and prospects

The present situation of the limits on the Scalar coupling constants for the most precise measurements of the a and b parameters are summarized in the exclusion plot 2.9 at 95 % CL. The annulus is the result of the measurement of the β-delayed p peak after the decay of ^{32}Ar (Adelberger *et al.*, 1999; García *et al.*, 2000). The experimental data was fitted to a single parameter $\tilde{a}$ containing both the a-parameter and the Fierz coefficient b

$$\tilde{a} = \frac{a}{1 + \frac{\Gamma m_e}{E_\beta} b}. \tag{2.7}$$

The diagonal band is the result of the determination of b from the ft-values of a number of superallowed $0^+ \rightarrow 0^+$ β-transitions from Ormand *et al.* (1989). As discussed before the measurements of a and b yield complementary information on the coupling constants.

In the coming years a boost of new data can be expected, that will allow to update this exclusion plot and restrict the permitted zone for a scalar interaction even further. First of all the ^{32}Ar experiment will be re-analysed. The TRIUMF and Berkeley experiments are analysing their experimental data and will soon publish their final result. Furthermore a number of new experiments will soon be taken in operation. The new results will provide first a check of the data obtained so far with different techniques and will allow to restrict the Scalar couplings even further. An overview of the new experiments is given in table 2.2.

2.3 Recoil energy spectrum

2.3.1 Recoil energy spectrum shape

The starting point to calculate the recoil energy spectrum is the integration of the distribution 1.10 over all possible β particle polarizations σ resulting in $W(E_\beta, \theta_{\beta\nu})$. By a transformation of variables one can convert this $W(E_\beta, \theta_{\beta\nu})$-expression into a distribution $W(E_\beta, T_r)$. This is done by Kofoed-Hansen

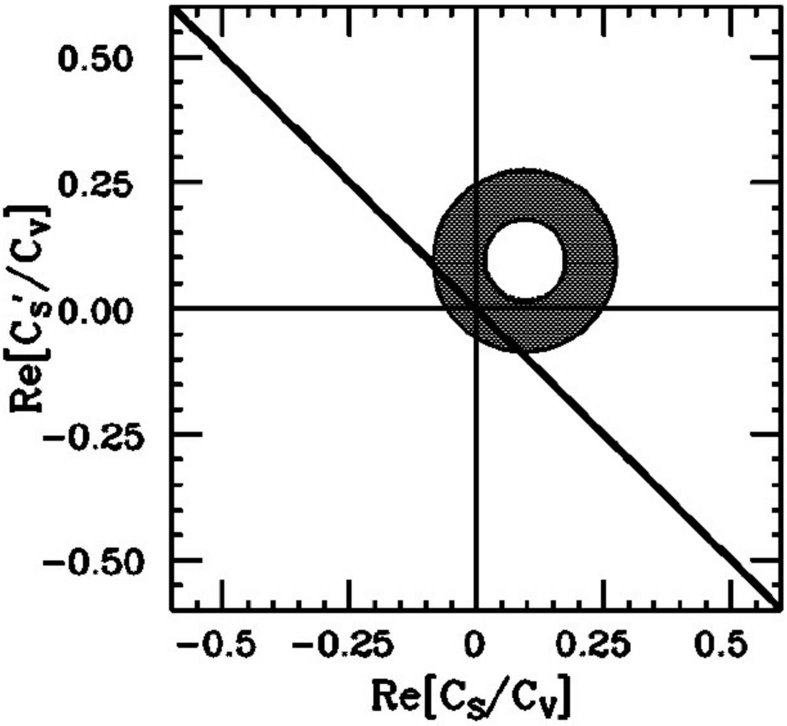

Figure 2.9: Exclusion plot for the coupling constants of the Scalar interaction C_S and C'_S (95%CL) (from García *et al.* (2000)).

Table 2.2: List of most precise a-parameter measurements for both Scalar and Tensor searches together with newly developed experiments. Quoted errors are 68%CL.

isotope	S or T	a_{exp}	source	measurement technique	reference
^{6}He	T	-0.3343 ± 0.0030	gas	recoil energy spectrum	Johnson *et al.* (1963)
^{6}He	T	in preparation	Paul	β-recoil coincidences	Delahaye *et al.* (2000)
n	S/T	in preparation	n-beam	recoil energy spectrum	Zimmer *et al.* (2000)
^{14}O	S	in preparation	Paul	β-recoil coincidences	Savard *et al.* (1999)
^{18}Ne	S	in preparation	gas	β^{+} delayed γ shift	Vorobel *et al.* (2003)
^{21}Na	S	0.5243 ± 0.0092	MOT	β-recoil coincidences	Scielzo (2003)
^{32}Ar	S	0.9989 ± 0.0065	C-foil	β^{+} delayed p broadening	Adelberger *et al.* (1999)
^{32}Ar	S	in preparation	C-foil	β^{+} delayed p shift	Egorov *et al.* (2001)
^{35}Ar	S	in preparation	Penning	recoil energy spectrum	Beck *et al.* (2003)
^{38m}K	S	$a = 0.9974 \pm 0.0050$ (prel.)	MOT	β^{+} delayed γ shift	Behr (2003a)

(1954) yielding

$$P(E_\beta, T_r)dE_\beta dT_r = \frac{M}{2}F(Z, E_\beta)\left[ep_\nu + bp_\nu + \frac{a}{2}\left(2MT_r - p_\beta^2 - p_\nu^2\right)\right] dE_\beta dT_r \tag{2.8}$$

This expression is written in natural units are used and does not include any recoil order corrections or induced current contributions. Coulomb corrections are taken into account by the Fermi function $F(Z, E_\beta)$. Integration of $P(E_\beta, T_r)$ over the total β energy E_β yields the recoil energy spectrum. All figures of recoil spectra in this work have been generated with this approach setting $F(Z, E_\beta) = 1$.

Figure 2.10 shows the shape of the recoil spectrum of the superallowed $0^+ \rightarrow 0^+$ decay of ^{26m}Al. The $\beta - \nu$ correlation parameter has been varied from -1 to $+1$ to show how the spectral shape depends on a. As predicted in section 2.1 the maximum of the recoil energy spectrum shifts to higher values for increasing a.

The endpoint energy of the recoil spectrum corresponding to the β-transition $^A_Z X \rightarrow ^A_{Z\pm1} X$ is given by

$$T_r^{max} = \frac{(\Delta M_{at}c^2 \pm m_e c^2)^2 - m_e^2 c^4}{2M_{at}(^A_{Z\pm1}X)c^2}, \tag{2.9}$$

where ΔM_{at} denotes the atomic mass difference between the mother and daughter particle, the upper signs correspond to β^- and lower signs refer to β^+-decay. On the right side of this expression the recoil energy term has been neglected with respect to the total decay energy (ΔM_{at}). Avoiding this approximation would give a correction of the order of 10^{-4} as is shown in appendix B, in which exact expressions can be found. This means that equation 2.9 is accurate enough for most applications.

Due to the principle of the retardation spectrometer the WITCH-set-up measures the integral spectrum. The spectral shape of the integral spectrum is also determined by the β-ν angular correlation coefficient. For a ranging from -1 to 1 the dependence is shown in figure 2.11. Through out this work integral recoil spectra $S_i(T_r)$ will be denoted with the subscript $_i$ and this in contrast to differential spectra $S_d(T_r)$ which are labelled with $_d$.

The natural question that arises is which of the two spectral shapes is best

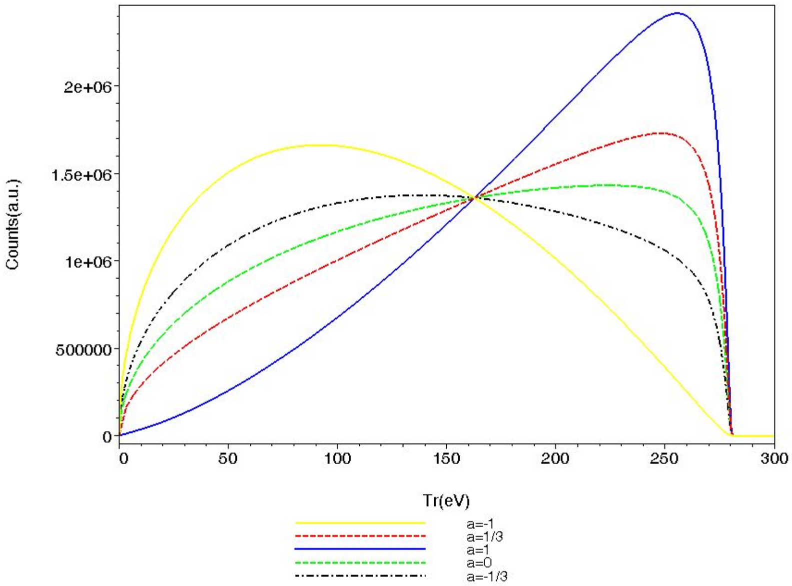

Figure 2.10: Differential recoil energy spectra of the β^+ decay of ^{26m}Al for different $\beta - \nu$ correlation parameters a. Assumptions: $F(Z, E_\beta) = 1$ and $b = 0$.

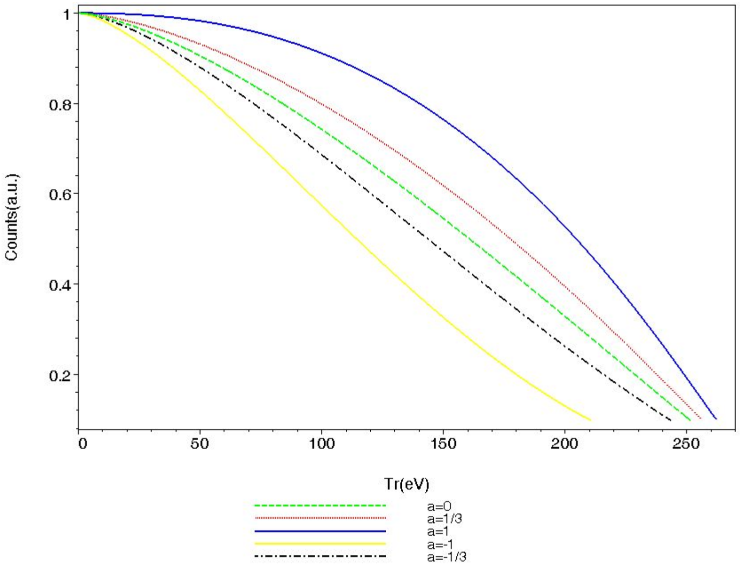

Figure 2.11: Integral recoil energy spectra of the β^+ decay of ^{26m}Al for different $\beta - \nu$ correlation parameters a. Assumptions: $F(Z, E_\beta) = 1$ and $b = 0$.

to fit: the measured integral spectrum or the differential one calculated out of the experimental spectrum. Up to now no hard evidence for choosing either of the two has been established. The procedure to fit the a-parameter from the integral spectrum is sketched further down. This can be easily adapted to a fit of the differential spectrum by omitting the last step.

2.3.2 Corrections to the spectral shape

As discussed in subsection 1.3.2 certain processes affect the kinematics of nuclear β decay. This results in a deformation of the shape of the β spectrum and consequently also the recoil energy spectrum. Therefore a calculated spectrum should be corrected for those effect before a meaningful comparison can be made with an experimental spectrum.

The Coulomb interaction between the β particle and the nucleus is taken into account by the Fermi function $F(\pm Z, E_\beta)$. Given a certain spectrum $S_d(T_r)$, the model independent radiative corrections can be included by

$$S_d^\gamma(T_r) = S_d(T_r)(1 + r(T_r)/100) \tag{2.10}$$

where $r(T_r)$ is the relative radiative correction function for the spectral shape as defined by Glück (1998); Glück (2004). The index γ indicates that radiative corrections have been included. This correction can be almost up to 3% for a decay with $\Delta - m_e$ of 5 MeV, where Δ denotes the atomic mass difference between mother and daughter particles (Glück, 2004). For the decays of ^{32}Ar and ^{6}He the correction to the spectrum shape gave a shift in a-parameter of the order of 0.3 % (Glück, 1998).

For $\beta - \nu$ angular correlation measurements below the percent level equations 1.10 and 2.8 are not accurate enough anymore. In this case second order contributions (weak magnetism and induced tensor terms) and recoil order contributions should be taken into account. This approach is shown for instance by Glück (1998) where an expression for $P(E_\beta, T_r)$ is derived from a more accurate expression of the distribution $W(E_\beta, \cos\theta_{\beta\nu})$ out of (Holstein and Treiman, 1971).

2.3.3 Fitting the recoil energy spectrum

The procedure to fit the β-ν angular correlation coefficient out of a certain integral spectrum $S_i(T_r)$ (measured or randomly generated) consists in a comparison with a sample spectrum $\tilde{S}_i(T_r)$ that is generated from a given set of parameters $(\tilde{N}, \tilde{a}, \tilde{b})$ and that includes all physical or set-up related corrections. The best fitting sample spectrum provides the fit parameters a_{fit}, b_{fit}. As a comparison technique between the two spectra a χ^2 approach can be applied. Other statistical methods will be explored in future to find the best fitting routine for this type of problem.

Generating a sample spectrum $\tilde{S}_i(T_r)$ is done in four steps.

Generate a theoretical differential spectrum The procedure to generate the theoretical spectrum $\tilde{S}_d(T_r)$ given certain parameters $(\tilde{a}, \tilde{b}, \tilde{N})$ is explained in subsection 2.3.1.

Include corrections Including radiative corrections the differential spectrum will get the form:

$$S_d^{\gamma}(T_r) = S_d(T_r)(1 + r(T_r)/100) \tag{2.11}$$

where the correction function $r(T_r)$ has been discussed in section 2.3.

Include response of set-up The measured spectral shape will deviate from the theoretical function $S_d^{\gamma}(T_r)$ due to the effects related to the set-up itself. In order to include this deformation one should fold it with the response function of the set-up $R(T_r)$. This function will be discussed in more detail in chapter 7.

Construct the integral spectrum The integral spectrum $S_i(T_r)$ is created by integrating the folded differential spectrum from T_r up to the endpoint of the spectrum.

Chapter 3

WITCH set-up: principle and overview

The WITCH set-up is designed to measure the recoil energy spectrum of the daughter ions after nuclear beta decay that reveals information on the interaction type of the weak decays as discussed in chapter 2. The experimental apparatus consists out of a Penning trap that is coupled to a retardation spectrometer. In the first section the experimental principle behind the set-up will be discussed. As will become clear one actually measures the integral recoil energy spectrum with this approach. The discussion of the set-up itself will be closed by an overview of its main components: the beamline system, the Penning trap structure and the retardation spectrometer. Each of them will be discussed in more detail in the following chapters. This will be followed by the results of the achievable accuracy study for this type of measurement. After this an overview will be presented on possible candidates for the search to Scalar currents.

3.1 Principle of the set-up

3.1.1 A Penning trap as radioactive source container

In order to allow detection of the low energy recoil ions and minimize scattering effects as much as possible the WITCH set-up confines the radioactive ions in a Penning trap. In comparison to atom traps, the Penning trap benefits from the universality in ion species that can be trapped allowing to select the best candidate isotope for a certain measurement. The presence of the magnetic field avoids the RF-heating of the ion motion that occurs in the Paul trap, resulting into a lower mean energy in the case of the Penning trap. Furthermore all charged particles that are emitted inside a solid angle of almost 2π, are focussed by the strong magnetic field into the axial direction. In the context of the design goal to develop a set-up having a broader application field than $\beta - \nu$ correlation measurements, the magnetic focussing is of particular interest as will be discussed in chapter 9.

The WITCH set-up contains two cylindrical Penning traps. The first one, the cooler trap will be used to remove energy from the ions and center the ions in the trap. The second one, the decay trap, acts as the radioactive source container. The reason for this separation finds its origin in the fact that in the cooler trap the interaction between the buffer gas atoms and the ions is essential for removing energy, while in the decay trap collisions are undesirable since they disturb the recoil energy determination. Differential pumping in between the two traps keeps the pressure in the decay trap sufficiently low.

3.1.2 Measurement principle

The decay trap acts as a scattering free radioactive source container in which approximately 10^6 ions with charge 1^+ are stored. The recoil energy that the daughter nuclei gain in the β decay is typically an order of magnitude larger than the electrostatic trapping potential. In this way the ions can escape from the trap. All ions recoiling into a 2π solid angle will be focussed by the strong magnetic field of the Penning trap into the direction of the spectrometer.

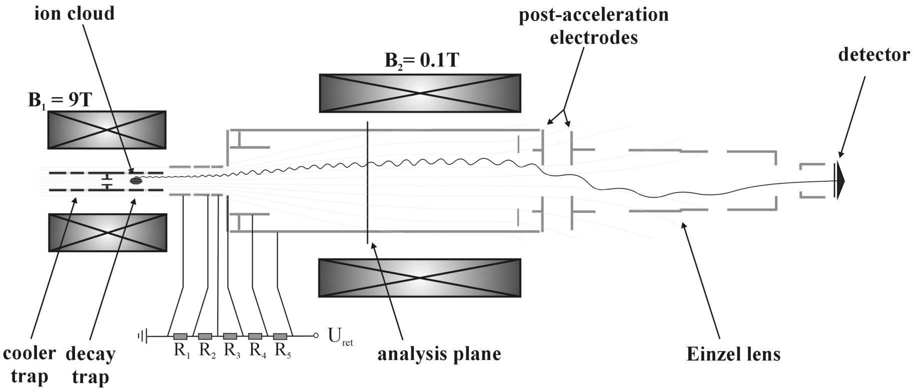

Figure 3.1: Schematic view on the principle of the WITCH set-up

The final charge state of the ions would in principle be 0,1^+ or 2^+ in the case of β^+, electron capture or β^--decay. Apart from this charge change the ion can loose one or more orbital electrons due to the shake-off process. In this way the ions end up with a charge state distribution when entering the spectrometer.

The energy analysis principle of the WITCH retardation spectrometer is the same as in the Mainz (Picard *et al.*, 1992) and Troitsk (Lobashev and Spivak, 1985) spectrometers which are used to measure the electron antineutrino mass by determining the exact shape of the β-spectrum of tritium near its endpoint. An electrostatic retardation potential filters the high energy particles that are counted on a detector behind the barrier. Since this energy analysis only takes the velocity component parallel to the retarding electric field into account, a high energy resolution of the filtering would correspond to a small emission solid angle. Therefore the electrostatic retardation concept is combined with a magnetic parallelizer. This concept is shown in figure 3.1. The radioactive source is placed in the high magnetic field B_1 of the decay trap. While the recoil ions travel through the region with slowly decreasing magnetic field, their radial kinetic energy is adiabatically converted into axial energy. When they arrive in the low magnetic field region almost all kinetic energy is in the motion along the magnetic field axis, indicating that the isotropically recoiling ions are parallelised an that their energy can be analysed with high resolution. Due to the strong focussing of the high magnetic field, the spectrometer accepts now a solid angle of almost 2π.

The ions that make it over the retardation barrier will be post-accelerated and counted by a micro channel plate (MCP)-detector. In this way the recoil energy spectrum is integrated from eU_{ret} up to the endpoint of the spectrum. By changing the retardation voltage one can scan the complete integral recoil energy spectrum.

Since the doubly charged ions see a retardation barrier which is twice the applied potential, their recoil spectrum endpoint will be exactly in the middle of the the recoil spectrum of the singly charged ions. For the higher charged ones this will be a third, a quarter etc... This means that only the upper half of the recoil spectrum, corresponding to the singly charged ions, will not be contaminated. Therefore the first experiments will only take this part of the spectrum into account for the fit of the $\beta - \nu$ angular correlation coefficient.

3.1.3 Set-up overview

The WITCH set-up is installed at the ISOLDE (Kugler, 2000; Kugler *et al.*, 1992) facility at CERN, being currently the world leading facility for the production of radioactive isotopes. The PS-booster accelerator delivers proton bunches with an energy of 1.4 GeV that are shot on a thick target. Due to spallation and fragmentation reactions that take place, radioactive nuclei are produced and diffuse out of the target by heating. The activity is guided via a transfer line to the ion source region where ionization is performed. The radioactive ions then get extracted, accelerated up to an energy of 60 keV and are guided to the separation magnet. Depending on the separation magnet that is chosen one can get a mass resolution of 2000 with the GPS (General Purpose Separator) or maximally 20000 for the HRS (High Resolution Separator). Figure 3.2 shows the layout of the ISOLDE facility. Figure 3.3 shows the WITCH set-up and its different components at the ISOLDE/CERN facility.

After mass separation the DC radioactive ISOLDE beam with an energy of 60 keV is guided to REXTRAP (Ames *et al.*; Schmidt, 2001; Schmidt *et al.*, 2002), the cylindrical Penning trap of the REX-ISOLDE project (Habs and coworkers, 2000). After collection of the continuous ISOLDE beam, the ions are cooled

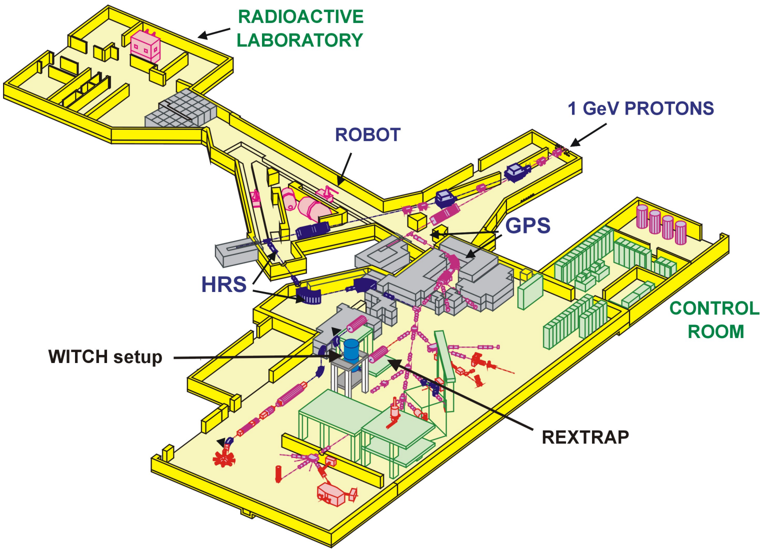

Figure 3.2: Layout of the ISOLDE facility.

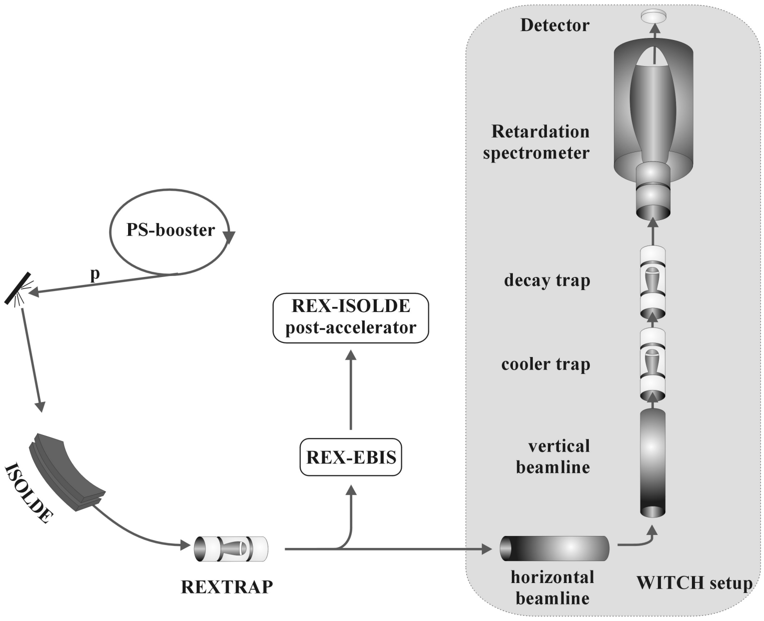

Figure 3.3: Schematic overview of the WITCH set-up.

and centered in this Penning trap. The bunched beam that is ejected out of REXTRAP and accelerated up to 60 keV has much better beam properties than the original ISOLDE beam. The most important features of REXTRAP for the WITCH set-up will be discussed in chapter 4.

The connection between REXTRAP and the WITCH-set-up is made by a UHV beamline. Part of the beamline is lying in a horizontal plane and guides the beam via an electrostatic deflector to the vertical axis of the actual WITCH set-up, that is positioned vertically due to space restrictions at the ground level. In the vertical beamline in front of the actual set-up the beam is retarded stepwise from 60 keV down to 1.5 keV. In this section a long drift cavity is pulsed over 60 kV in 1 μs while the ion bunch is inside, to adjust the potential energy of the ions and allowing capturing in a Penning trap on ground potential. After further deceleration the beam is injected into the cooler trap, where the ion bunches are again centered and cooled. The decay trap is the second trap of the double Penning trap system of the WITCH trap where the cooled ions are stored to observe their decay. The decay trap is coupled to the retardation spectrometer where the energy analysis of the recoil ions is performed.

Figure 3.3 shows a schematic overview of the set-up divided into the four main sections. The different sections of the WITCH set-up will be described in detail in the next chapters. Figure 3.4 shows a picture of the set-up installed in the ISOLDE hall.

3.2 Achievable accuracy with the WITCH experiment

In order to determine the accuracy on small a that can be achieved with the experimental approach of the WITCH set-up, a series of random recoil spectra have been generated from which the a parameter was fitted. By changing all kinds of set-up parameters like, fit interval, bin width, etc... it was possible to investigate their influence on the achievable precision on a.

The procedure for this study consisted in generating a random recoil energy spectrum $S_i(T_r)$ starting from certain input parameters (a, b, N, σ) and search

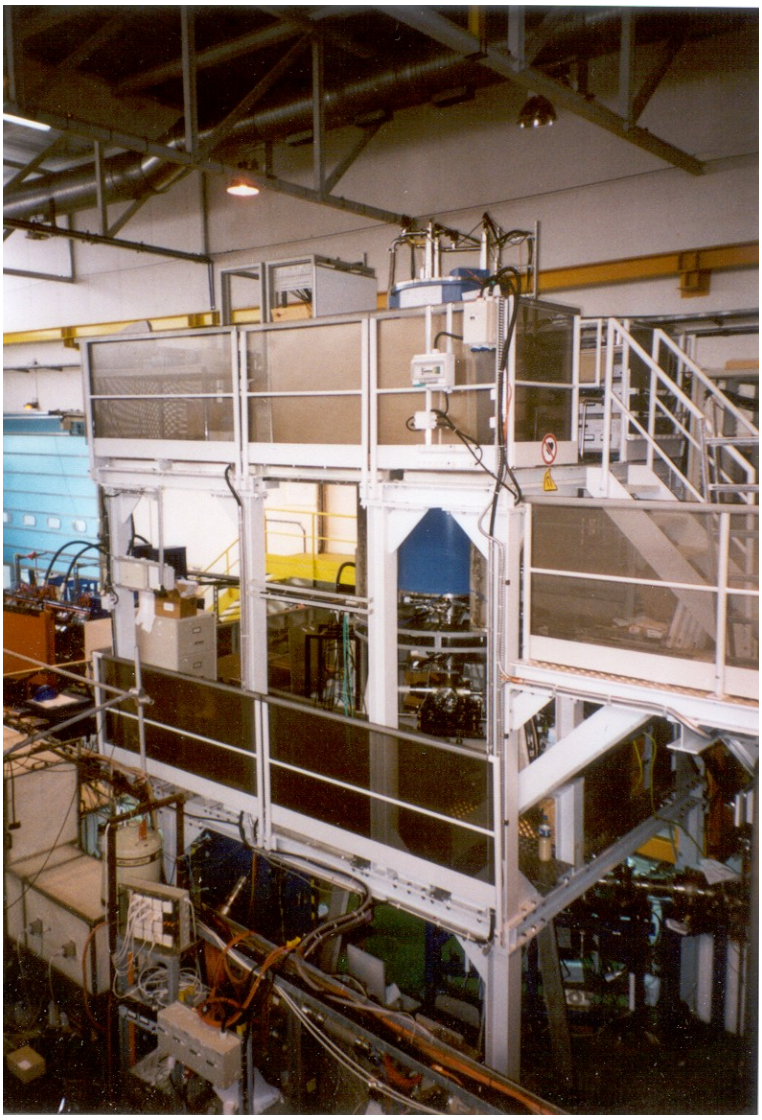

Figure 3.4: WITCH set-up installed at the ISOLDE/CERN facility.

for the best fitting sample spectrum. To include the response of the set-up the integral spectrum was folded with a gaussian function with σ equal to the energy range of the true response function of the retardation spectrometer as derived in chapter 7. The fitting was performed with a maximum likely hood method. The random spectrum is generated in a similar way as for getting the sample spectrum $\tilde{S}_i(T_r)$ with an additional randomization applied on the integral spectrum using a Poisson distribution for the number of counts in a bin. Repeating the procedure for different random spectra gives the statistical spread on the fitted value a_{fit}.

In order to determine how many events are needed to reach a certain statistical accuracy, spectra with different number of counts have been fitted with the procedure mentioned above. The results in figure 3.5 show the achievable statistical precision as a function of the number of events in the differential spectrum. It can be seen that a statistical accuracy of the order of 0.5% on a can be reached when one would have 10^7 recoil ions in the differential spectrum. This result is achieved by only fitting the upper half of the spectrum, which is free of multiply charged ions. The same figure also includes the achievable precision when the fit range is reduced.

On should note that the achievable precision that has been discussed is purely statistical. In a real experiment the experimental uncertainty will also be determined by the systematic effects of the set-up like which will be discussed in chapter 7.

3.3 Candidates for Scalar current search

As was mentioned in chapter 1 a Scalar admixture in nuclear beta decay can only be present in Fermi transitions. Since the first experiments with the WITCH set-up will be focussed on a Scalar interaction search, the highest sensitivity for this research program can be obtained in pure Fermi decays. The selection rules for nuclear beta decay state that the only transitions that are of the pure Fermi-type are those where $\Delta I = 0$ and $\Delta T = 0$. Those decays are known as the superallowed $0^+ \rightarrow 0^+$ decays and only a couple of tens of them are known at present. Apart from pure Fermi decays mixed transitions with a

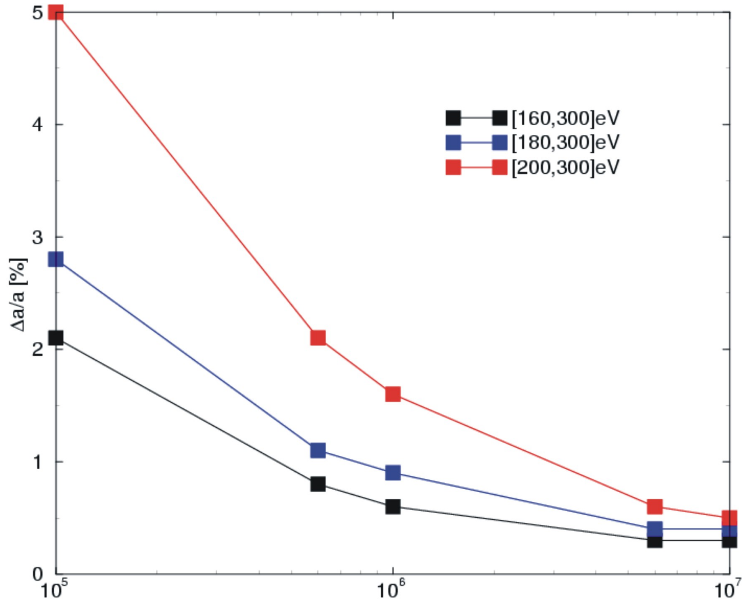

Figure 3.5: Achievable statistical accuracy on a for different event numbers in the differential recoil energy spectrum and for different fitted intervals.

dominant Fermi contribution can also be good candidates. In this respect the so-called mirror transitions in odd-even nuclei are interesting candidates. Since the initial and final nuclear states differ only by the interchange of a proton into a neutron, the wave functions will overlap very well and the decay will be minimally influenced by nuclear structure effects.

To determine whether a certain isotope can be used for a precise measurement of the $\beta - \nu$ angular correlation coefficient it should fulfill certain requirements.

Stable daughter If the daughter nucleus of the nuclear β decay would not be stable, it could gain recoil energy. This sudden change in kinetic energy could disturb the energy analysis that is performed inside the retardation spectrometer. Therefore this is a necessary requirement.

Clean upper half of recoil spectrum If the mother nucleus decays via other branches then the transition of interest, a superposition of recoil spectra with different endpoint energies will be created. Since only the upper half of the recoil spectrum of interest will be used for the fit, the side branches of a good candidate have a sufficiently low decay energy such that their recoil spectrum falls outside the interesting range.

Half-life The half-life should be of the order of seconds or less in order to restrict the total measurement period to reasonable time scales.

Production yield In order to perform a recoil energy measurement in a reasonable time, the production yield should be of the order of 10^7 ions/s. The effect of the ISOLDE yield on the total measurement time will be discussed in more detail further down (8).

Superallowed $0^+ \rightarrow 0^+$ decays

The superallowed $0^+ \rightarrow 0^+$ decays have been studied intensively over the last decades in order to test the Conserved Vector Current hypothesis. In this context the properties of the following twenty transitions are known quite well: ^{10}C $\rightarrow$ ^{10*}B, ^{14}O $\rightarrow$ ^{14*}N, ^{18}Ne $\rightarrow$ ^{18*}F, ^{22}Mg $\rightarrow$ ^{22*}Na, ^{26m}Al $\rightarrow$ ^{26}Mg, ^{26}Si $\rightarrow$ ^{26m}Al, ^{30}S $\rightarrow$ ^{30*}P, ^{32}Ar $\rightarrow$ ^{32*}Cl, ^{34}Cl $\rightarrow$ ^{34}S, ^{34}Ar $\rightarrow$ ^{34}Cl, ^{38m}K $\rightarrow$ ^{38}Ar,

^{38}Ca → ^{38m}K, ^{42}Sc → ^{42}Ca, ^{42}Ti → ^{42}Sc, ^{46}V → ^{46}Ti, ^{50}Mn → ^{50}Cr, ^{54}Co → ^{54}Fe, ^{62}Ga → ^{62}Zn, ^{66}As → ^{66}Ge, ^{70}Br → ^{70}Se, ^{74}Rb → ^{74}Kr.

The requirement of having a stable daughter nucleus eliminates ^{10}C, ^{14}O, ^{18}Ne, ^{22}Mg, ^{26}Si, ^{30}S, ^{32}Ar, ^{34}Ar, ^{38}Ca, ^{42}Ti, ^{62}Ga, ^{66}As, ^{70}Br, ^{74}Rb. The isotope ^{50}Mn has not been rejected due to the extremely long half-life of its daughter. From the 21 candidates 7 are left, being listed in table 3.3 together with their most important parameters. Appendix C contains a more detailed table of the transition data including the β branch with the highest recoil energy.

At present the isotopes ^{14}O, ^{42}Sc, ^{46}V and ^{54}Co are not produced at ISOLDE. For ^{26m}Al and ^{50}Mn, the production yield is too small to allow an experiment in a reasonable measurement period. Therefore with the present yields one $0^+ \rightarrow 0^+$ candidate isotope remains: ^{38m}K.

In principle the ground state decay of ^{38}K contaminates the upper half of the recoil spectrum of ^{38m}K. The longer half-live of the ground state (7.636 min) with respect to the isomeric state (0.923 s) and the fact that the branching ratio for this decay is smaller than 0.61% implies that after 2 s the ratio of decays from ground over isomeric state is of the order of $5 \cdot 10^{-5}$ for an equal initial population. For this reason it can be neglected.

Mirror transitions

Apart from those pure Fermi decays the superallowed mirror transitions of odd-even nuclei can also yield information about a possible scalar-type weak interaction. A disadvantage of those decays is that the sensitivity of a on the coupling constants C_S and C'_S decreases when the Fermi to Gamow-Teller mixing ratio y decreases, as can be seen from equation 2.4. As was shown in figure 2.3 if one would obtain for the $\beta - \nu$ coefficient the a_{SM}-value with a precision of 1% the possible contribution of Y_S is 11.2% for a decay with $y = 2$ in stead of 10% for a pure Fermi decay, corresponding to a loss of sensitivity of about 10%. Limiting then the list of superallowed mirror transitions to the decays that have a mixing ratio higher than 2 results in two good candidates: ^{33}Cl → ^{33}S and ^{35}Ar → ^{35}Cl. Their most important parameters are also listed in table 3.3.

Table 3.1: Properties of the candidate isotopes for a scalar current search in nuclear beta decay with the WITCH set-up. ΔE is the energy difference between the initial and final state. Columns 2,3 and 5 are obtained from Firestone and Shirley (1996), 4 from ISOLDE collaboration (2003), and 7 from Navilat-Cuncic *et al.* (1991).

mother	$t_{1/2}$ (s)	spin ($\hbar$)	Yield (part/s)	ΔE (MeV)	T_r^{max} (eV)	y	a_{SM}
^{26m}Al	6.345	0	$3.95{\cdot}10^4$	4.232	281	∞	1
^{34}Cl	1.525	0	$1.26{\cdot}10^3$	5.492	388	∞	1
^{38m}K	0.923	0	$6.3{\cdot}10^6$	6.0435	429	∞	1
^{42}Sc	0.68	0	0	6.425	444	∞	1
^{46}V	0.422	0	0	7.0514	497	∞	1
^{50}Mn	0.283	0	$7.6{\cdot}10^5$	7.633	542	∞	1
^{54}Co	0.193	0	0	8.24309	592	∞	1
^{33}Cl	2.511	3/2	$1.41{\cdot}10^2$	5.583	415	3.463(52)	0.897(3)
^{35}Ar	1.775	3/2	$2.1{\cdot}10^7$	5.9653	453	-3.674(68)	0.908(3)

Since the Standard Model value of the β-ν angular correlation parameter a_{SM} depends on the mixing ratio y, the achievable precision on a is limited by the accuracy on y. Navilat-Cuncic *et al.* (1991) list a number of mirror transitions with the experimental ft value as well as the mixing ratio, determined from the experimental ft value. For the two decays mentioned above the contribution in the error of a_{SM} is 0.003 due to the mixed character of the transition. It should be clear that this systematic error will only have a limiting effect when one would be able to push the accuracy of the set-up to the promille level.

Chapter 4

REXTRAP and its beam

Before exploring the WITCH set-up in detail it is instructive to spent a few words on the source that delivers the radioactive beam: REXTRAP. This chapter will provide a short overview on the REXTRAP set-up and its beam. Penning trap related parameters will be mentioned but not explained so far. A more detailed discussion into the different aspects of a Penning trap can be found in chapter 6. Since the properties of the REXTRAP beam define the requirements for the beamline of the WITCH set-up, a characterization will be performed by means of the quantity called emittance. This can be interpreted as a measure of the quality of the beam. Both experimental as well as simulation results will be discussed. To conclude a short section will be spent to the optimization of the REXTRAP Penning trap to maximize the transfer efficiency to the WITCH set-up.

4.1 REXTRAP set-up

REXTRAP is the cylindrical Penning trap of the REX-ISOLDE facility that acts as a cooler and buncher of the DC ISOLDE beam. The complete REXTRAP set-up is placed on a HV platform at 60 kV to allow capturing the 60 keV ISOLDE beam while applying only low voltages on the trap electrodes. After

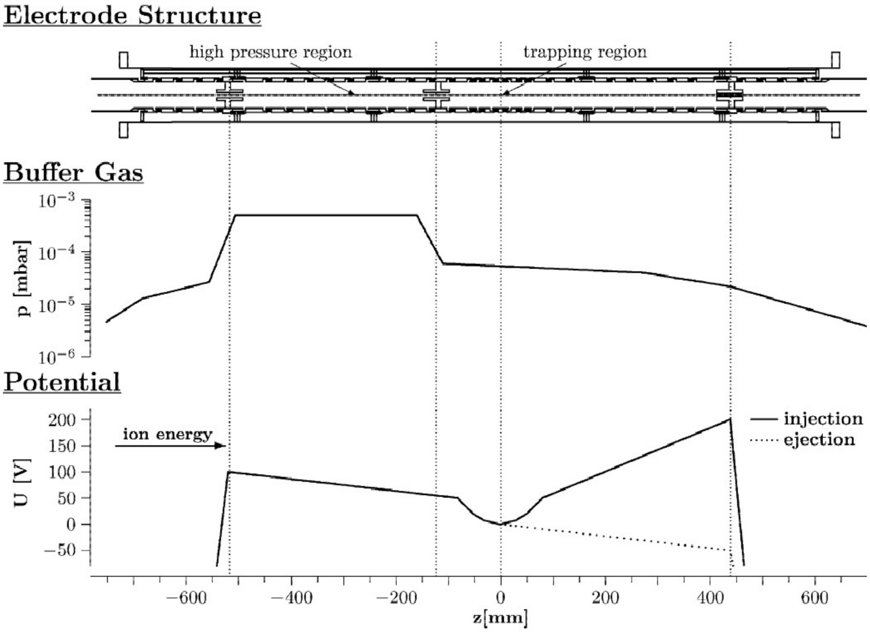

Figure 4.1: Electrode structure, voltage and buffer gas pressure distribution of the REXTRAP set-up (from Schmidt (2001)).

buffer gas cooling of the trapped ion cloud, the ion bunch is ejected. This cycle is repeated with a frequency of 50 Hz. The bunched 60 keV beam is transferred to an EBIS (Electron Beam Ion Source) where highly charged ions are bred. Those ions are then post-accelerated up to energies of 0.8-2.2 Mev/u and are used for experiments in the field of nuclear structure and nuclear astrophysics.

The REXTRAP electrode structure that is placed inside a 2.975 T superconducting magnet system consists out of two sections, a deceleration stage and a Penning trap structure. In the first section the ions loose energy by means of collisions with Ne or Ar buffer gas atoms at a pressure of about $1 \cdot 10^{-3}$ mbar. After they have lost the main fraction of their kinetic energy, the ions will end up in the potential minimum of the second section, the Penning trap. Figure 4.1 gives an overview of the electrode structure of the REXTRAP-set-up with buffer gas pressure and electrostatic potential at different positions.

Table 4.1: Main characteristics of the REXTRAP Penning trap.

Parameter	Unit	Value
B	T	2.975
$D = U_0/d^2$	V/m^2	$3.5 \cdot 10^4$
p_{buf}	mbar	$3.2 \cdot 10^{-4}$
ϕ_{elec}	mm	40

Once the ions are captured inside the Penning trap the ions are cooled and centered. Two techniques are being employed to decrease the ion clouds phase space: buffer gas cooling and rotating wall cooling. The cooling is performed during a period of 20 ms in a buffer gas pressure of roughly $3.2 \cdot 10^{-4}$ mbar. Experiments have been performed on stable and radioactive ions covering a mass range between ^{7}Li and ^{238}U. An efficiency of about 40% has been reached (Ames *et al.*, 2002). The most important characteristics of the REXTRAP set-up are summarized in table 4.1.

4.2 Phase space and emittance

In order to describe the dynamics of extended collections of charged particles the concept of phase space is a very powerful tool. A single particle is represented by one point in the 6-dimensional phase space (x, p_x, y, p_y, z, p_z) where the z-axis represents the propagation direction of the beam. A collection of particles, like a beam, occupies a volume in phase space. If the particle distribution is sufficiently dense, forces acting on the particles vary smoothly in space and time (there are no collisions) and frictional forces are excluded, then it can be shown that this phase space volume is conserved, as explained by Humphries Jr. (1990). For certain applications the aim is exactly to violate this conservation theorem and reduce the phase space volume occupied by a beam or a collection of charges. As will be discussed in chapter 6 the reduction of the phase space volume of an ion cloud in a Penning trap can be performed by the collisions with buffer gas atoms inside the trap volume resulting in a frictional force.

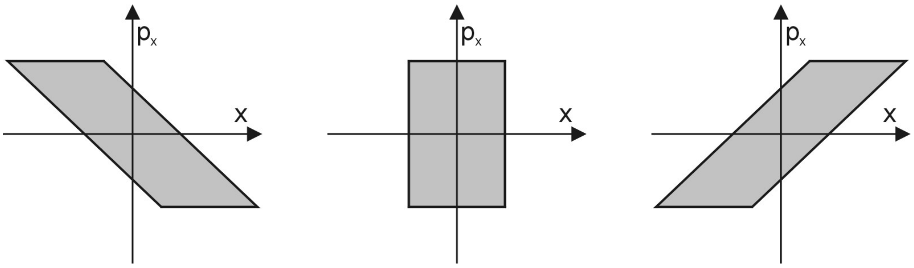

Figure 4.2: Evolution of the phase space diagram in the x-direction for a converging beam when no force is applied.

To obtain pictures that can be visualized phase space is usually projected into the two dimensional planes: $(x, p_x), (y, p_y), (z, p_z)$. This type of plots will be called action plane projections or action diagrams following Moore *et al.* (1995). As an example figure 4.2 shows the evolution in the x-direction for a converging beam on which no force is applied. The central figure is called a (spatial) focus and it is characterized by a minimal spread in the x-coordinate. If the phase space diagram has an elliptical shape, the two principle axes are parallel to the x or the p_x axis.

Emittance is a quantity that is closely related to the volume/area that the beam takes in phase space, as will become clear further. It represents in a way the quality of the beam. In the definition of emittance one makes a distinction between the transversal (x, y) and longitudinal (z) direction. The word quality should in the transversal context be interpreted as the focusability or the parallelism of the beam. Longitudinal emittance is only meaningful when one has to do with a bunched beam. Quality refers here to the energy and time spread of the beam in the propagation direction. A whole variety of definitions exist when it comes to the quantity emittance. The definitions that are given in this work are based on references (Humphries Jr., 1990; Moore *et al.*, 1995).

4.2.1 Transversal emittance

Since velocity or momenta can normally not be measured directly, emittance is defined in the so-called trace space (x, x', y, y') where $x' = p_x/p_z$ and $y' =$

p_y/p_z. Emittance is then the area of the smallest ellipse that circumscribes the distribution of beam points in trace space divided by π.

$$\epsilon_x = \frac{1}{\pi} \int \int_{ellipse} dx dx'. \tag{4.1}$$

In y-direction a similar formula holds. To indicate that the definition of emittance contains the division by π the unit of emittance is $\pi \cdot mm \cdot mrad$.

Since trace space plots of beams are typically elliptical a practical formula can be applied, in the case of a spatial focus, which relates the beam width Δx and divergence $\Delta x'$ to the beam emittance:

$$\Delta x \cdot \Delta x' = 4\epsilon_x. \tag{4.2}$$

In some cases this definition of emittance is not completely unambiguous since a real beam has no clear envelope in phase space. A practical definition is to define the emittance as the area of the ellipse containing a certain percentage of the total particle number (80 or 95% depending on the author).

If the beam is accelerated along the z-axis, then the angle x' will decrease resulting in a decrease of the transversal emittance. So it is important to specify the beam energy with the emittance. The concept normalized emittance exists in order to accomodate for this effect and to allow a quantitative comparison of the beam quality at different acceleration stages. This will however not be discussed here.

4.2.2 Longitudinal emittance

In the propagation direction of the beam it is not meaningful to define an angle as was the case for the transversal case. Therefore the longitudinal emittance is referred to as the area being occupied by the beam in the (z, p_z) plane divided by π. Under the assumption that the momentum spread of the beam is small compared to its central momentum, it can be shown that this area is equal to the product of the energy spread ΔE and the time spread Δt in a so-called time focus. In analogy to a spatial focus, a time focus is characterized by a minimal time spread of the action diagram in (E, t)-space. In this way the longitudinal emittance can be expressed as

$$\epsilon_L = \Delta E \cdot \Delta t \, \pi \cdot eV \cdot \mu s \tag{4.3}$$

The presence of the factor π in the unit refers to the same convention as mentioned earlier.

The concept longitudinal emittance is important when one is dealing with bunched beams. Often it is the case that certain components of a set-up have to be switched in a certain time window that is defined by the time and energy spread of the bunch. For the WITCH set-up this is the case when the beam is injected into the pulsed drift section of the vertical beamline and when it is injected in the cooler trap.

4.2.3 Emittance of the REXTRAP beam

Based on initial calculations the transversal and longitudinal emittance of the REXTRAP set-up was expected to be $\epsilon_T = 3\pi \cdot mm \cdot mrad$ (60 keV) and $\epsilon_L =$ 10 eV $\cdot\mu$s (Ames *et al.*; Schmidt *et al.*, 2002). The transversal emittance was determined from the final ion temperature (300K) and the estimated radial ion cloud distribution in the Penning trap. The longitudinal emittance was calculated from the axial dimension of the ion distribution and the accelerating fields for ejection. Later, simulations have been performed to study the emittance of REXTRAP for different ion cloud conditions (Schmidt, 2001). For the transversal emittance experimental results are available (Reisinger, 2002) as well, and are listed in table 4.2 together with the simulation results.

In a first series of simulations the ion cloud was assumed to be in thermal equilibrium with the Ar buffer gas at 300 K with ion energies that are Boltzmann distributed. In this approach no Coulomb interaction between the different ions is taken into account. The first three rows of table 4.2 show the result for three different ion types. Both emittances increase with increasing mass. This can be understood since the momentum distribution for heavier particles at the same temperature shifts to higher values.

In a second approach the starting conditions for the ejection process have been generated by a simulation of buffer gas cooling of the ions during 20 ms. After

Table 4.2: Emittance results of REXTRAP based on simulations (Schmidt, 2001) and measurements (Reisinger, 2002). The percentage thats is mentioned denotes the fraction of ions that is included in the phase space ellipse for the emittance determination.

Ion	T_{cool} (ms)	p_{trap} (mbar)	E (keV)	ϵ_T (π·mm·mrad)	ϵ_L (eV·μs)	Perc. %	Reference
^{23}Na$^+$	therm. equil.		60	0.19	1.39	95	Schmidt (2001)
^{39}K$^+$	therm. equil.		60	0.23	1.63	95	Schmidt (2001)
^{133}Cs$^+$	therm. equil.		60	0.37	3.41	95	Schmidt (2001)
^{133}Cs$^+$	20	$0.70 \cdot 10^{-4}$	60	8.4	340	95	Schmidt (2001)
^{133}Cs$^+$	20	$1.05 \cdot 10^{-4}$	60	3.4	68.6	95	Schmidt (2001)
^{133}Cs$^+$	20	$1.40 \cdot 10^{-4}$	60	1.5	20.5	95	Schmidt (2001)
^{23}Na$^+$	20	$70 \cdot 10^{-6}$	60	12.0	407	80	Schmidt (2001)
^{23}Na$^+$	20	$105 \cdot 10^{-6}$	60	8.0	188	80	Schmidt (2001)
^{23}Na$^+$	20	$140 \cdot 10^{-6}$	60	5.4	140	80	Schmidt (2001)
^{39}K$^+$	no	$3.1 \cdot 10^{-4}$	30	18.4		80	Reisinger (2002)
^{39}K$^+$	20	$3.1 \cdot 10^{-4}$	30	7.7		80	Reisinger (2002)

cooling, the ions are ejected out of the Penning trap. This was done for different buffer gas pressures. No Coulomb repulsion has been taken into account. Those results are shown in rows 4 to 9.

A comparison between both approaches shows that for the buffer gas pressures used the ion cloud is not yet in thermal equilibrium with the gas atoms after 20 ms cooling time. Even at the highest buffer gas pressure, both transversal and longitudinal emittance are still a factor of 4 and 6 away from the thermal equilibrium values in the case of ^{133}Cs$^+$ ions. For ^{23}Na$^+$ the situation is even worse which can be explained by an inefficient cooling since the ion mass is smaller than the buffer gas atom. Looking to the trend of the emittance as a function of the buffer gas pressure, one could clearly improve here by increasing the pressure. In the actual set-up the Ne buffer gas pressure is $3.1 \cdot 10^{-4}$ mbar, corresponding to a similar damping performed in the simulations.

For the transversal emittance of REXTRAP experimental results are available. The last two rows of table 4.2 list the mean value of the different measurements that are mentioned by (Reisinger, 2002). The results were achieved with a 30 keV beam with roughly $6 \cdot 10^5$ ions. As buffer gas Ne was used. First emittance measurements have been performed without buffer gas cooling on the ^{39}K$^+$ ion cloud. This gave an emittance of 18.4 π mm·mrad. Secondly buffer gas cooling has been applied for 20 ms. This decreased the emittance by a factor of 2.4. During the measurements the ion number has been varied between $1.4 \cdot 10^5$ and $7 \cdot 10^5$. No correlation between the particle numbers and the area of the phase space ellipse could be determined. Measurements with ion bunches containing 10^7 ions have shown a clear increase of the transversal up to ϵ_T=30 π mm·mrad (Ames, 2003).

In an attempt to compare the measurements with the simulations one should first of all scale the emittance by the beam momentum. Dividing the result in the last row of table 4.2 by $\sqrt{2}$ would then result in an emittance of roughly 5.4 π mm·mrad at 60 keV. Taking into account that the measured emittance ellipse only contains 80% of the ions, it can be concluded that the measured result is higher than the simulated value of ϵ_T. This difference is expected to originate from the electric repulsion between the ions which has been neglected in the simulations. This Coulomb repulsion causes a bigger ion cloud both in radial and in longitudinal direction, resulting in a more extended phase space area.

For the longitudinal emittance no measurements have been performed up to now. To get an idea of the time spread of an ejected ion bunch one could use the TOF measurements that have been performed after ejection out of REXTRAP. At 60 keV the time spread is 10μs for an ion bunch of 10^6 ^{39}K$^+$ ions (Ames, 2003). The energy spread of an ejected ion bunch can be estimated by taking into account the electric field gradient that is applied to eject the bunch (cfr. the bottom graph of figure 4.1). The voltage drop is approximately 50 V over 50 cm. Over the average length of 2cm for an ion cloud this corresponds to a decrease of 2 V. So conservatively the energy spread of the ion bunch can be estimated to be about 10 eV.

4.3 Optimization of the REXTRAP beam

The REXTRAP set-up has been optimized for delivering a 60 keV bunched beam to the REX-EBIS at a repetition rate of 50 Hz. To maximize the transmission efficiency from REXTRAP to the WITCH set-up, different parameters will have to be adapted. First of all one measurement cycle for the WITCH experiment will take of the order of seconds, so that there is more time available for cooling. This means for instance that one could run at a lower buffer gas pressure if such would be useful. Secondly the beam parameters in longitudinal direction should be adapted to have maximal transmission efficiency through the pulsed drift section. This means that one should try to decrease the time spread of the bunch coming from REXTRAP which limits the achievable efficiency as will be discussed in the next chapter. The two parameters that can be tuned are

- length of the ion cloud in axial direction
- ejection electric field

The axial dimension can be decreased by reducing the number of trapped ions. A second solution is to increase the depth of the trapping potential. This will force the ion cloud to expand into the radial direction. This will, however, also result into an increase of the transversal emittance which can limit the beam transfer efficiency as well. So a good balance has to be found here. The electric field gradient to eject the ion cloud from REXTRAP, which is shown in the bottom graph of figure 4.1, will induce an energy spread in the ejected ion bunch. To a certain extent this energy spread will influence the time spread of the beam.

Chapter 5

WITCH beamline system

The connection between the REXTRAP facility, which delivers a 60 keV cooled and bunched beam, and the actual WITCH experimental apparatus is made by a UHV beamline. This chapter describes this part of the set-up and is built up in a more or less chronological way. First the design phase with the simulation work will be discussed. This is followed by a detailed description of the electrode structure of the beamline as well as of the diagnostics system that is implemented at seven positions along the beam path. To conclude the first tests with the beamline system are illustrated and briefly discussed.

5.1 Design considerations

The radioactive ion bunches coming from REXTRAP have a kinetic energy of 60 keV. However, the actual injection of the ions into the WITCH trap potential is done at typical energies of tens to one hundred eV. This means that the ions have to be retarded before they are injected in the actual trap structure. In many cases the trap structure is placed on a ”hill of electrostatic potential energy”, as is the case for the REXTRAP set-up. In order to reach the trap the ions are retarded and in this way suitable injection energies can be reached. A disadvantage of this approach is that not only the trap structure but

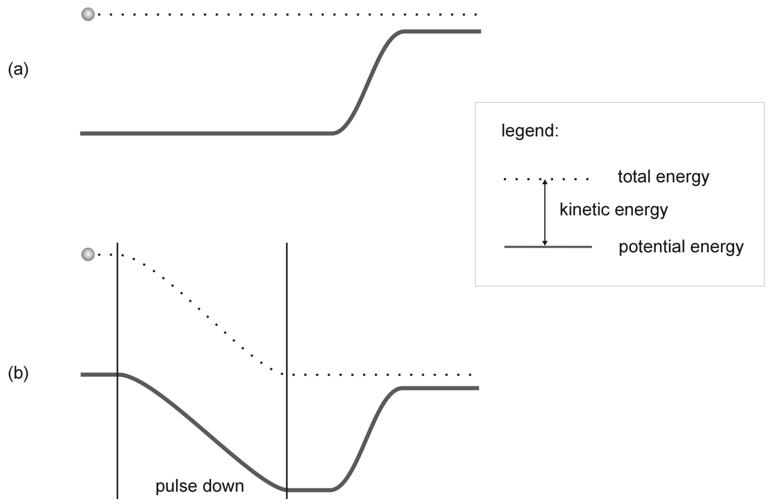

Figure 5.1: Schematic energy evolution during the retardation of an ion by means of a HV platform (a) and a pulsed drift section (b). It should be noted that a time evolution is implicitly included in figure (b).

the complete environment of the trap (i.e. magnet system, bore tube, pumps, electronics, etc...) has to be placed on a HV platform as is shown schematically in figure 5.1(a).

In contrast to the retardation that is essential for a successful injection of ions into the Penning trap, the use of the HV platform can be avoided by performing a trick (Herfurth *et al.*, 2001) as is shown schematically in figure 5.1(b). The trick is to shift the zero level of the electric potential down over a range that equals the initial kinetic energy of the beam such that the beam is fully retarded when it enters a region that is on ground potential. This can be done by pulsing down the potential of an electrode while the ion bunch is travelling through it. The kinetic energy of the ions will not be changed by this operation but when the bunch exits the drift section it will see a different potential energy level. The pulsed drift section trick has been realized at the ISOLTRAP experiment (Herfurth *et al.*, 2001) where, however, the potential energy is shifted in two steps. In the WITCH set-up the shift will be performed in one single pulsing. More details about the switching system will be given further down.

Apart from the retardation the ions also have to be injected into the magnetic field of the Penning trap. When a charged particle moves from a low to a high magnetic field region kinetic energy that is stored in the (axial) motion along the magnetic field lines is converted into radial energy [1]. If no axial energy is left before the charged particle has fully passed the electrostatic retardation in front of the Penning trap, the particle will be reflected. In this way the particle cannot be captured and is lost. In order to avoid magnetic reflection of the ions the radial energy that the ions gain should be minimized as much as possible. Therefore the ions have to be injected parallel to the magnetic field lines.

Apart from those two processes that had to be incorporated into the design, several practical considerations had to be taken into account. First of all the actual WITCH set-up is oriented vertically due to the limited floor space in the ISOLDE experimental hall. Secondly it was decided to keep some distance from the neighboring REX-ISOLDE facility to avoid possible disturbing effects like magnetic stray fields from the two superconducting magnets and X-rays from the RFQ linear accelerator. Therefore the WITCH beamline system consists out of a first section in the horizontal plane to provide the spatial separation which is followed by a vertical part in which the retardation and the adjustment of potential energy is performed.

5.2 Simulations

In order to realize the design of the beamline a series of ion trajectory simulations has been performed. The main effort spent was focussed on the realization of the two points mentioned above:

- incorporating the pulsed drift tube in the retardation section
- injection of the ions into the magnetic field

For this design study the commercial simulation package SIMION 3D 6.0 has been used. It uses a Runge Kutta method of fourth order with adaptive step size

---

[1] The inverse process that forms the basis of the working principle of the retardation spectrometer, will be discussed in more detail in chapter 7

to integrate the equation of motion (Dahl, 1995). Both electric and magnetic potentials are calculated by means of a relaxation method that uses the nearest neighbor points to estimate the potential in each point.

The starting point of the simulations is the spatial focus of the beam ejected out of REXTRAP just after the acceleration. The mono-energetic beam that was used for the simulations has a transversal emittance of 9 π·mm·mrad and the ions are uniformly distributed inside this ellipse.

5.2.1 Simulation results

To define the layout and the applied voltages of the retardation section with the pulsed drift cavity, two factors had to be taken into account that work in opposite direction. From one side it is preferable to retard the beam as much as possible before letting it enter the pulsed drift section. This increases the travel time of the ions into this electrode which relaxes the timing of the pulse-down and allows an ion bunch with a bigger time spread. The disadvantage of a strong retardation however is that the beam is focussed very strongly implying a strong divergence afterwards. An optimum between both effects was found by a partial retardation in front of the pulsed drift tube. The optimal situation that came out of the simulations was to retard the ions up to an energy of 8 keV before entering the pulsed drift tube. Afterwards the ion beam is retarded further down in two steps up to the drift energy of 1.5 keV. Figure 5.2 shows the trajectories of 100 ions passing through the retardation section of the vertical beamline. The simulation voltages for all electrodes can be found in appendix D. It should be noted that in this beamline simulation no timing is involved. The Penning trap structure as well as all drift electrode after the pulsed drift tube are placed on a HV platform. As a first approach this is expected to give the same results as when the pulsed drift tube electrode is switched.

To inject the ions into the magnetic field while limiting the radial energy pick-up, one of the electrodes can be used as an einzellens. By focussing the beam in the right way one can bring the ion trajectories parallel to the magnetic field lines. The simulations showed that it is possible with the lens approach to inject the beam into the Penning trap. It became also clear, however, that apart from the voltage on the focussing electrode, the voltages on the horizontal beamline electrodes are even more critical. This can be understood by noting that those electrodes define the initial orientation of the beam with respect to the vertical axis. Giving the ions a too high radial component when the beam is bent into the vertical direction cannot be compensated any more by the focussing electrode, in the absence of steerer plates for the simulation circumstances. On the right part of figure 5.2 the beam is shown when it enters the magnetic field.

The fact that the ions pick-up radial energy when moving towards the Penning trap cannot be avoided in practice since it is impossible to inject all ions perfectly parallel to the magnetic field lines. To determine the amount of radial energy that is gained by the ions the voltage on the trap electrode was varied in steps from 59.95 kV up to values above 60 kV while plotting the number of transferred ions for each voltage. Since this voltage is mostly an axial potential barrier the ions with high radial energy will be blocked already for low voltages. The evolution is shown in figure 5.3. The radial energy pick-up is of the order of tens of eV which is reasonable for allowing capturing. Surprisingly the injected fraction does not drop to zero when the trap structure is on 60 kV. This is expected to be due to inaccuracies in the calculations. Errors on the calculated energies of the order of some tens of eV are noted by the program which are of similar magnitude as what the discrepancy one can see on figure 5.3.

5.2.2 Refining of simulations

As the above mentioned study has been the first approach to simulate the beam trajectories inside the beamline system, it is clear that improvements can be made at different points. First of all it might be worth to include REXTRAP in the geometry and start the simulations by an ejection of an ion bunch with realistic properties. Secondly, it would be good to take into account timing. This would be especially helpful for studying the process of pulsing the pulsed drift tube. After transfer tests through the vertical beamline have been made a comparison with simulations might be extremely valuable.

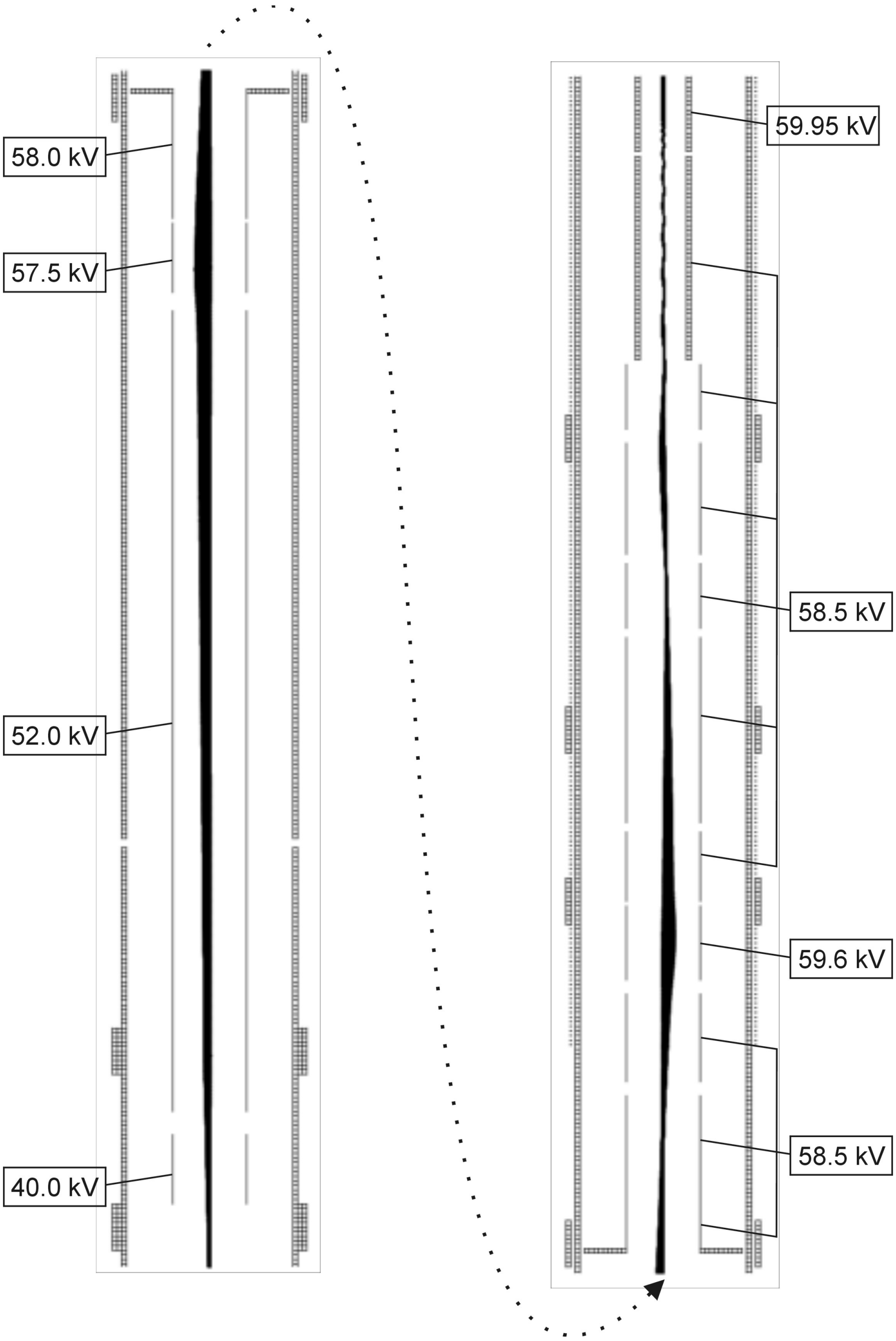

Figure 5.2: Simulated ion trajectories of a 60 keV beam of 100 ions with a transversal emittance ϵ_T=9π·mm·mrad.

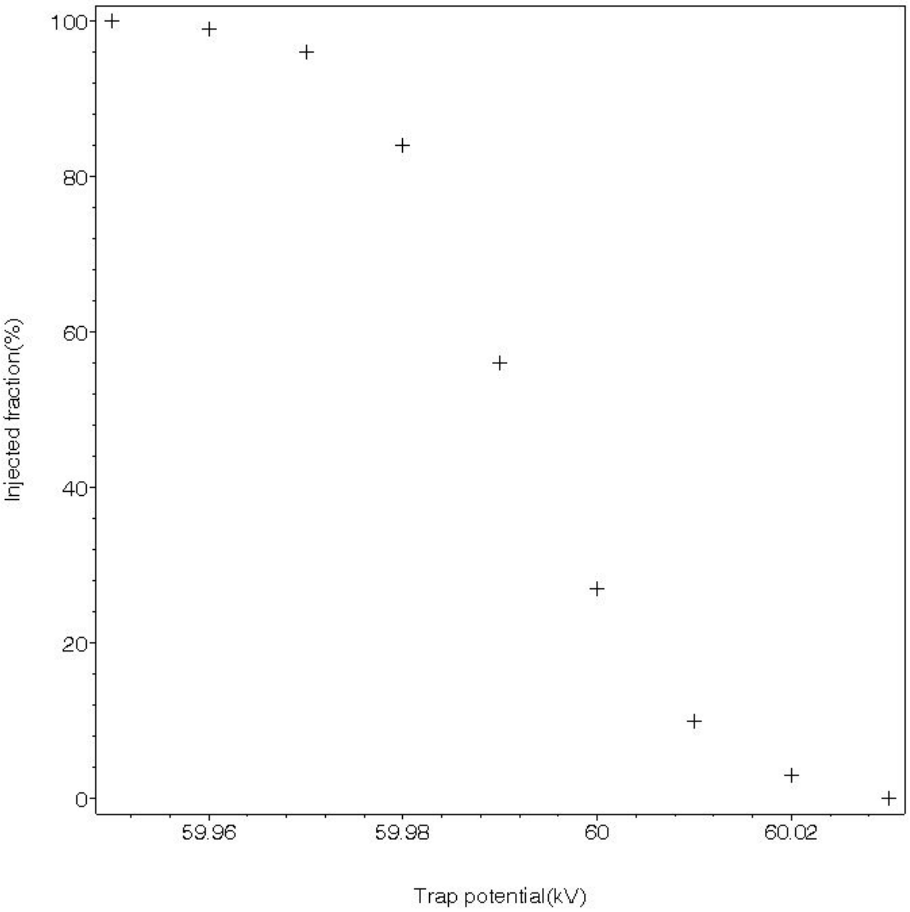

Figure 5.3: Injected fraction of ions as a function of the trap potential. Note that two neighboring points in the plot are only 10 V away from each other, although the x-axis scale is expressed in kV.

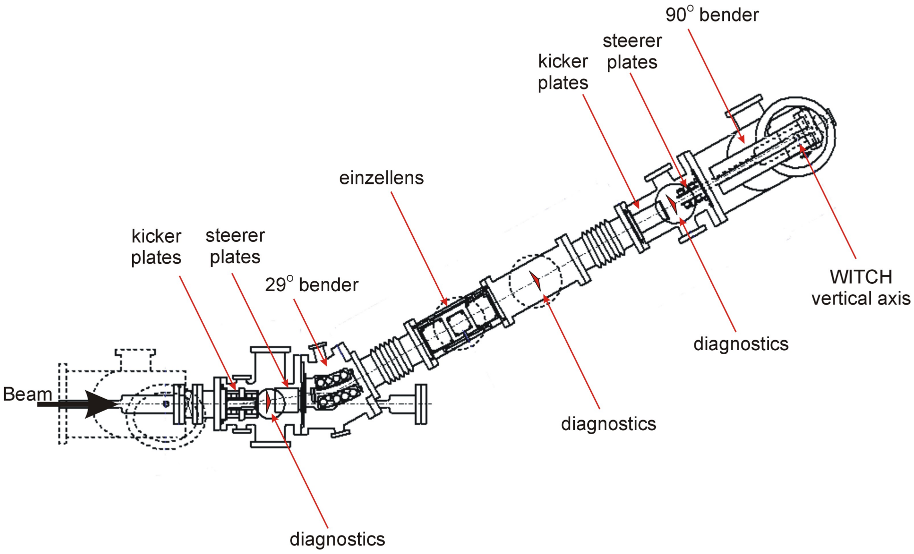

Figure 5.4: Overview of the horizontal beamline section (see text).

5.3 Electrode structure

In this section an overview will be given on the most important electrodes of the beamline and their function. A (natural) separation has been made between the horizontal and the vertical beamline. More details about all the electrodes can be found in appendix D. The diagnostics that is used in the beamline, will be discussed in section 5.4.

5.3.1 Horizontal beamline

The horizontal beamline section consists mainly out of guiding components for the 60 keV beam. An overview is given in figure 5.4. The main building blocks of the horizontal beamline are the two electrostatic kicker-bender combinations of which the second one is shown (in detail) in figure 5.5. The kicker that is located in front of the bender consists out of two parallel deflection plates of 60×60 mm^2 area with a gap of 3 cm (figure 5.6). Both plates are tilted over an angle of 3.75° with respect to the beam axis. The kicker acts as a beam switch

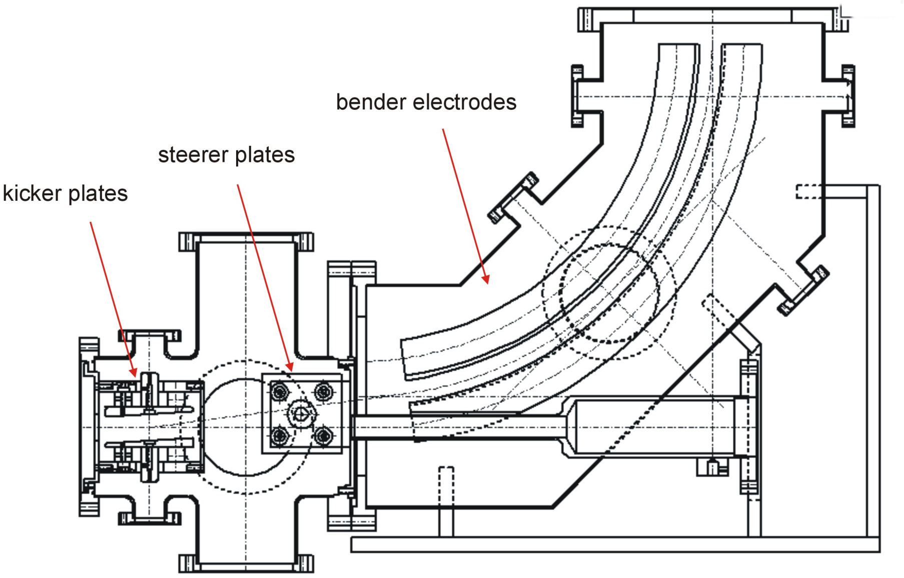

Figure 5.5: View of the different electrodes inside the kicker and 90° bender.

between two trajectories: applying the suited voltage on the plates, deflects the beam over an angle of 7.5° and guides it in between the electrodes of the bender that is positioned directly behind the kicker vacuum chamber 5.5. Keeping the kicker plates at ground potential lets the beam continue its trajectory without entering the electrostatic bender electrodes. The construction of the kicker and bender (figure 5.5) is based on the design of the REX-ISOLDE beamline that connects REXTRAP with the REX-EBIS.

The electrostatic bender, shown in figure 5.7 consists out of two spherical electrodes with a radius 385 mm for the inner electrode and 415 mm for the outer one. This spherical shape ensures that the beam which is bend at a radius of 400 mm is also focussed in the direction perpendicular to the deflection plane. This is an advantage over the so-called cylindrical deflector where the beam can diverge in this perpendicular direction. Although the two benders of the WITCH horizontal beamline will be called further 29° and 90° bender one should note that those angles represent the sum of the kicker angle (7.5°) and the actual bender angle (21.5° and 82.5° respectively).

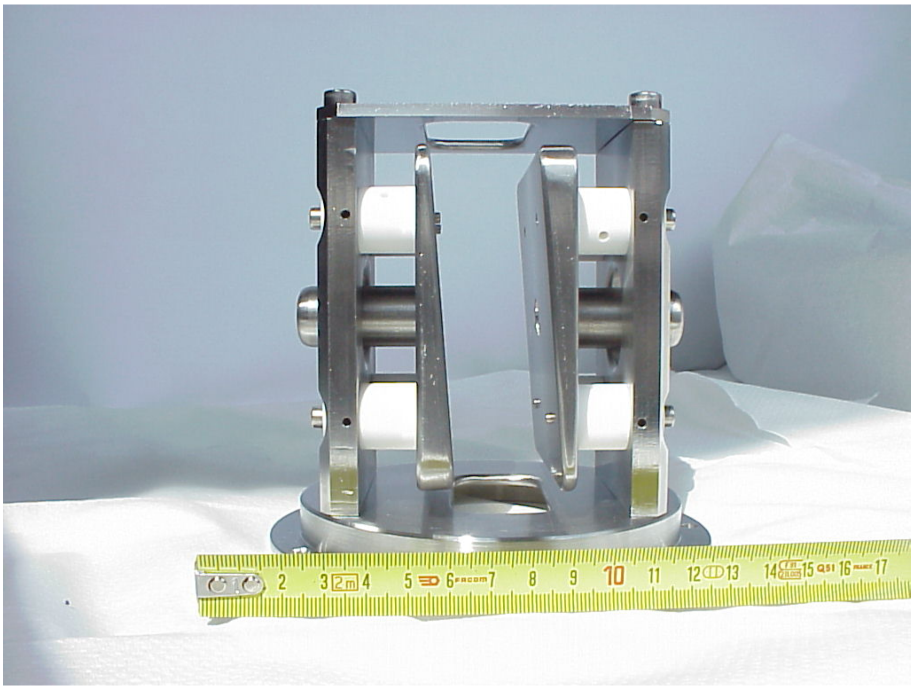

Figure 5.6: Picture of the kicker plates.

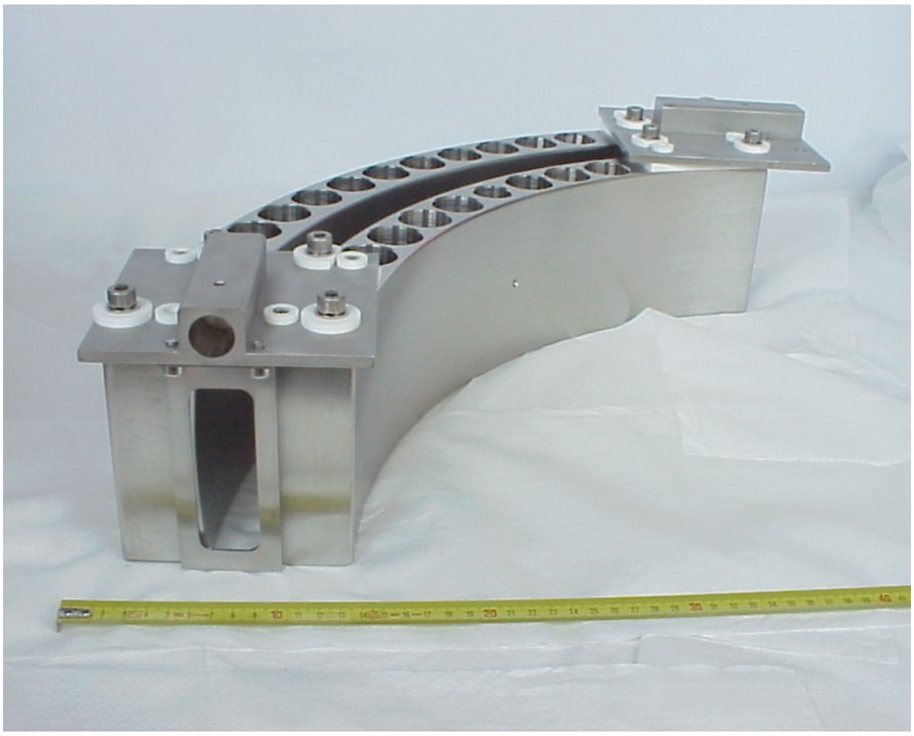

Figure 5.7: Picture of the spherical bender electrodes of the 90° bender.

Inside the kicker vacuum chambers, two steering plates are mounted to correct for small offsets of the beam perpendicular to the deflection plane of the kicker plates. In between the two electrostatic benders, an einzellens serves as focussing element for the 60 keV beam. Picture 5.8 shows the 3-electrode structure of the einzellens, the design of which was based on the REXTRAP einzellens that is installed just after the Penning trap. The two outer electrodes of the lens are on ground potential. The central electrode, on which the HV is applied, is supported by Macor bars.

At three positions in the horizontal beamline beam monitoring devices are foreseen: after each set of kicker plates and after the einzellens (figure 5.4. Those will be discussed in more detail in section 5.4.

The complete horizontal beamline section is one vacuum section. More details concerning the vacuum aspects can be found in appendix E. Figure 5.9 shows the horizontal beamline installed at the ISOLDE facility.

5.3.2 Vertical beamline

The vertical beamline is mainly built up out of stainless steel cylindrical electrodes with an internal diameter of 60 mm, as shown in figure 5.10. At four positions along this beamline two doublets of x-y steerer plates are foreseen to correct for possible beam shifts. All electrodes are electrically insulated from each other and from the vacuum chamber by Macor spacers. The complete electrode structure can be divided into two sections each having a specific function. In the actual realization they are separated by a valve.

In the first section the beam is retarded from 60 keV in four steps down to 1.5 keV. Furthermore this section contains the pulsed drift electrode that is used to shift the potential energy down over a range of 60 keV. The cavity which has a length of 78 cm is shown in figure 5.11. The lower part of the electrode can be removed from the main part. This was done for practical reasons, i.e. to allow that the beamline can be moved out of the set-up. The vertical beamline is installed on a rail system that allows a horizontal displacement of the vacuum chambers. In this way access is created to the bore tube inside the magnet system where the Penning trap structure is located.

Figure 5.8: Electrode structure of the einzellens of the horizontal beamline.

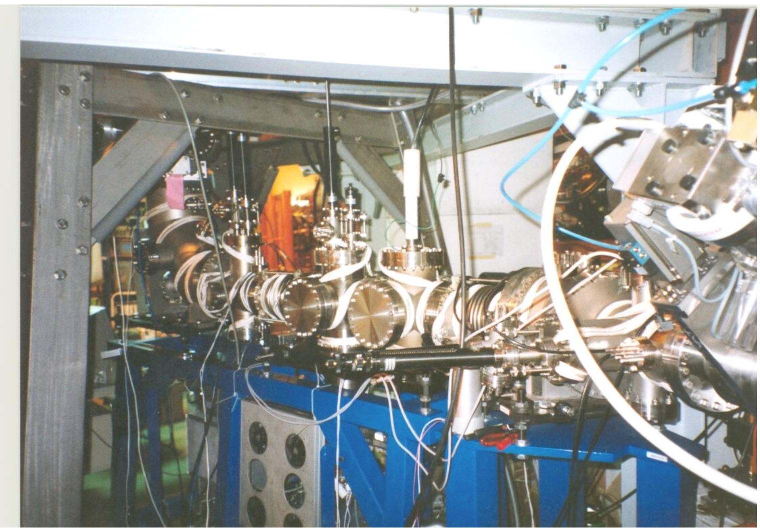

Figure 5.9: Picture of the horizontal beamline installed at the ISOLDE facility.

In the second section the electrode structure is designed to create a drift region with a potential of -1.5 kV. In this way the kinetic energy of the beam is 1.5 keV, the energy with which it is injected into the magnetic field. In stead of having one long electrode the drift region is split into different shorter components to provide flexibility during beam tuning. One of the electrode is used as an einzellens to focus the beam and force the ion trajectories to be parallel to the magnetic field lines.

Along the vertical beamline four diagnostics systems are installed. The positioning of them is shown in figure 5.10.

Pulsed drift section and HV switch

In order to shift the potential energy of the beam over 60 keV, the pulsed drift section has to be ramped down over a voltage difference of 60 kV while the ion bunch travels inside the electrode. Before going into details on how the fast pulsing down occurs and what efficiency one can reach with this approach it is

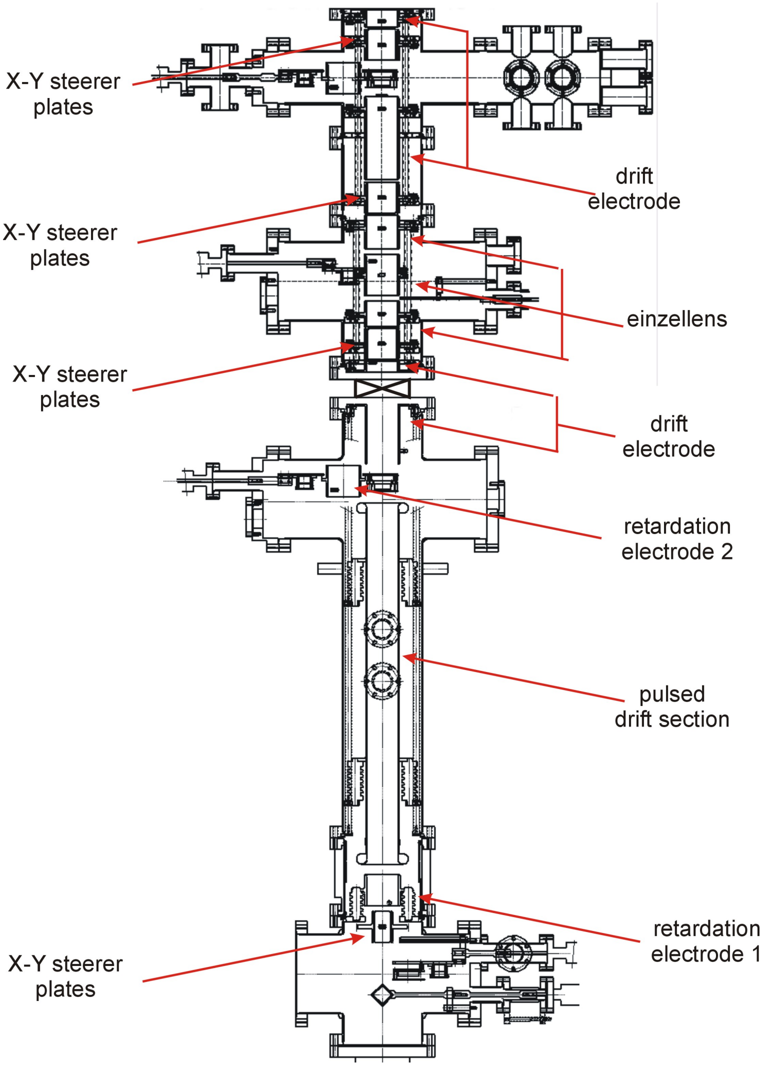

Figure 5.10: Overview of the vertical beamline.

Figure 5.11: Picture of the pulsed drift section with Macor insulators and its support structure.

important to raise the question: when has an ion successfully passed the pulsed drift cavity?

In the ideal case an ion enters the electrode before the start of the pulse down and leaves it after the voltage on the electrode is at the minimal value. In practice the pulse down process follows an exponential decay. Two ions leaving the pulsed drift tube at different times will end up with a relative energy spread, which decreases as the ions leave the pulsed drift electrode at a later time. Therefore one should define a maximal tolerable shift from the relaxation voltage which still allows successful injection into the cooler trap.

Apart from the energy spread caused by the pulsed drift tube, other sources of energy widening of the ion bunch have already been mentioned too. First of all the electric field gradient during ejection out of REXTRAP will result in an energy spread that was estimated to be about 10 eV in chapter 4. Secondly the magnetic field gradient converts axial into radial energy resulting in an additional spread in axial energy which is of the order of 50 eV as was shown by the simulations. In chapter 6 the total axial spread that can be tolerated for the capture process in the cooler trap will be estimated to be 100 eV for an ion bunch with a time spread of 10 μs entering the trap. This means that the energy spread due to the pulsing can be at most up to 40 eV. An ion passage through the pulsed drift section will therefore be considered as successful if the ion leaves the cavity when the electrode is less than 40 V away from the relaxation value.

Form the experimental side the critical parameters are the length of the cavity and the ramp down time that can be achieved. The time window in which the electrode should be pulsed down is defined by the two critical parameters of the ion bunches: the travel time of the ions through the electrode as well as the time spread with which they enter the pulsed section.

Based on a first timing estimate as well as ion optical and space considerations the length of the pulsed drift section was determined to be 78 cm. The travel time of the ions over this length varies from 3.3 μs for a 10 keV ^{35}Ar ion up to 10.5 μs for a 1 keV ion of the same mass.

The fast pulsing is realized with the scheme shown in figure 5.12, of which the key component is the HV switch (Behlke HTS650-03-LC). The initial voltage

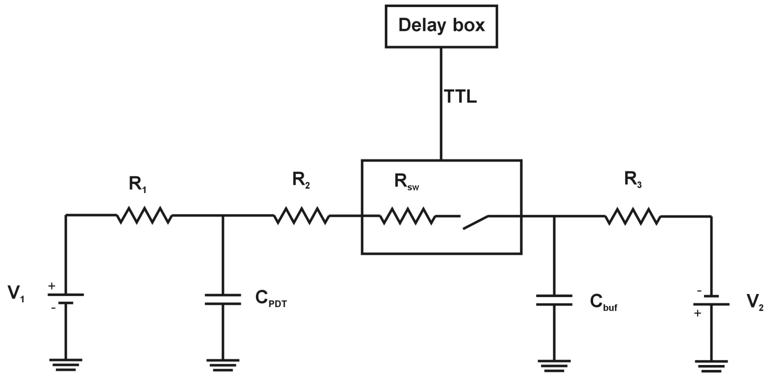

Figure 5.12: Electronic scheme of the switch box for the pulsed drift section. Values for the different components: R_1=600 MΩ, R_2=1500 Ω, R_{sw} = 360Ω, R_3 = 2000Ω, C_{PDT}=100 pF, C_{buf}=94 nF.

is supplied by a FUG HCN 6,5M 65000, the final voltage is supplied by a ISEG CPn100 105 24 5 UC power supply. The HV switch is triggered by means of a TTL-signal. The fall time of the drift section is determined by the parameters of the RC-ciruit: capacitance of the actual electrode (including cable), the resistor R_2 which limits the peak current and the internal resistance of the switch R_{sw}.

The total capacitance of the electrode and cable is assumed to be 100 pF. Figure 5.13 shows the ramping down of the voltage that is applied on the pulsed drift tube electrode for a series of design parameters resulting in four different time constants. The curve corresponding to the realised switch system has a time constant of $1.86{\cdot}10^{-7}$ s and will lie in between curves two and three. From this graph one can extract that starting from 1.5 μs after the start trigger the voltage will be closer than 40 V from the relaxation value of the circuit.

The rise time of the electrode after the switch has been closed, is defined by resistor R_1 (600 MΩ) as well as C_{PDT}. The electrode deviates less than 0.5 V from the initial value after 1 s. This value defines the repetition rate at which the system can run.

To allow successful pulse down of all ions the sum of the time spread of the ion bunch as well as the pulse down time of the electrode should be smaller

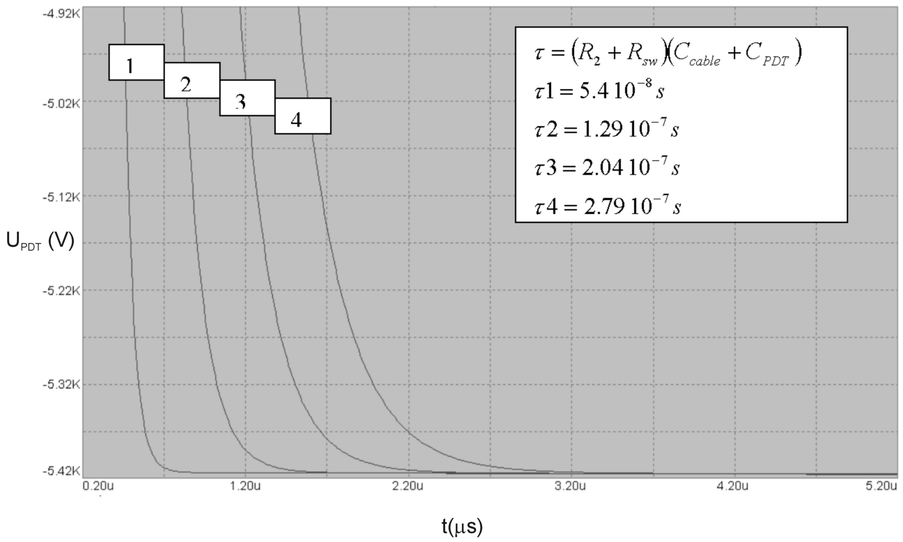

Figure 5.13: Potential evolution on the pulsed drift section for a ramp down started at t=0.2μs from an initial applied value of 55 kV to -5.5 kV.

than the travel time of an ion inside the pulsed cavity. Assuming that the drift energy of the ions in the cavity is the simulated value (8keV) resulting in a travel time of 3.7 μs and subtracting the pulse down time of 1.5 μs it is clear that in the current situation one can only handle a time spread of 2.2 μs. Assuming the time spread of the ions to be distributed as step function being 10μs wide, this corresponds to an efficiency of 22 %.

Improvements of the pulsed cavity efficiency can be performed in two ways. First of all the ramp down time should be decreased further. Secondly one should work on the beam tuning such that the drift energy is smaller resulting in a longer travel time. This will also increase the transmission efficiency. Finally a decrease of the time spread of the ion bunch ejected out of REXTRAP would also improve the situation.

5.4 Beam monitoring system

At seven positions along the complete beamline it is possible to monitor the beam intensity. Each diagnostics system consists of two components: a collimator and a detector. The collimation of the beam is performed in two ways which are explained in more detail in the next section. Depending on the beam intensity one can use a Faraday Cup or a micro channel plate as detector.

5.4.1 Collimator system

The reason to introduce a collimator system with adjustable opening is threefold. First of all the collimator, if aligned precisely, defines the center of the beamline. This reference can then be used to determine the possible spatial shift of the beam and afterwards correct for it. This is especially important when injecting a beam of charged particles in a strong magnetic field where the minimization of the radial energy pick-up is crucial. Secondly it is advantageous that one can change the opening of the collimator. Starting with a large opening, after maximizing the transmitted current by tuning the electrode voltages, one can then decrease the opening and repeat this operation. This iterative process will allow to gradually improve the tuning. Finally the adjustable opening will also provide a rough estimate of the spot size of the beam at that particular location. This can be extracted from the beam intensities measured for different openings. For the WITCH beam diagnostics two collimator solutions have been developed and implemented: a strip with holes of different diameter and a rotating cube. Which type of collimator system is used at a certain location is shown in figure D.1 and D.2.

Collimator strip

The first collimator system which is used at five of the seven positions consists out of a stainless steel plate with 4 holes with different diameter (3, 5, 8 and 20 mm). By means of a linear motion feed through (Caburn-MDC E-BLM-275-6) the strip can be moved forth and back to put a different collimator hole in front of the beam. The orientation of the linear feed through can be adjusted in order

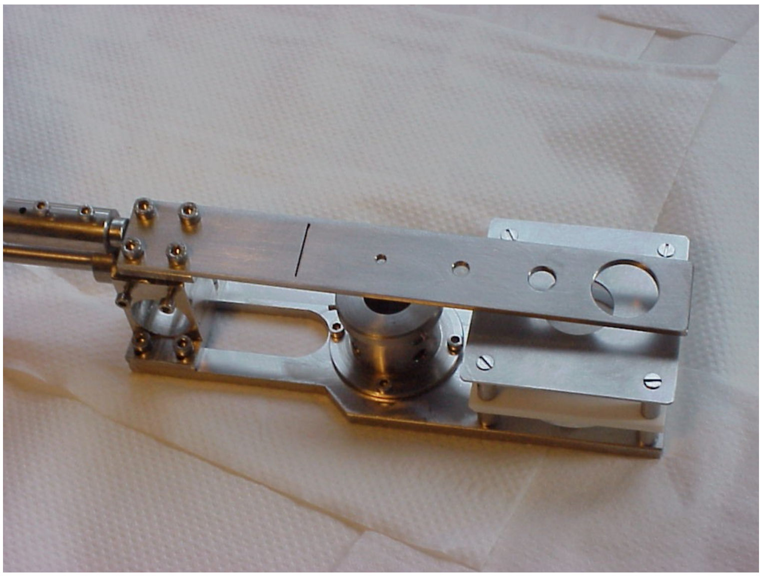

Figure 5.14: Collimator strip system for beam diagnostics.

to correct for misalignment of the flange on which it is mounted. Internally a guiding system is foreseen to prevent the long structure from bending and to keep it nicely positioned. The position of the holes with respect to the beamline axis was checked by means of a theodolite which allows an accuracy of 0.3mm. Figure 5.14 shows a picture of the strip collimator system. The strip has also a slit of $20{\cdot}1\ \mathrm{mm}^2$, which allows a scan of the beam profile in one direction.

Disadvantages of this system are the restriction to a discrete number of collimator openings and the relatively high cost due to the need for a linear motion feed through. The big advantage is its very small dimension (thickness of 3mm along the beam path) as well as the possibility to make a beam profile scan in one direction. One could think of a system in which one has two strips moving in mutually perpendicular directions. In this configuration one could make a 2 dimensional beam profile scan that would give valuable information during the tuning. This would correspond, however, to a significant additional cost and require additional space.

Rotating cube

The design of the second collimation system allows to vary the collimator opening continuously. It consists out of a hollow stainless steel cube with an external rib r_1 of 30 mm of which two opposite sides with an area of $25 \cdot 25$ mm^2 are open to allow the beam to pass (see figure 5.15). The cube can be rotated by means of a rotational motion feed through (MDC-Caburn E-BRM-275) around an axis that crosses the center of two opposite ribs of the cube which are parallel to the open axis. By a rotation of the cube the opening through which the beam can pass is then decreased gradually and in two directions. The evolution of the opening as a function of the rotation angle goes as

$$\begin{aligned} x &= \frac{1}{2}\left(\sqrt{2}r_2 \cos\theta - r_1 \sin\theta\right), && (5.1) \\ y &= \frac{1}{2}\left(\sqrt{2}r_2 \theta - r_1 \tan\theta\right), && (5.2) \end{aligned}$$

where θ is the rotation angle, r_1 the external rib of the cube and r_2 the rib of the squared opening. This dependence is shown in figure 5.16. The decrease of the opening evolves differently for the x and y directions. However, the difference is much smaller than for other geometries like the cylindrical one. The area of the opening is then given by the double product of x and y.

The advantage of this system is that one can continuously change the opening. A disadvantage of the rotating cube collimator is its size, which makes it inapplicable to the vertical beamline and the kicker chambers. The alignment of the cube is also less straightforward in comparison with the strip system.

Further improvement

The first tuning tests have clearly shown the need to find out in which direction the beam is off-axis such that one can correct the electrode voltages in the good sense. This is not possible with the cube collimator, however. The strip system allows a determination of the shift but only along the linear feed through axis.

This could be solved by the use of an additional slit in the strip that makes

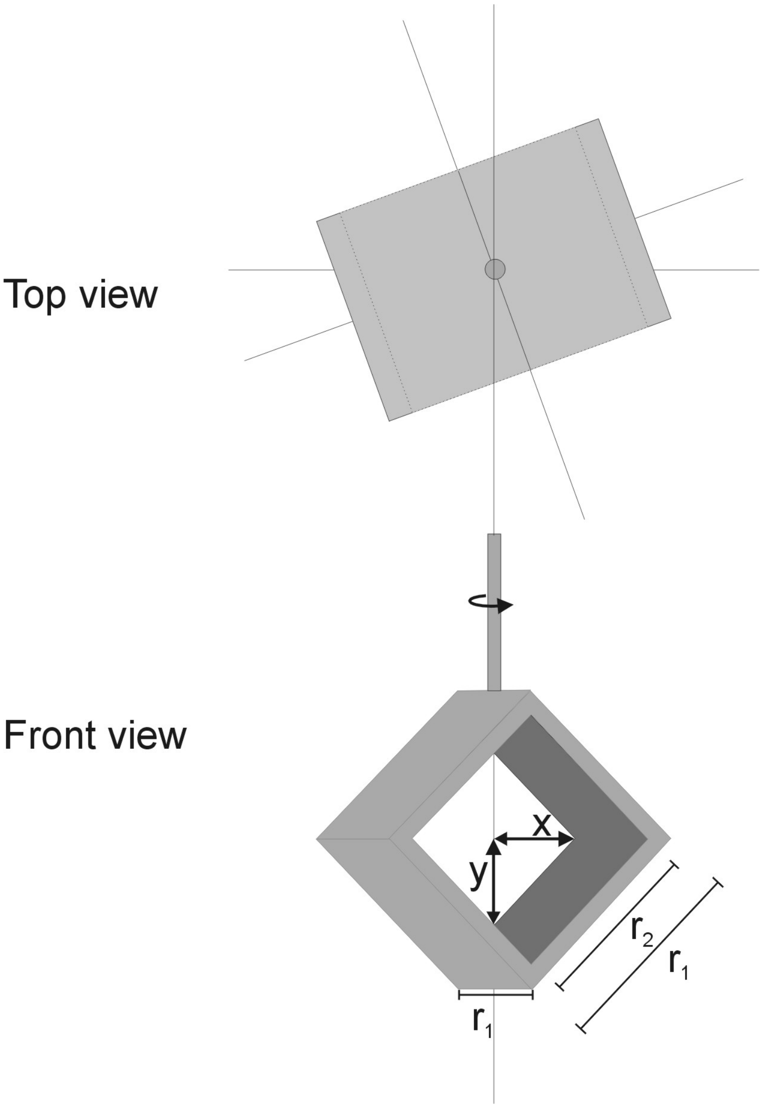

Figure 5.15: Rotating cube collimator system with $r_1 = 30mm$, r_2=25mm.

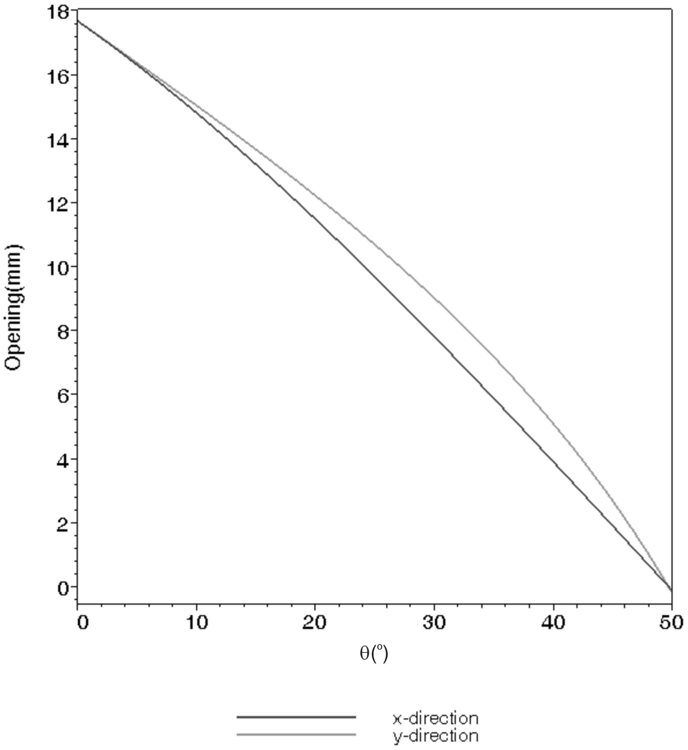

Figure 5.16: Cube-collimator opening in two dimensions as a function of the rotation angle.

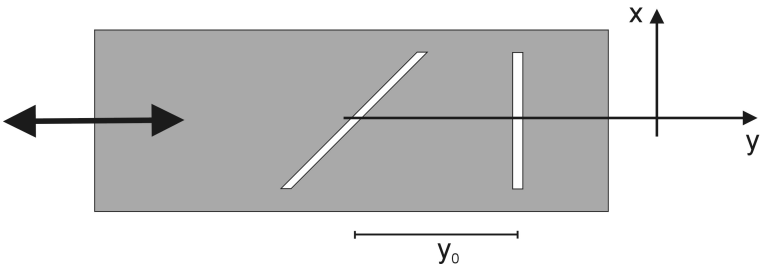

Figure 5.17: Slit system to measure a beam shift in a direction perpendicular to the motion axis.

an angle of 45° with respect to the axis of the motion feed through and is stretched such that it has the same width in x-direction, as shown in figure 5.17. With the straight slit one first makes a beam profile scan to find the point y_1 with maximal current along the y-axis of motion. To determine the shift x_0 of the center of the beam a scan with the 45° slit should be performed. If y_0 is the distance between the center of the two slits and y_2 is the point where the maximal intensity is observed with the rotated slit, then the shift $x_0 = y_0 - (y_2 - y_1)$. The sign x_0 gives the sense of the shift.

5.4.2 Detectors

Two different detectors are installed at the different beam diagnostics positions to monitor the beam. For low beam intensities (from single ions up to 0.1 pA DC beam) an MCP detector can be used. Larger currents (starting from a few pA) can be measured with a Faraday cup.

At all positions the MCP detector and the Faraday cup are installed on one common support that can be moved in and out by means of a linear motion feed through (Caburn-MDC E-BLM-275-6). In the horizontal beamline the diagnostics supports slide forth and back by means of cylindrical stainless steel bearings (Caburn-MDC ALMB-1). This system is shown in figure 5.18.

In the vertical beamline section the situation is somewhat more complicated since a series of cylindrical electrodes on which the drift potential is applied blocks the access to the beam region. In order to move in a detector, one of

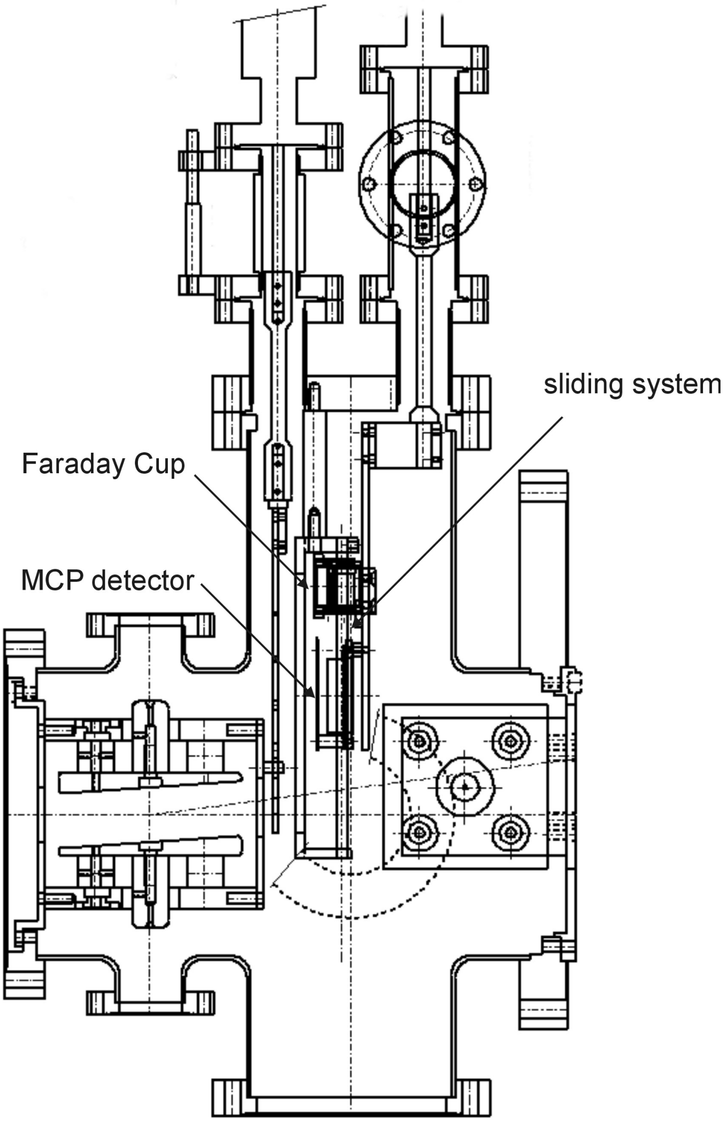

Figure 5.18: Diagnostics system of the horizontal beamline.

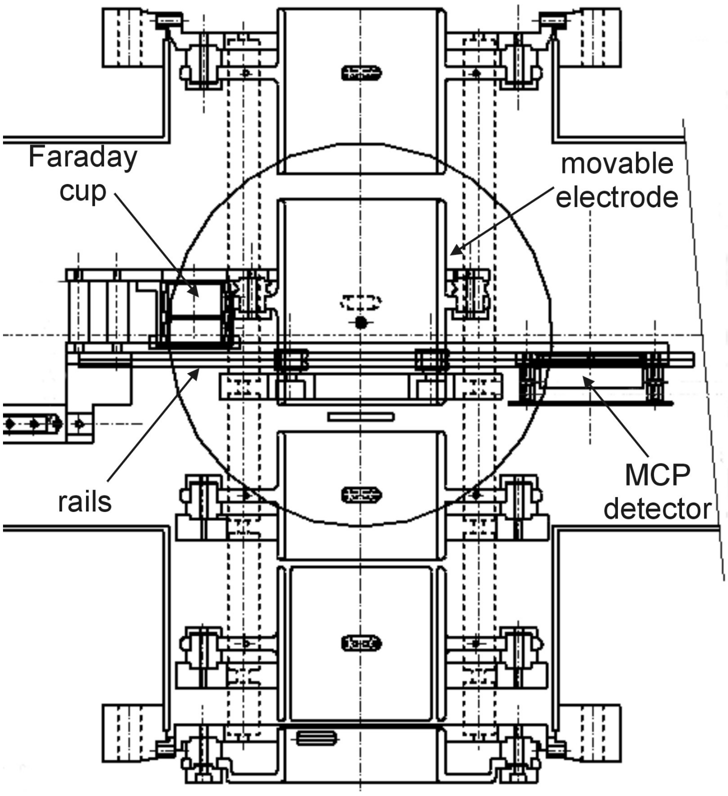

Figure 5.19: Diagnostics system of the vertical beamline.

the electrodes has to be moved out. To allow an easy and precise motion the detectors and the drift electrode are therefore fixed on a common support that moves by means of four stainless steel wheels (HEPCO SSLJ13CNS/ENS) over a rail system (figure 5.19).

Faraday Cup

The stainless steel Faraday cups consist out of an anode and a repeller electrode that are insulated by Macor pieces from the grounded cover. The cylindrical opening of the Faraday cup has a diameter of 16.5 mm. On the anode the ion

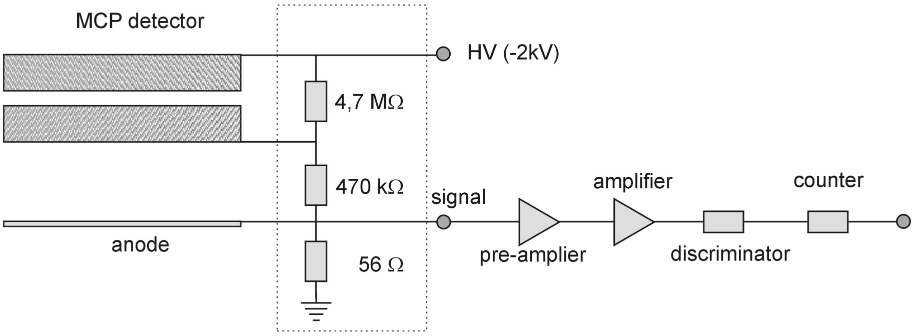

Figure 5.20: Electronics to operate the MCP detector.

current is measured directly by a Picoamp meter. On the repeller electrode a negative voltage of several tens of volt is sufficient to reflect the secondary electrons emitted after the ion impact back into the anode.

Micro Channel plate

The micro channel plate detector consists of a glass plate with many small and parallel channels that are oriented under an angle of roughly 10° with respect to the direction perpendicular to the surface. Each channel has a semiconductor coating and serves as an electron multiplier. A potential difference of approximately 1 kV is applied over front and back plane of the micro channel plate to accelerate the secondary electrons that are created by the impact of a projectile particle. The secondary electrons are collected on a metal anode, which is located from the backside of the MCP. Quite often MCP detectors contain two or three micro channel plates. This increases the intensity of secondary electrons. The detectors that are used for beamline diagnostics have a sensitive area with 2 cm diameter. The electronics to operate the MCP detector is shown in figure 5.20.

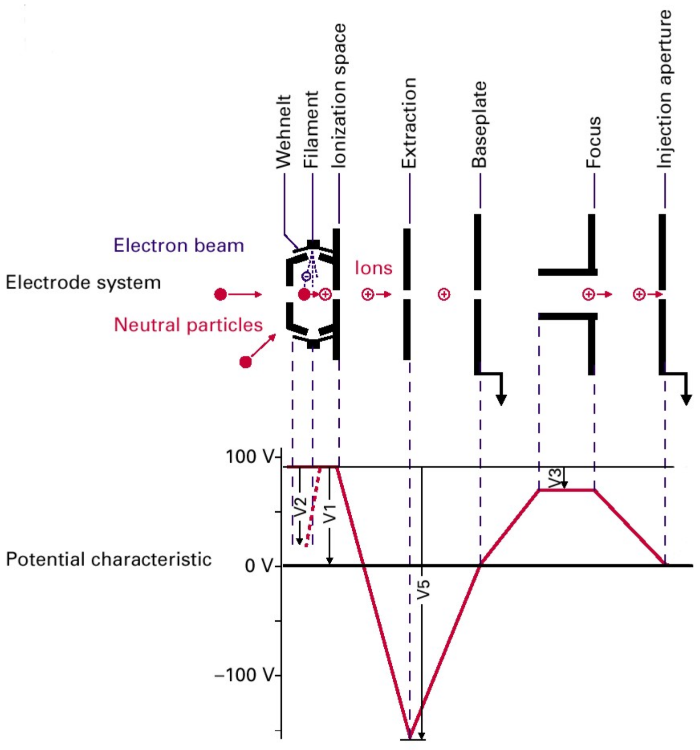

Figure 5.21: Schematic overview of the operation of both the ion source and the voltage that have to be applied on the different electrodes.

5.5 Off line ion source

The testing and optimization of the trapping procedures is performed by using a stable ion beam. The REXTRAP facility has an off-line ion source that is able to produce alkali ions by surface ionization similar to the system described by Dezfuli *et al.* (1996). This ion source is however also used to optimize and tune the REX-ISOLDE post acceleration facility. In order to allow tests independent from the REX-ISOLDE experiment an off-line ion source was installed in the vertical beamline section of the WITCH set-up.

The source is a commercial cross beam ion source from Pfeiffer (BN846481-T)

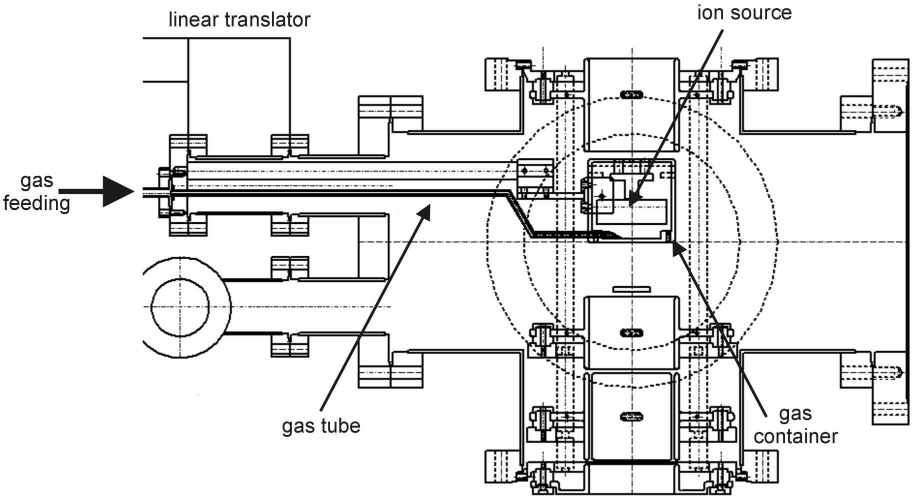

Figure 5.22: Overview of the positioning of the ion source inside the vertical beamline.

that is used in mass spectrometers for gas analysis. The ionization is performed by electron bombardment of gas atoms. Figure 5.21 gives an overview of the working principle of the ion source. Electrons are produced by heating one of the two thungsten filaments. These electrons are accelerated up to an energy of about 70 eV in the direction of the ionization chamber. Due to the electron impact the gas atoms that are present are ionized. They are then extracted out of the ionization chamber and focussed by a lens electrode.

In order to protect the vacuum of the beamline against the gas that is to be ionized, the source itself is placed in a cubic stainless steel box with an outlet hole of 3 mm diameter. The gas is inserted into this box through a small copper tube with inner diameter of 2 mm. A needle valve allows to control the gas flow that is inserted towards the box, which is directly related to the amount of ions that are produced. Both the ion source box and the gas inlet are fixed to a flange that can be moved in and out by means of a linear translator (Thermo Vac. Gen. ZLTM100). Because of space restrictions the einzellens electrode has to be pulled back before moving the ion source in. The positioning of the ion source inside the beamline is shown in figure 5.22.

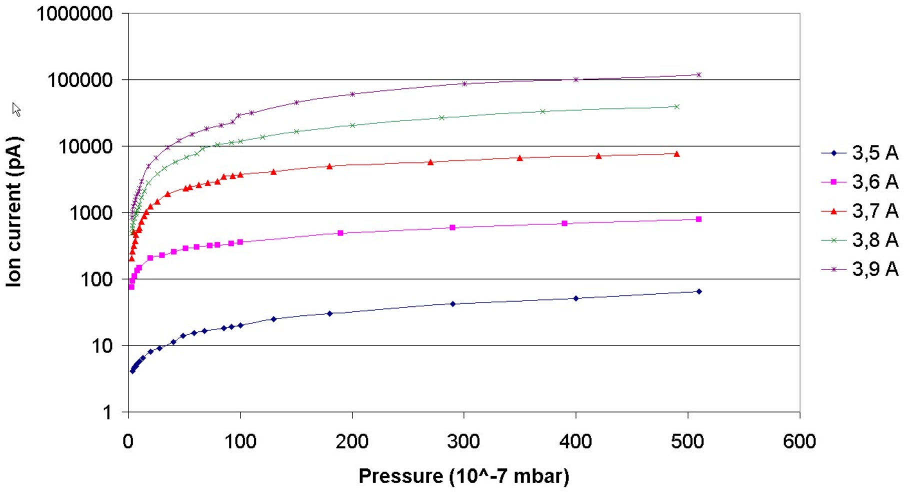

Figure 5.23: Ion current produced by the off-line ion source as a function of the pressure for different filament currents. The ion current was measured with a Faraday cup.

During off-line test measurements the characteristics of the ion source have been investigated. As an example figure 5.23 shows the ion current that has been produced for different pressures and filament currents. Note the wide ranges of ion currents that can be produced.

The ion source delivers a DC beam. The beam coming from REXTRAP is however a bunched beam. In order to create similar circumstances one could pulse one of the ion source voltages from its normal value to a higher value such that the current coming from the ion source is zero. This might be implemented in the future.

5.6 Transfer test

The beamline system of the WITCH set-up has been tested up to the first diagnostics point in the vertical beamline. The commissioning was performed with a 12 pA $^{39}K^+$ beam with an energy of 59.8 keV. The ions have been produced with the off-line ion source of the REXTRAP set-up. The beam was cooled during 20 ms in a Ne buffer gas environment at a pressure of $3.2 \cdot 10^{-4}$ mbar. The first 0.7 ms of this period were used for accumulation. The bunches have been ejected from REXTRAP with a repetition rate of 50 Hz. Fluctuations of 5 to 10 % in beam intensity have been observed. The pressure in the horizontal beamline section was $2.7 \cdot 10^{-7}$ mbar during this transfer test.

The beam was transported through the horizontal beamline and up to the first diagnostics point in the vertical beamline section without any significant loss. Through out this trajectory the beam has been monitored at the 3 diagnostics points in the horizontal section and at the first vertical beamline diagnostics. The result is summarized in figure 5.24. The fact that the intensity at the second diagnostics decreases by roughly 20 %, is expected to originate from a shift and/or a significant width of the beam causing it to exceed the circular opening of the FC (diameter 16 mm). At the diagnostics further down stream, no such losses have been observed. The voltages applied during the test can be found in appendix D.

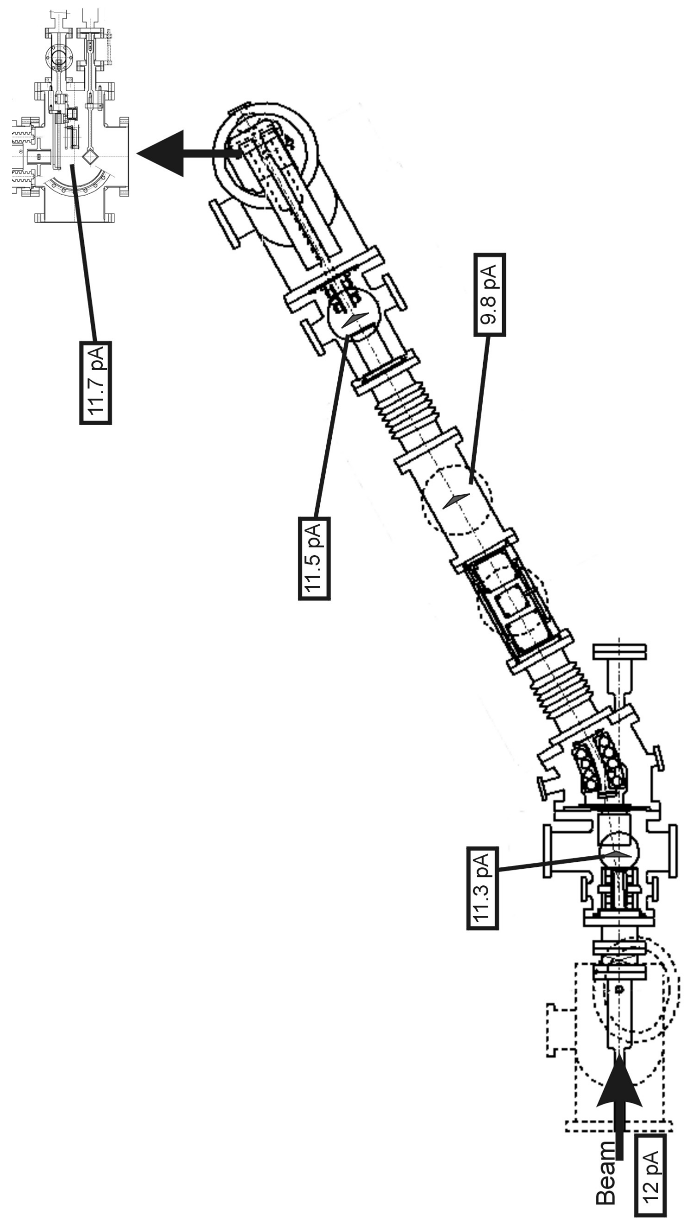

Figure 5.24: Results of the horizontal beamline transfer test.

Chapter 6

WITCH Penning trap structure

This chapter is dedicated to the Penning trap section of the WITCH set-up. A first section is devoted to the working principle of a Penning trap. This is done by means of a description of the motion of an ion in the confining electromagnetic fields of the trap. The buffer gas cooling technique that allows to reduce the phase space volume of the ion cloud will be described as well. As soon as more than one ion is present in a Penning trap the Coulomb repulsion between the ions will start to play a role. This is of special importance for the WITCH set-up which will store of the order of 10^6 ions in the Penning trap. Both experimental as well as simulation results will be discussed to point out how the Coulomb repulsion changes the one-particle description of the ion motion. Furthermore the simulation approach provides an estimate on what ion cloud dimensions can be expected in a Penning trap for certain ion numbers. Also the field of non-neutral plasmas will be briefly touched, where the one-particle picture is abandoned and looks to the collective behavior of the ions in the trap. After a detailed description of the WITCH Penning trap structure the chapter is concluded by a brief schematic picture on how to inject ions into a Penning trap.

6.1 One ion in a Penning trap

The original use of magnetic and electric fields to increase the time that electrons remain within a discharge (Penning, 1936) has been greatly refined over the years. The equations of motion of one single charged particle inside a Penning trap can be solved analytically and the particle dynamics is very well understood leading to extremely high precision experiments. In this work an overview will be given of the motion of an ion in a Penning and some excitation schemes. Derivation of the formulas will not be given, but can be found in the literature, e.g. Brown and Gabrielse (1986); König *et al.* (1995).

6.1.1 Ion motions in a Penning trap

A Penning trap makes use of a strong magnetic field $\mathbf{B} = B\mathbf{e_z}$ to confine charged particles in a plane perpendicular to the magnetic field axis. Confinement along the z-axis is performed by an electrostatic quadrupole potential of the form

$$U(r,z) = U_0 \frac{z^2 - r^2/2}{2d^2}. \tag{6.1}$$

The most natural electrode structure that generates this quadratic potential is the one of the so-called hyperbolic Penning trap. It consists out of three hyperbolically shaped electrodes as shown in figure 6.1 that coincide with equipotential surfaces of the trapping potential 6.1. In this respect U_0 represents the potential difference that is applied between the central ring electrode and the two end caps. By defining d as

$$d = \sqrt{(z_0^2 + r_0^2/2)/2} \tag{6.2}$$

with z_0 and r_0 the shortest axial and radial distance from the center to the end cap respectively ring electrode, one has a quantity that represents the trap dimension. The quadrupole potential can also be generated by a set of cylindrical electrodes. In this case the parameter d looses its meaning as trap dimension. For this type of traps the ratio U_0/d^2 is a good measure for the depth of the well and will be represented throughout this work by the symbol D. For positively charged ions the applied potential U_0 should be positive to allow successful trapping. As is imbedded in equation 6.1 and graphically

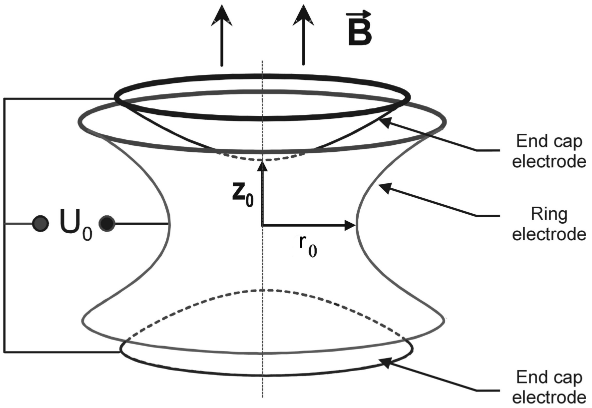

Figure 6.1: Most simple electrode structure of a hyperbolical Penning trap.

shown in figure 6.2 an axial potential well corresponds to a radial hill. The radial outward pointing electric field will affect the motion of the trapped ion in the radial plane.

By solving the equations of motion of a charged particle in the electromagnetic fields of the Penning trap, it can be shown that the motion is a superposition of three uncoupled motions (see figure 6.3). In the axial direction the particle can be described as a harmonic oscillator with frequency

$$\omega_z = \sqrt{\frac{eU_0}{md^2}}. \tag{6.3}$$

In the radial plane the well-known circular motion of a charged particle in a homogenous magnetic field is modified due to the radial outward pointing electrostatic field from the trapping potential. This results into an epicyclic motion which is composed out of two components: the reduced cyclotron motion(frequency ω_+) and the magnetron motion (frequency ω_-). The frequencies are given by

$$\omega_\pm = \frac{1}{2}\left[\omega_c \pm \sqrt{\omega_c^2 - 2\omega_z^2}\right] \tag{6.4}$$

For typical trap parameters the frequencies have the following hierarchy

$$\omega_c \approx \omega_+ >> \omega_z >> \omega_-. \tag{6.5}$$

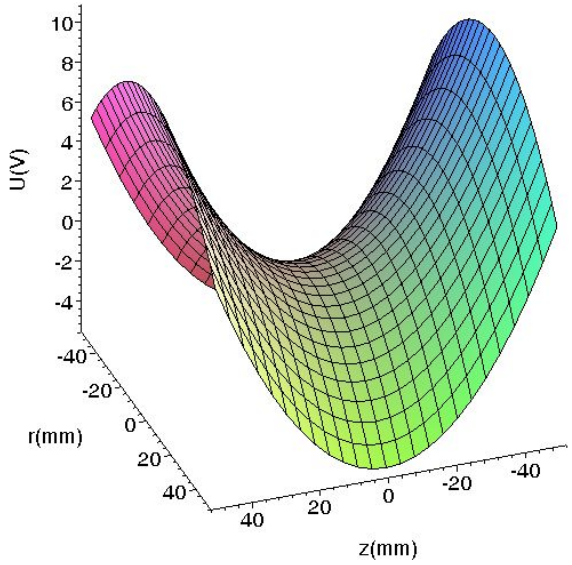

Figure 6.2: Electric quadrupole potential of a Penning trap with d =34.4mm and U_0=10V.

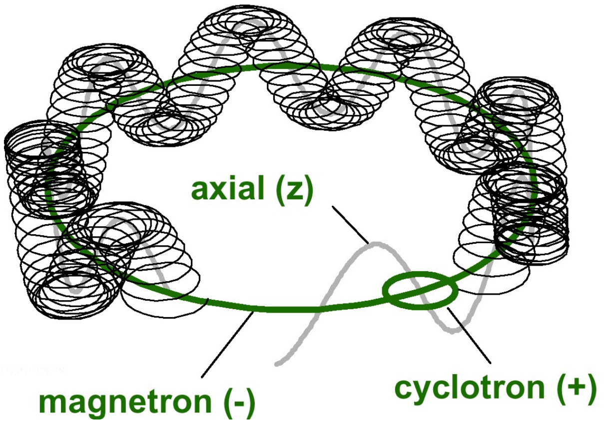

Figure 6.3: Motion of an ion in an ideal Penning trap that can be decomposed into the uncoupled magnetron, axial and reduced cyclotron.

As an example table 6.1 lists the motional frequencies for three isotopes in the WITCH Penning trap. Equation 6.4 also shows that

$$\omega_c = \omega_+ + \omega_-. \tag{6.6}$$

The fact that this sum frequency, being the pure cyclotron frequency ω_c, is mass dependent, provides the mass-selectivity of the buffer gas cooling technique that is described below. In contrast to ω_z and ω_+ the magnetron frequency is to first order independent of the mass. Using equation 6.4 one can show that

$$\omega_- = \frac{U_0}{2Bd^2} \tag{6.7}$$

Irrespective of the mass of the trapped ion the magnetron frequency is a measure for the trap depth D. In the case of REXTRAP ν_-=950 Hz (Ames, 2003) resulting into $D = 3.5 \cdot 10^4$ V/m^2. For the ISOLTRAP cooler trap ν_-= 307 Hz (Beck, 1997) meaning that $D = 1.8 \cdot 10^4$ V/m^2.

Apart from its low frequency and mass independence, the magnetron motion differs in another way from the two other motions and this by the fact that it is a meta-stable motion that describes a circular orbit around the radial potential hill. When energy is removed from it, the magnetron radius thus increases and the ion can eventually get lost on the electrodes. This feature needs special attention when it comes to cooling the ion motion.

Table 6.1: Motional frequencies for different 1^+ ions in the WITCH Penning trap with parameters B =9T, D=$1.817 \cdot 10^4$ V/m^2.

Isotope	ν_-(Hz)	ν_z(kHz)	ν_+(MHz)	ν_c(MHz)
^{26}Al	161	41.3	5.31	5.31
^{35}Ar	161	35.6	3.95	3.95
^{38}K	161	34.2	3.64	3.64

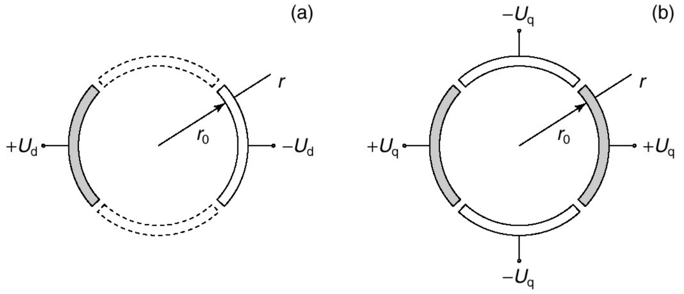

Figure 6.4: Application of a dipole (a) and quadrupole RF field (b) on the segmented ring electrode for excitations of the radial motions in a Penning trap.

6.1.2 Excitation of the ion motion

The fact that the ion motion can be decoupled into three independent eigenmotions makes the manipulation of the ions in the Penning trap highly selective. By applying time varying electric fields with the right RF frequencies one can affect one or two of the three eigen motions leaving the other(s) unaffected. The two most common excitation schemes use a dipole or quadrople electric field. To allow those excitations on the radial motion the ring electrode has to be split into two respectively four pieces. Figure 6.4 shows the electrode segmentation for a dipole (a) or quadrupole excitation (b) in the radial plane.

Dipole excitation

In order to excite one of the three motions one can apply an electric dipole field with the same frequency as this motion. In the radial plane this can be done with a dipole field given in

$$\mathbf{E_x} = E_d \cos(\omega_d t + \phi_d)\mathbf{e_x}, \tag{6.8}$$

with frequency ω_d. The immediate evolution of the motion will depend on the relative phase between the ion motion and RF field. On a longer time scale the net result is, however, always an increase of the radius as is described by Kuckein (2002).

Dipole excitations are used to drive ions out of the center. By performing a magnetron dipole excitation one can do this for all ions at the same time since the magnetron frequency ω_- is to first order mass independent. Mass-selective excitation can be performed at the reduced cyclotron frequency ω_+.

Quadrupole excitations

Apart from exciting a single ion motion, one can also couple two different motions. This can be done by a quadrupole RF field. Coupling the magnetron and the reduced cyclotron motion in the radial plane can be performed by the RF modulated electric field

$$\begin{aligned} E_x &= \frac{U_q}{2a^2} y \cos(\omega_q t + \phi_q) \\ E_y &= \frac{U_q}{2a^2} x \cos(\omega_q t + \phi_q), \end{aligned}$$

where U_q corresponds to the maximal RF potential on a circle with radius a.

Starting from a pure magnetron motion a quadrupole excitation at the RF frequency $\omega_q = \omega_+ + \omega_-$ induces a periodic conversion of the pure magnetron motion into the reduced cyclotron motion and back. The time period of this process is given by

$$T_B = \frac{4\pi a^2}{U_q} \frac{m}{q} (\omega_+ - \omega_-) \tag{6.9}$$

which depends linearly on the inverse of the applied RF amplitude.

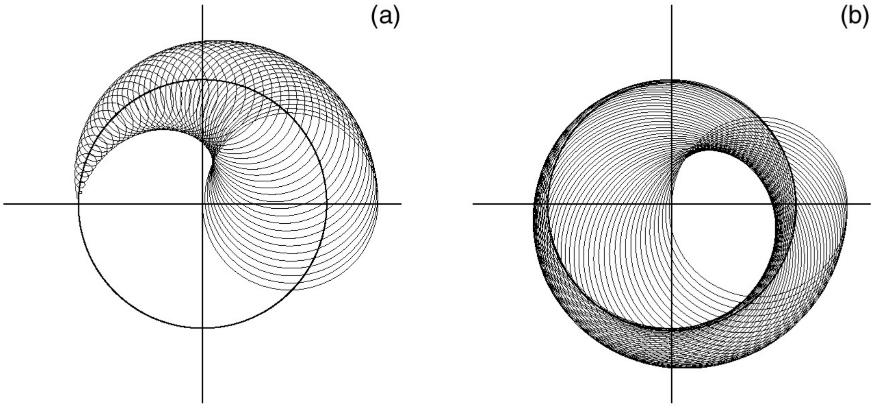

Figure 6.5: Conversion of a pure magnetron motion (a) into a reduced cyclotron motion (b) by means of a quadrupole excitation at frequency $\omega_c = \omega_+ + \omega_-$.

A detailed description of this conversion can be found in (König *et al.*, 1995). Since the conversion is performed with an RF field at the pure cyclotron frequency ω_c this process is mass-selective. As will be discussed later this feature allows to perform mass-selective buffer gas cooling of the ion cloud in a Penning trap. Figure 6.5 shows the conversion of an initially pure magnetron motion into a pure cyclotron motion.

6.1.3 Cooling of the ion motion

As discussed in chapter 4 the dynamics of a collection of charged particles can be described in phase space. As long as one deals with conservative forces, the volume that the particles occupy in phase space remains constant. In general, experiments performed with trapped particles benefit from ion clouds with small phase space volumes (i.e. small dimensions and small momentum/energy spread) because it reduces all kinds of systematic effects. The same is true for the WITCH experiment. As will be discussed in chapter 7 the spatial extension of the ion cloud might lead to a different response of the spectrometer for different initial ion positions. Secondly a minimal ion energy in the Penning trap is favorable since the energy analysis cannot separate this from the recoil energy which the ions obtain from the β-decay.

A reduction of phase space can be performed by using non-conservative forces that can dissipate the energy into a thermal bath. Various mechanisms are available for this energy transfer. Resistive cooling of light particles has been achieved by damping the signal induced in a tuned circuit by the particle motion (Brown and Gabrielse, 1986; Van Dyck Jr. *et al.*, 1984). For heavy ions, this method is not practical since the signals are proportional to the velocity of the stored particles and hence too small, resulting in long cooling times. Laser cooling of ions has also been demonstrated (Wineland *et al.*, 1987) but are only applicable on some elements with suitable optical transitions, i.e. mainly alkaline elements. Collisions with buffer gas atoms provide a widely applicable, relatively fast and simple mechanism for dissipating the ion energy (Savard *et al.*, 1991). Since the WITCH set-up is intended to be used to a wide range of (possibly) short-lived isotopes the buffer gas cooling technique will be applied.

In the buffer gas cooling technique the energy dissipation occurs via collisions between the buffer gas atoms and the ions. This interaction can be described to a good approximation as an average damping force

$$\mathbf{F} = -\delta M \mathbf{v}, \tag{6.10}$$

where M and $\mathbf{v}$ are the mass and velocity of the ion. The damping coefficient δ is given by

$$\delta = \frac{q}{M} \frac{1}{K_{mob}} \frac{p/p_N}{T/T_N}, \tag{6.11}$$

where the buffer gas pressure p is expressed in fractions of the normal pressure p_N, the temperature T in fractions of the normal temperature T_N and K_{mob} represents the ion mobility in the buffer gas. A compilation of nearly all available data on ion mobilities can be found in Ellis *et al.* (1978, 1976, 1984); Viehland and Mason (1995).

For the axial and the reduced cyclotron motion this mechanism will lead to a decrease of the amplitude of the motion and the ions will end up centered. In the case of the magnetron motion, however, the energy loss will lead to a widening of the motion. The time evolution of the radii of the two radial motions (reduced cyclotron and magnetron motion) is given by

$$r_{\pm}(t) = r_{\pm}(0)\exp(\alpha_{\pm}t) \tag{6.12}$$

with

$$\alpha_{\pm} = \mp\delta\frac{\omega_{\pm}}{\omega_{+} - \omega_{-}}. \tag{6.13}$$

Since $\omega_{+} >> \omega_{-}$ the cyclotron motion shrinks much faster than the increase of the magnetron radius as can be seen from equation 6.13. The evolution of the radial motion due to the presence of buffer gas atoms is shown in figure 6.6 (a).

As discussed in the previous section a quadrupole RF field that is applied on the four ring electrode segments with frequency ω_c will result in a conversion from one motion into the other. In combination with the damping force of the buffer gas this results into a decrease of the radial energy centering of the ions. Figure 6.6 (b) shows the effect of applying an RF quadrupole electric field at the true cyclotron frequency $\omega_c = \omega_{+} + \omega_{-}$. Typical buffer gas pressures that are used for cooling in a Penning trap are in the range of $10^{-2} - 10^{-5}$ mbar. Typical cooling times for those pressures are of the order of 10 to 20 ms. The buffer gas cooling has first been demonstrated at the ISOLTRAP set-up at ISOLDE/CERN (Savard *et al.*, 1991) and has in the mean time been implemented into different Penning trap set-ups. Mass resolving powers of 10^5 have been achieved (Raimbault-Hartmann *et al.*, 1997) allowing isobaric purification of the ion cloud.

One should however note that the buffer gas cooling technique is based on a single particle description of the trap dynamics where one relies on the fact that the motions in the quadrupole trapping potential can be coupled with a pure cyclotron excitation. However, increasing the number of ions in the ion cloud will deform the potential which an individual ion experiences in the Penning trap. So the buffer gas cooling method meets its limits both in efficiency as well as in mass resolving power at large ion numbers. However at the REXTRAP set-up it was shown that to 10^6 ions can be cooled with the buffer gas technique. Therefore this technique should also fulfill the needs of the WITCH set-up. If in future the number of trapped ions in WITCH would reach 10^7 it might be interesting though, to look for other techniques that are more effective for high density ion clouds. One of those techniques is the rotating wall cooling that

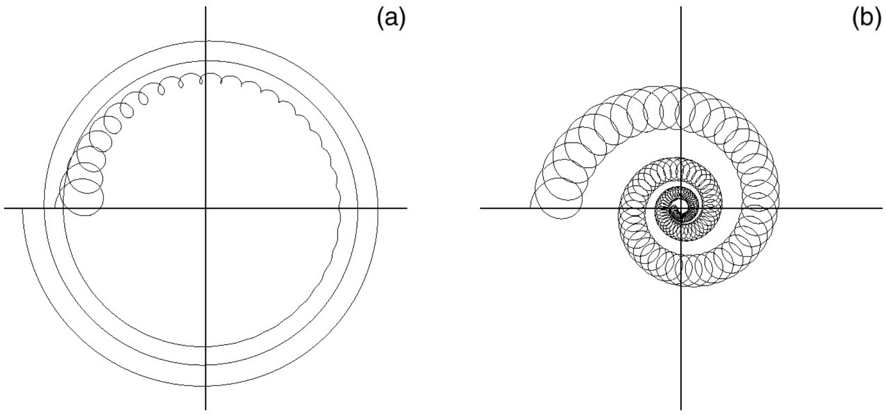

Figure 6.6: Radial trajectory of an ion in a buffer gas filled Penning trap without (a) and with (b) an RF quadrupole electric field at frequency $\omega_c = \omega_+ + \omega_-$ for the same starting position.

has recently been applied for the first time in combination with buffer gas at the REXTRAP-set-up (Reisinger, 2002).

6.1.4 Charge exchange

Although the motion of an ion in a Penning trap is meta-stable, in the absence of an energy removing mechanism the ion can stay confined for long times. However, due to charge exchange with rest gas particles, the ion can get neutralized and is lost. No estimates have been made so far on the charge exchange process. It should be clear, however, that the effect will be more pronounced for elements having a large ionization potential like the noble gases and is much smaller in the case of alkalis.

At the ISOLTRAP mass spectrometer, charge exchange losses for noble gas ions have been observed in the RFQ buncher and the cooler Penning trap, where a buffer gas is used to cool the ion motion (Blaum, 2003). For ^{36}Ar a half-live of the order of 5-10 ms has been observed in the RFQ buncher. In the hyperbolic Penning trap, where a pressure of 10^{-8} – 10^{-9} mbar is maintained, the loss is negligible. For the stable K^+ions that are being produced at the off line ion source, charge exchange is negligible through out the complete set-up (Blaum, 2003).

6.2 Many ions in a Penning trap

The previous section has focussed on the behavior of a single ion in the quadratic electrostatic potential and the homogenous magnetic field of a Penning trap. As more ions are inserted into the trap the electric repulsion between the ions will start to play a role. The influence of the Coulomb interaction on the dynamics of the trapped particles will be more pronounced for an increasing number of trapped ions. Since the WITCH set-up aims to store of the order of 10^6 ions in a Penning trap the influence of the created space charge on the recoil energy measurement has to be investigated.

As soon as one inserts a few to a couple of thousand ions at rather low densities in a Penning trap the effect of the Coulomb repulsion can be observed as deviations from the expected excitation resonance at the single particle frequencies. Two experimental examples will be discussed to show this behavior. This will be followed by a brute force simulation approach to study these many ions effects. This simulation can still be considered as a single particle description of the problem although a trick is needed to access the regime of 10^7 ions in the trap.

Increasing the ion density, the ion cloud can at some moment be described as a non-neutral plasma. An important feature of this approach is that the focus is on the collective phenomena of the ion cloud rather than looking on the scale of single particles. Although the densities that can be reached with the REXTRAP and probably also with the WITCH set-up, do not allow completely to consider the ion cloud as a non-neutral plasma, as will be shown later, the REXTRAP set-up operates under certain circumstances in the vicinity of the collective regime. Therefore the non-neutral plasma field can give hints for unexplained effects that are observed in the WITCH and REXTRAP density regime.

6.2.1 Experimental observations of space charge effects

In recent work (Paasche *et al.*, 2002), a study has been made on the effect of the space charge created by electrons in a Penning trap. A study of the $2\nu_z$ resonance in the motional spectrum reveals an individual and a center-of-mass resonance, as shown in figure 6.7. The broad non-collective resonance is linked to the individual motions of the ions inside a Penning trap and shifts to lower values for increasing number of trapped electrons. The narrow collective resonance stays at the one-particle frequency value and is linked by the authors to the center of mass motion of the ion cloud. A similar appearance of these two resonances has been observed in a Paul trap (Alheit *et al.*, 1997). The fact that individual ion frequencies shift from their values corresponding to the absence of the Coulomb repulsion, indicates that the total electric potential that the electrons experience in the Penning trap, deviates from the pure quadratic potential. Paasche *et al.* (2002) made an attempt to explain the asymmetric shape of the non-collective resonance in the Penning trap by including higher order terms of the electric potential. Including an r^4 contribution (with coefficient $c_4 = 10^{-3}$) to the quadratic potential provides good agreement with the experimental resonance as can be seen from figure 6.7.

Frequency shifts due to the space charge of a large number of ions inside a Penning trap have also been observed in the REXTRAP-set-up. When performing buffer gas cooling, the resonance frequency ω_q was found to shift to higher values and also broadened when the amount of trapped ^{133}Cs ions increased from 10^4 to 10^7 (Ames *et al.*, 2001; Forstner, 2001). For the case of ^{133}Cs this behavior is shown in figure 6.8. A shift of the center of the resonance of the order of 7.5 kHz can be observed and a broadening by a factor of about seven. By performing a second excitation after the first cooling stage a shift of the resonance frequency between those excitations occurred again. The resonance frequency for the second excitation was again shifted to higher to higher values. This measurement shows that the effect depends on the ion density rather than on the ion number. Shifts of the order of a few hundred Hz have also been observed at the dipole excitation of the magnetron motion and the reduced cyclotron motion. In both cases the resonance frequency increases with increasing ion number (Forstner, 2001).

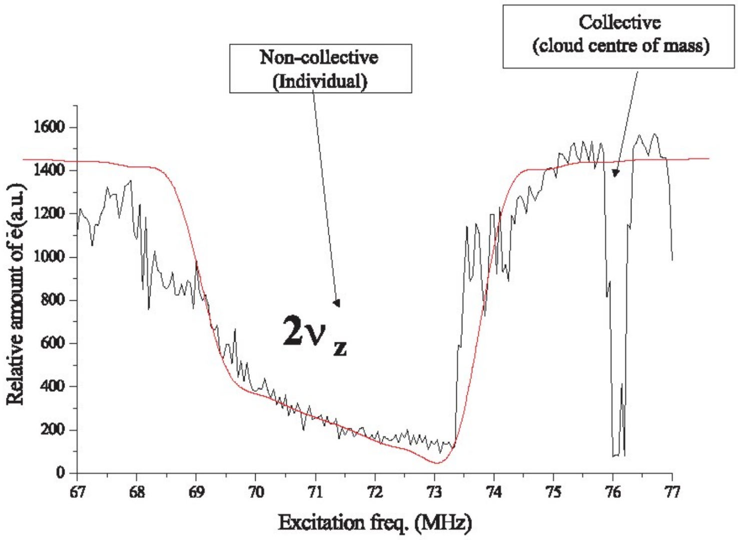

Figure 6.7: Individual and center-of-mass component observed in the $2\nu_z$ resonance of electrons in a Penning trap (Paasche *et al.*, 2002). The line represents a calculation of the non-collective resonance in which a term of order r^4 has been introduced.

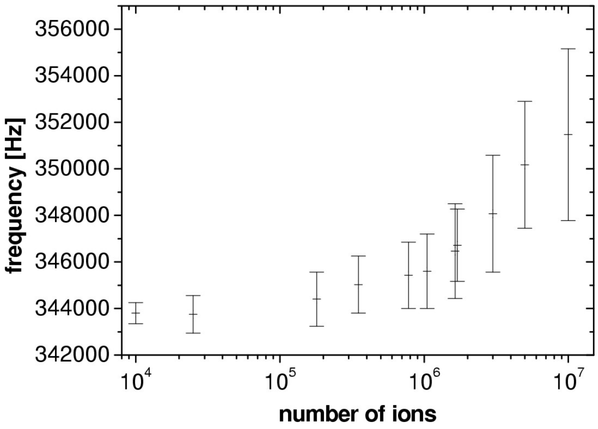

Figure 6.8: Shift and broadening of the cooling resonance frequency ω_q observed at the REXTRAP-set-up (Ames *et al.*, 2001).

6.2.2 Scaled Coulomb force simulations

In order to describe the behavior of the cooling resonance at REXTRAP for high ion densities numerical simulations have been performed (Beck *et al.*, 2001). Since it is not possible with the present computing power to calculate on a reasonable time scale the trajectories of ion numbers of the order of 10^6 ions taking into account the Coulomb repulsion between the individual ions, an alternative approach was followed. The calculation was performed with about 10^3 ions but the Coulomb interaction between the particles was scaled as

$$F_{C,comp} = \frac{N_{store}}{N_{comp}} F_C. \tag{6.14}$$

In this expression $F_{C,comp}$ is the scaled Coulomb force used in the calculation, F_C represents the true Coulomb force between two ions, N_{store} is the number of stored ions and N_{comp} the number of particles used in the calculation. For the computation a fifth-order Runge-Kutta method with adaptive step size control was adapted from Press and coworkers (1996).

The trap parameters used for those calculations are: U_0 = 100 V, d = 41.6 mm, magnetic field B = 3.0 T, mass of the singly charged ions m = 133 amu, buffer gas pressure $p = 10^{-3}$ mbar. The mobility constant $K_{mob} = 2$ cm^2/(Vs) is that for cesium ions in argon gas.

Simulations of the buffer gas cooling process for different ion numbers in the trap show that the resonance frequency shifts to higher values as shown in figure 6.9 for two initial starting conditions. The shift is larger for high initial density and is of the same order of magnitude as the experimental result observed at REXTRAP. The broadening of the resonance, obtained from the simulations, is by far not as pronounced as was observed in the experiment.

A simulation of radial dipole excitations at the magnetron frequency ω_- and at the reduced cyclotron frequency ω_+ show that in these cases, a shift is observed of approximately 30 Hz to lower, respectively higher values. If the effect of the space charge would be described as a reduction of the effective trap potential, then the direction of the shifts can be explained from equation 6.4 by a reduction of the value of ω_z through U_0. The validity of this simple picture is however doubtful since the repulsive force would act in opposite direction as the axial trapping field but would enforce the radial outward pointing electric

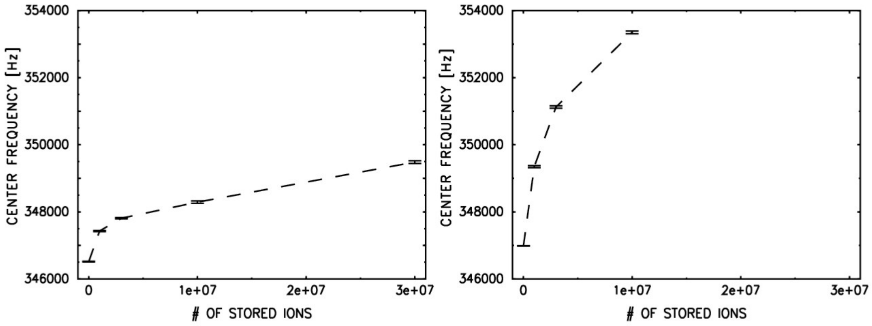

Figure 6.9: Shift of cooling resonances as a function of ion number based on simulations with a scaled Coulomb force (Beck *et al.*, 2001). The initial distribution in radial and axial direction is 15 mm (left) and 5 mm (right)

field of the trap. Furthermore, the direction of the magnetron frequency shift as well as the order of magnitude of both shifts are not in agreement with the experimental results. An important conclusion that can be drawn from these simulations is that the cooling resonance shifts are, not to first order, coming from trap imperfections since a perfect quadratic potential was used in the simulations.

With the same approach an estimate has been made of the dimensions of the ion cloud in the REXTRAP set-up. Figure 6.10 shows the ion cloud size in radial and axial direction after buffer gas cooling for 20 ms. Two different initial distributions have been used. For an ion cloud of 10^7 ions the radial $FWHM_r$ is roughly 5 mm, taking the mean of the two results corresponding to two different initial distributions. In axial direction the $FWHM_z$ is of the order of 11 mm. From these values an order of magnitude estimate of the ion cloud density can be made by assuming that the ions are located inside an ellipsoid with the width in radial direction given by FWHM_r and in axial direction by FWHM_z. This corresponds to a volume of 0.15 cm^3 implying that the density will be of the order of a few 10^7 ions/cm^3.

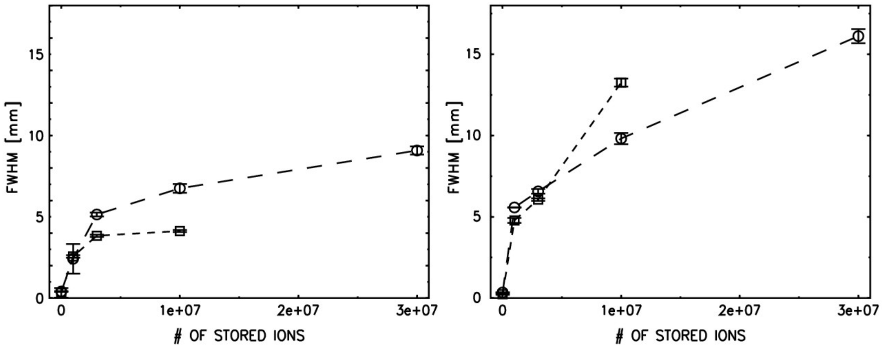

Figure 6.10: Calculated size of the ion cloud after buffer gas cooling during a period of 20 ms. On the left (right) side the FWHM in radial (axial) direction is shown as a function of ion number for two different initial distributions (circles: FWHM=15 mm, squares: FWHM=5mm) (Beck *et al.*, 2001).

6.2.3 Non-neutral plasma regime

In certain temperature and density regimes a collection of a large number of ions in a Penning trap can be characterized as a so-called non-neutral plasma. The condition for this, as generally stated, is that the ion cloud dimensions of such a plasma should be large compared to the Debye length λ_D (Dubin and O'Neil, 1999) which is given by

$$\lambda_D = \sqrt{\frac{\epsilon_0 k_B T}{2ne^2}}, \tag{6.15}$$

and where T represents the plasma temperature and n the charge density of the ion cloud. This condition ensures that external electric fields are Debye screened over a distance of the order of λ_D by the ions at the edge of the cloud. The two parameters T and n thus determine whether an ion cloud is in the non-neutral plasma-regime or not. For an ion cloud with a density of $n = 10^7$ ions/cm^3 and $T = 300$K the Debye length equals $\lambda_D = 1.2$ mm. The plasma frequency of this collection of charges is given by (Dubin and O'Neil, 1999)

$$\omega_p = \sqrt{\frac{e^2 n}{\epsilon_0 m}}. \tag{6.16}$$

The description given below will concentrate on ion clouds where correlations between the ions are weak ($\Gamma << 1$ (Dubin and O'Neil, 1999)) which is valid when dealing with ion clouds with "low" densities, i.e. of the order of 10^7 ions per cm^3 at room temperature.

With sufficiently long confinement the ions evolve to a state of thermal equilibrium characterized by a uniform density that drops to zero at the distance scale of one Debye length. This evolution has been observed experimentally in the case of electrons (Driscoll *et al.*, 1988). With decreasing temperature this border gets sharper resulting into a step function when $T = 0$.

A cloud in thermal equilibrium performs a rigid rotation around the magnetic field axis with a frequency that is independent of the radius and given by (Dubin and O'Neil, 1999)

$$\omega_r = \frac{1}{2}\left(\omega_c \pm \sqrt{\omega_c^2 - 2\omega_p^2}\right), \tag{6.17}$$

which depends on the ion cloud density via the presence of ω_p (Dubin and O'Neil, 1999). As is shown in equation 6.17 for a certain density n two solutions are present. When the ion density equals the Brillouin density (Brioullin, 1945) given by

$$n_B = \frac{\epsilon_0 B^2}{2M}, \tag{6.18}$$

with B the magnetic field of the Penning trap and M the mass of the confined ion, the two frequencies become equal

$$\omega_r = \frac{1}{2}\omega_c. \tag{6.19}$$

The energies of the confined ions are Boltzmann distributed inside a frame rotating with the ion cloud (Dubin and O'Neil, 1999).

Estimate of ion cloud dimension

For a non-neutral plasma in a Penning trap with a quadrupole potential the space charge potential of an ion cloud in thermal equilibrium can be calculated (Bollinger *et al.*, 1993; Dubin and O'Neil, 1999). In this case the ion cloud is a spheroid characterized by the so-called aspect ratio $\alpha = r_s/z_s$ that depends on the radial width $2r_s$ and the axial extent $2z_s$ of the spheroid. As discussed by Bollinger *et al.* (1993) the space charge potential is given by

$$U_{sc} = -\frac{m\omega_p^2}{6e}\left[a(\alpha)r^2 + b(\alpha)z^2\right] \tag{6.20}$$

The coefficients $a(\alpha)$ and $b(\alpha)$ can be calculated from

$$b(\alpha) = 3\frac{Q_1^0(\frac{\alpha}{\sqrt{\alpha^2-1}})}{\alpha^2 - 1} \tag{6.21}$$

and

$$2a(\alpha) + b(\alpha) = 3 \tag{6.22}$$

with Q_1^0 the associated Legendre polynomial of the second kind (Morse and Feshbach, 1963). Since $b(\alpha)$ depends on the axial and the plasma frequencies via

$$b(\alpha) = 3\frac{\omega_z^2}{\omega_p^2} \tag{6.23}$$

The aspect ratio α for an ion cloud with given density n, can be calculated by combining equations 6.21 and 6.23. If the cloud contains N ions then the radial and axial dimensions of the cloud can be calculated from the aspect ratio and the volume of the spheroid, which is given by

$$V = \frac{4\pi r_s^2 z_s}{3} \tag{6.24}$$

Table 6.2 lists some calculated dimensions of ion clouds in thermal equilibrium at T =300 K, for various densities and numbers of trapped ions for both the REXTRAP set-up as well as the WITCH Penning trap. Looking to the radial dimensions of the ion cloud one can see that they are relatively large for the two lowest densities. An interesting point to note is also that the ion cloud aspect ratio α depends on the potential well depth of the Penning trap but not on the magnetic field strength of the Penning trap. The dependence of the aspect ratio on the trap depth D can be observed by noting that it is smaller in the case of REXTRAP, having a deeper potential well. The magnetic field does not affect the aspect ratio (as long as it is strong enough to allow confinement) since it does not compress the cloud but rather prevents it from expanding into the radial direction. A comparison between the simulated ion cloud dimensions show that the order of magnitude is the same as for the calculated values. Due to the difference in distribution function (assumed to be gaussian in the

Table 6.2: Estimate of ^{35}Ar^{+} ion cloud dimensions in the non-neutral plasma regime for both WITCH and REXTRAP.

		WITCH			REXTRAP		
n	N	α	r_0	z_0	α	r_0	z_0
ions/cm^3	ions		[mm]	[mm]		[mm]	[mm]
$6 \cdot 10^6$	10^7	2.07	5.7	11.9	1.04	7.3	7.6
	10^6	2.07	2.6	5.54	1.04	3.4	3.5
10^7	10^7	3.19	4.2	13.4	1.81	5.1	9.1
	10^6	3.19	2.0	6.3	1.81	2.4	4.3
$6 \cdot 10^7$	10^7	11.3	1.5	17.2	7.35	1.8	12.9
	10^6	11.3	0.7	8.0	7.35	0.8	6.0

simulation results and uniform in the non-neutral plasma description), it is however hard to make more quantitative comparisons. A second important point one should mention is that decreasing the temperature will not change the dimensions of the spheroid significantly. As discussed before it will just make the border of the spheroid sharper.

6.2.4 Importance for the WITCH set-up

It is expected that space charge effects are of importance for the WITCH experiment because of three reasons. First of all the buffer gas cooling, being a single particle technique, works less efficient for large number of ions, since the electrostatic potential, that the ions experience, deviates from the quadratic one. In the case of REXTRAP it has been observed that the efficiency of the buffergas cooling decreases significantly when the number of stored particles exceeds 10^6 (Ames *et al.*, 2001). Since the WITCH setup will also make use of the buffergas cooling, it will have to be investigated for which trap load the cooling fails to compress the ion cloud strong enough, to allow transfer through the differential pumping diaphragm.

Secondly the response of the spectrometer will depend on the radial position at which the recoil ion has started its orbit. Therefore the radial dimension of the ion cloud induces a systematic effect. A good knowledge of the dimensions and charge distribution of the ion cloud is of importance. A rough estimate from the brute force simulations and the non-neutral plasma calculations, predict a radial extent of 1 to a few mm for 10^6 ions in the WITCH trap. Concerning the ion distribution inside the cloud no estimates have been made up to now.

Finally, it might be that energy distribution of the ions in the trap deviates from the single particle picture due to the Coulomb repulsion. This topic has not been investigated in detail in this work. However, in future a study of this effect has to be made. This is of high importance because the major deformation to the response function of the spectrometer finds its origin in the Doppler broadening due to the initial energy of the ions in the trap, as will be shown in chapter 7.

6.3 WITCH double Penning trap system

6.3.1 Electrode structure

The Penning trap electrodes are incorporated into a larger structure, shown in figure 6.11, that consists out of three sections. The first part is a drift and retardation section located just above the vertical beamline, through which the bunched beam passes and gets further decelerated from an energy of 1.5 keV down to roughly 50 eV. The second section is the cooler trap in which the ion bunch is captured. The decay trap is the third component.

Each section forms a separate unit consisting out of cylindrical electrodes with an internal diameter of 40 mm and machined out of oxygen free high purity copper. The electric insulation between the electrodes is performed by rings out of the glass ceramic Macor. In order to avoid the formation of insulating oxides on the electrode surface, all electrodes have been gold plated. Each of the three sections is kept together by two disks that are fixed to each other by means of four rods. This surrounding structure is made from aluminium. The total length of the structure is 670.5 mm.

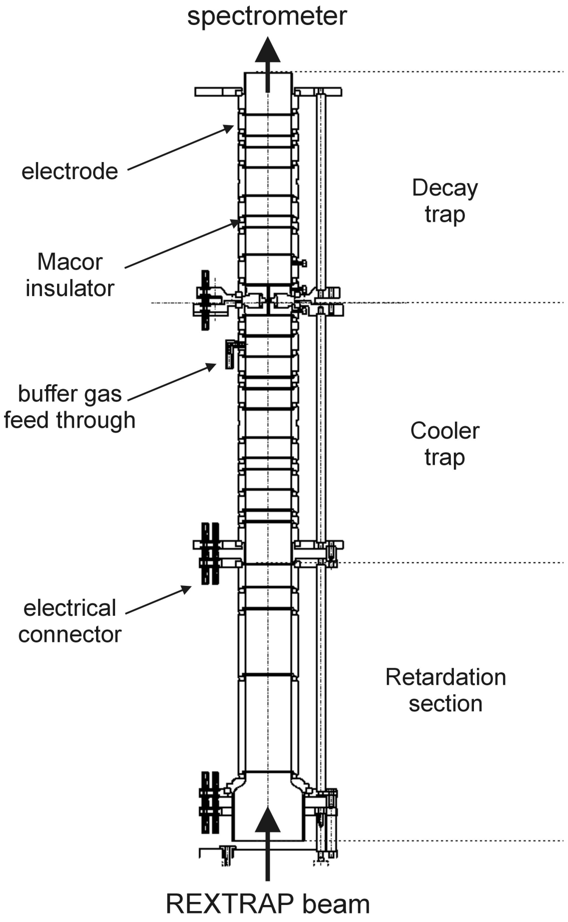

Figure 6.11: Electrode structure of the WITCH double Penning trap structure consisting of three components: retardation section, cooler trap and decay trap.

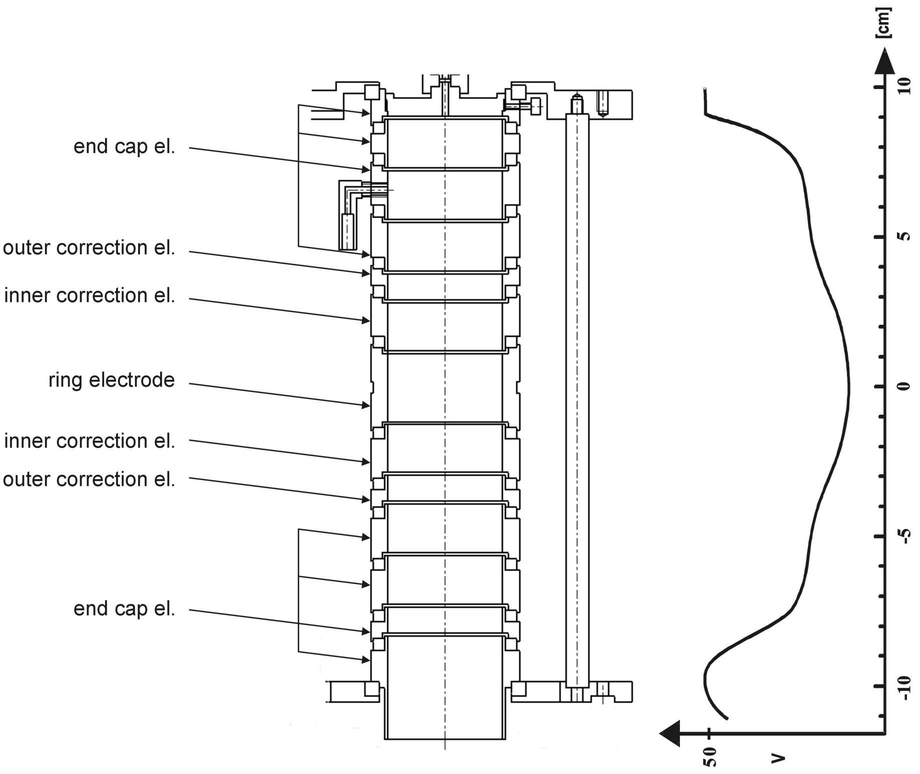

Figure 6.12: Electrode structure of the WITCH cooler trap (a) and the electric potential (b).

6.3.2 Penning trap design

Both Penning traps of the WITCH set-up are of the cylindrical type. This has the advantage that the electrode structure is much more open allowing easy injection and extraction and providing a better pumping cross section. The design of both Penning traps is based on the ISOLTRAP cooler trap (Raimbault-Hartmann *et al.*, 1997). Figure 6.12 shows the electrode structure of the cooler trap as well as the electric potential that is generated by this configuration.

Two correction electrodes positioned at both sides of the ring electrode allow to fine tune the trapping potential in order to let it match the quadrupole shape.

Both upper and lower end cap electrodes consist out of four segments. This configuration allows to apply a big boxlike potential for injection purposes as shown in figure 6.12 (b). Furthermore, an electric field gradient can be created to eject the ions out of the Penning trap. The ring and the inner electrode are cut along the axis into eight and four respectively equal parts to allow the application of RF fields for excitation purposes. Apart from a shortened end cap electrode the decay trap is a copy of the cooler trap. A picture of the electrode structure of the two traps is shown in 6.13.

In order to perform the commissioning of the two Penning traps an electrode structure with MCP detector is fixed above the decay trap as shown in figure 6.14. With this structure it is possible to accelerate the ejected beam before detection with the MCP. In this way the injection, cooling and transfer process can be optimized.

6.3.3 Buffer gas system

In the cooler trap buffer gas atoms at a pressure of typically $10^{-3} - 10^{-5}$ mbar are used to dissipate the energy of the trapped ions. As one does not want this buffer gas to interfere with the β-decay of ions in the decay trap, the volumes of both traps should be connected via a long and thin channel. If both volumes are pumped this will result into a significant pressure drop between the two traps through the so-called differential pumping diaphragm. The small diameter can, however, result into ion loss if the ion cloud diameter exceeds the opening of the channel. Therefore an optimal balance should be found between pressure drop and minimal ion loss during the transfer of the ion cloud. For this reason it was decided to produce different pieces that allow to form a gas channel that can have a diameter of 2, 3 or 4 mm and a length of 25 or 52 mm depending on the electrodes that are inserted. Gas flow calculations taking into account the pumping capacity of the set-up have been performed and show that a pressure ratio of one hundred to several hundreds can be achieved. Assuming that the transfer of the cloud from one trap to the other happens in a translational way, the loss of the ions due to the blocking is shown in figure 6.15 for ion clouds with different radial dimensions. Note that in this approach the cyclotron radius is not taken into account.

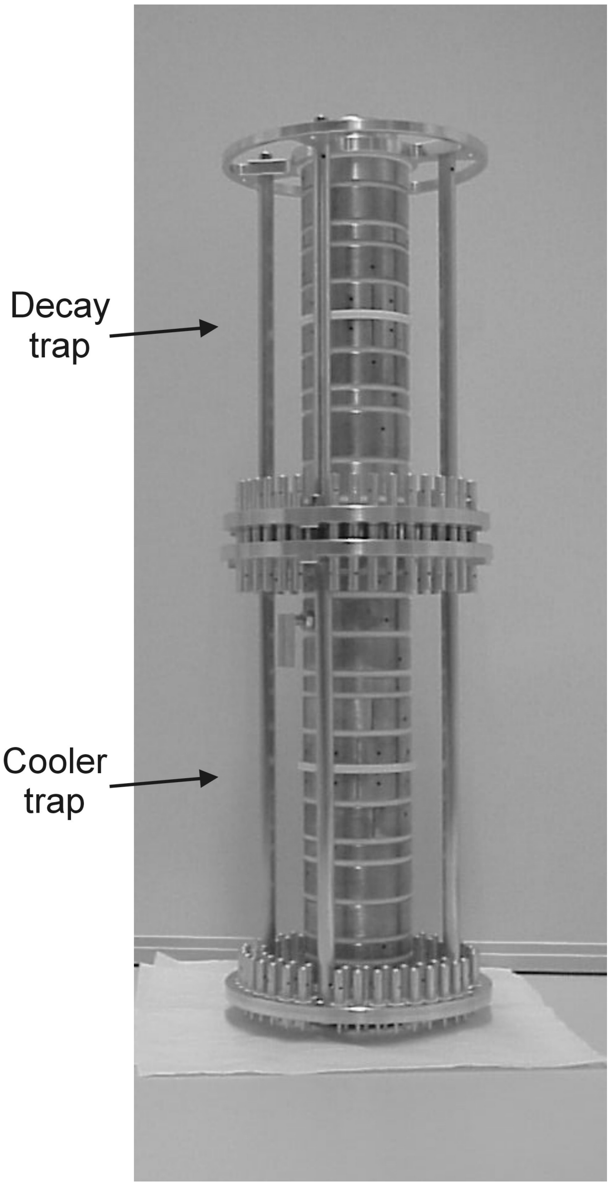

Figure 6.13: Picture of the cooler and decay trap.

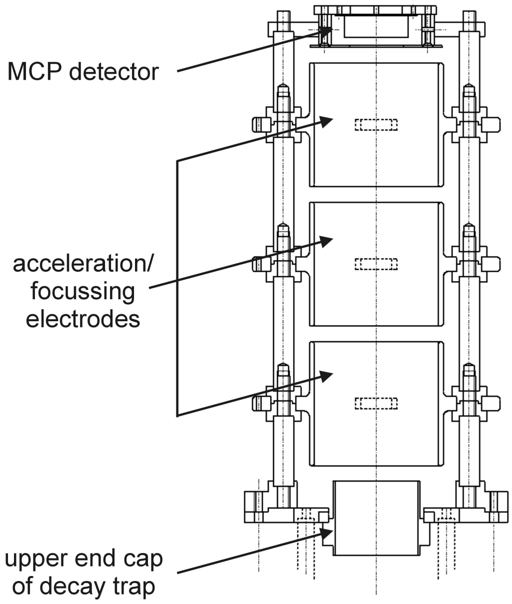

Figure 6.14: Electrode structure mounted on top of the Penning trap structure to focuss and accelerate ejected ions towards an MCP detector for testing and optimizing the ion trapping.

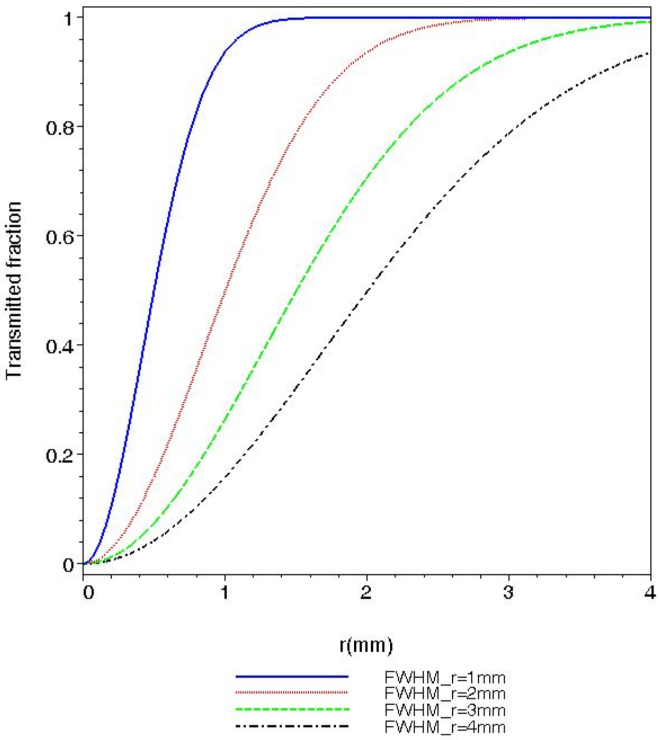

Figure 6.15: Fraction of ions that is blocked by the differential pumping diaphragm as a function of the diaphragm radius. The different curves represent different radial ion cloud dimensions.

A gas dosing valve located outside the vacuum chamber allows to control the gas flow that is sent to the cooler trap. Inside the vacuum a teflon tube guides the buffer gas. The gas is inserted into the cooler trap via a metal piece that is connected to the second segment of the end cap, as can be seen in figure 6.11.

6.3.4 Superconducting magnet system

The magnet system of the WITCH set-up contains two superconducting coils sharing a common cryostat. A first coil generates the 9T field for the two Penning traps. The winding is done in such a way that two homogenous field regions are created 100 mm above and below the center of the 9T coil and coinciding with the positions of the two Penning trap ring electrodes. The homogeneity of the magnetic field is 10^{-4} over a region of length 40 mm and diameter 10 mm in both regions. The second coil can generate a maximal field of 0.2T which is used for the retardation spectrometer as will be discussed in chapter 7. In the center of this coil the homogeneity of the magnetic field is $5{\cdot}10^{-5}$ inside a sphere of 10mm diameter. The magnetic field on axis, generated by the two coils, is shown in figure 6.16. The center of the 9T magnet coil is located at $z = 0$.

The vacuum tube which is connected to the magnet system consists out of two parts having a different diameter. The Penning trap structure is located inside a tube with a diameter of 130mm and a length of 903 mm. The major part of the spectrometer is located inside a tube with a diameter of 420 mm and length of 1663 mm. The most important parameters of the magnet system can be found in table 6.3.

6.4 Injection of ions in a Penning trap

6.4.1 Injection

The process to inject ions into a Penning trap has been developped at the ISOLTRAP-experiment at the ISOLDE/CERN facility (Schnatz *et al.*, 1986). At present there are two procedures used to inject an ion beam into a Penning

Table 6.3: Important parameters for the WITCH superconducting magnet system (Superconductivity, 2002).

parameter	9T-coil	0.2T coil
manufacturer	Oxford Instruments	
LN volume (l)	163	
LN holding time (days)	3	
Useful LHe volume (l)	44	
LHe hold time (days)	7	
overall length (mm)	2566	
B(T)	9	0.2
coil current (A)	103.81	67.87
bore tube diameter (mm)	130	420
homogeneity	10^{-4}	$5 \cdot 10^{-5}$

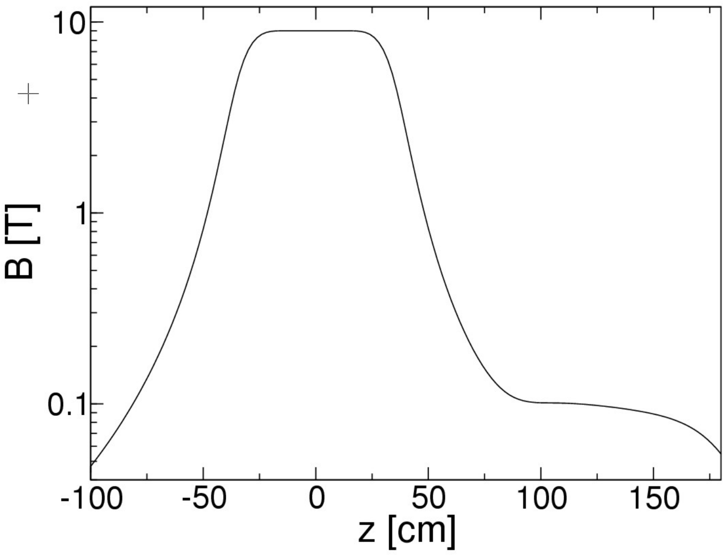

Figure 6.16: Magnetic field on the axis.

trap (Raimbault-Hartmann *et al.*, 1997): the pulsed and the continuous injection. Figure 6.17 schematically shows both procedures. The first approach is best suited for a bunched beam. The first end cap electrode is at low voltage such that the ion bunch can enter the trap. As soon as the ion bunch is inside, the potential of the end cap is raised such that the ions cannot escape any more. Due to collisions with buffer gas atoms the ions loose energy and are guided finally into the harmonic part of the trap potential.

The time it takes the ions to be reflected at the right potential barrier in figure 6.17 and reach the left electrostatic wall that has been raised after the complete ion cloud has entered the cooler trap, depends on the axial energy of the ions. Assuming the distance between the two electrostatic end cap walls to be 15 cm, this travel time for $^{35}\mathrm{Ar}^{+}$ ions is shown in figure 6.18 for different axial kinetic energies. It ranges from about 13 μs to 40 μs for ion kinetic energies between 100 eV and 10 eV respectively. No energy loss has been taken into account here. If the first end cap electrode can be pulsed up in a time interval less than 1 μs then an axial energy spread of 100 eV can still be tolerated assuming the time spread of the REXTRAP bunch is 10 μs. It is this 100 eV energy spread that has been used to estimate the pulsed drift section timing that was discussed in chapter 5.

The second approach allows to inject a DC ion beam into the trap. In this scheme the potential on the first end cap electrode is such that the incoming beam can pass over it, but that after reflection on the second end cap the ions have lost so much energy that they cannot escape any more over the potential well of the trap. In the same way as with the pulsed injection, the ions are centered in the harmonic part of the trap. This technique is used to inject the ISOLDE DC-beam into the REXTRAP Penning trap.

6.4.2 Transferring ions between two traps

The transfer of the ion cloud between the cooler trap and the decay trap will be performed by lowering the potentials on the electrodes in between the two traps and creating in this way an accelerating electric field gradient. This allows to transfer the ion cloud to the second trap. The process is sketched in figure 6.19. A study of the effect of the ejection and injection electric field gradient on the

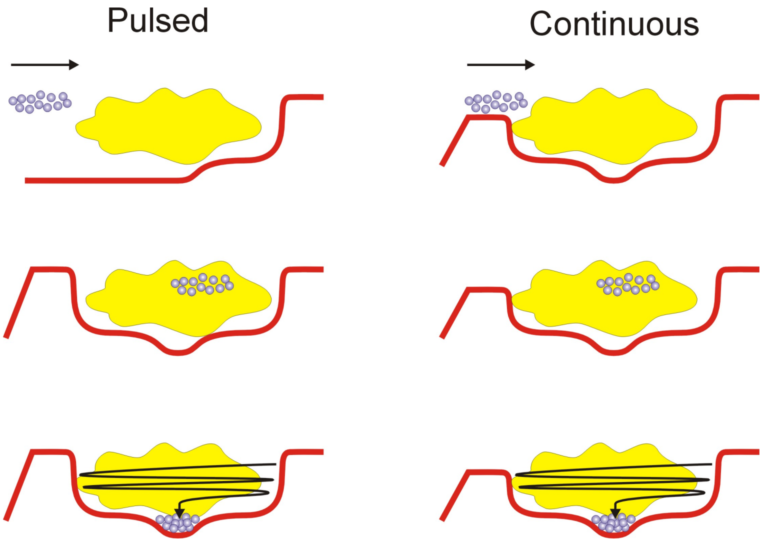

Figure 6.17: Schematic view on pulsed (left) and continuous (right) injection of ions in a cylindrical Penning trap.

axial spread of the ions after transfer of an ion cloud between the cooler trap and the measurement trap is discussed by Beck (1997).

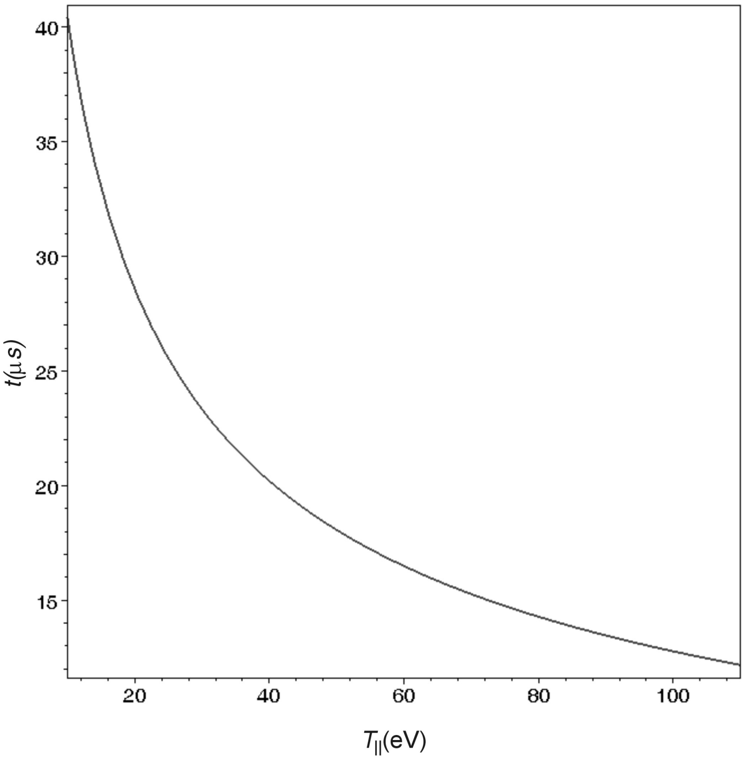

Figure 6.18: Travel time inside the cooler trap between entering the trap and returning at the same position after reflection at the end cap potential, for different kinetic energies.

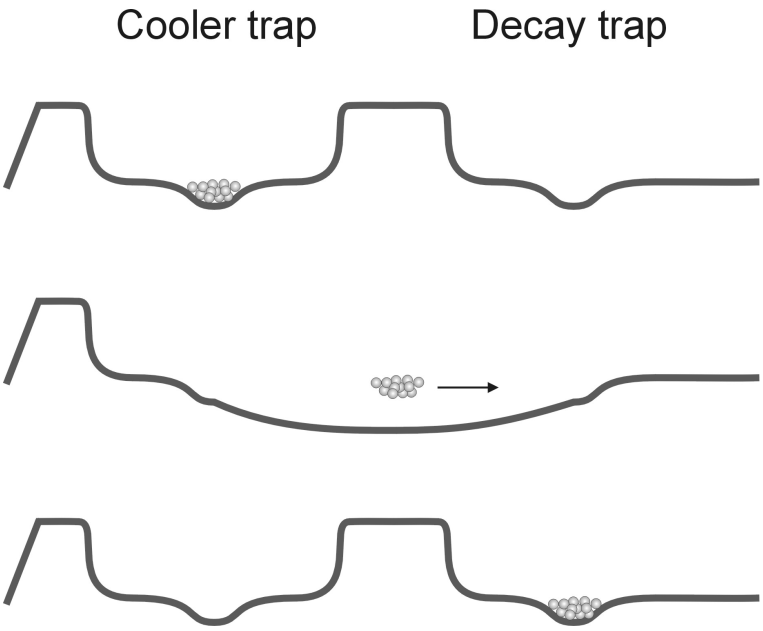

Figure 6.19: Schematic sketch on the transfer of the ion cloud from the cooler trap to the decay trap.

Chapter 7

WITCH retardation spectrometer

The analysis of the recoil energy that the daughter nuclei have gained in nuclear beta decay in the second Penning trap, is performed in the retardation spectrometer, which acts as an electrostatic filter. First of all the principle of energy conversion in a smoothly changing magnetic field is discussed, which provides the spectrometer to accept emission in a solid angle of 2π, that is combined with high energy resolution. Inside the ideal picture the response function of a mono-energetic collection of isotropically emitted ions is derived. In a following section the realization of the spectrometer principle for the WITCH set-up is discussed. The specific features of this device are used to investigate the true response function of the set-up and give an overview of the different systematic effects influencing the performance of the spectrometer. The chapter will be concluded by giving a glimpse on the spectral shape that is expected to be measured with the WITCH set-up.

7.1 Principle of retardation spectrometer

The energy conversion of radial into axial kinetic energy in a smooth magnetic field gradient is already known for quite some time. Combining it with an electrostatic filter in order to reach high resolution at full solid angle was first done in 1980 by Beamson *et al.* for low-energy electron spectroscopy. The most famous applications of this experimental approach, that has been realized to date, are the measurements of the spectral shape of the endpoint region of the β-spectrum of tritium decay in Mainz (Picard *et al.*, 1992) and Troitsk (Lobashev and Spivak, 1985). This has allowed to put an upper limit on the mass of $\bar{\nu}_e$ of $m_{\bar{\nu}_e} \leq 2.5\mathrm{eV}/c^2$ (95%CL) for the Troitsk spectrometer (Lobashev *et al.*, 1999) and $m_{\bar{\nu}_e} \leq 2.3\mathrm{eV}/c^2$ (95%CL) for the Mainz experiment (Kraus *et al.*, 2004). The same principle will be exploited in the KATRIN spectrometer that is being prepared now and will be installed at the Forschungszentrum Karlsruhe with the aim of improving the $\bar{\nu}_e$-mass sensitivity to about 0.35 eV/c^2 (Osipowicz and coworkers, 2001). In the field of $\beta - \nu$-angular correlation measurements the aSPECT spectrometer uses the same concept to measure the recoil energy spectrum of protons that originate from free neutron decay (Zimmer *et al.*, 2000).

7.1.1 Principle of energy conversion

In a magnetic field that changes slowly over the distance that a charged particle travels during one cyclotron orbit (referred to as an adiabatic change) one can show that the action integral for the transverse motion

$$J = \oint \mathbf{p}_\perp \cdot d\mathbf{l} \tag{7.1}$$

is an invariant (Jackson, 1975). The symbol $\perp$ refers to the plane perpendicular to the magnetic field $\mathbf{B}$. Working out the action integral, the adiabatic invariance of J means that the flux linked by the particles orbit remains constant. This statement can be rewritten in three different ways, i.e.

$$\left.\begin{array}{c} Br_c^2 \\ p_\perp^2/B \\ \gamma\mu \end{array}\right\} \text{are adiabatic invariants} \tag{7.2}$$

where r_c is the cyclotron radius and μ the magnetic moment of the particle.

Applying this invariance to a situation where two homogenous magnetic field regions with field strength B_1 and B_2 are connected via a smooth magnetic field gradient such that the motion of a charged particle is adiabatic, then the second invariance statement can be easily rewritten as

$$\frac{T_{\perp 1}}{T_{\perp 2}} = \frac{B_1}{B_2}, \tag{7.3}$$

with $T_\perp$ the kinetic energy of the particle in the plane perpendicular to the magnetic field, and the index $_i$ referring to the homogenous field region B_i. This index convention will be followed through out the remainder of the chapter. Since the total kinetic energy is constant in a magnetic field environment, expression 7.3 shows that if $B_1 > B_2$ radial kinetic energy of the particle motion in the high magnetic field region is converted into axial energy during the transition to the low field region. If the initial velocity of the charged particle forms an angle θ with respect to the magnetic field axis, the axial kinetic energy in the low field region is given by

$$T_{\|2} = T_1 \left[1 - \frac{B_2}{B_1} \sin^2 \theta \right], \tag{7.4}$$

with T_1 the total initial kinetic energy and $T_{\|}2$ the kinetic energy in the motion along the magnetic field.

In the case of the WITCH set-up, the decay trap is located in a homogenous 9 T field. In the low magnetic field region of the spectrometer the field strength is 0.1 T. In this case a conversion of almost 99% of the radial kinetic energy into axial energy is realized under adiabatic conditions, as can be calculated from equation 7.3 by setting $\theta = 90°$.

The inverse process of conversion of axial into radial energy, that occurs when going from a low to a high magnetic field region, is the fact that makes injection of ions into a Penning trap a non-trivial process as was discussed in chapter 5. If all axial energy is converted into radial energy before the ion has reached the highest point of the electrostatic hill on which the Penning trap is situated, the ion will be reflected. This is called the magnetic mirror effect. This can be avoided by minimizing the angle that the ion velocity makes with the magnetic field, as can be seen from equation 7.3 while setting $B_1 < B_2$.

An important question that concerns the energy conversion in the magnetic field gradient is the validity of the adiabatic approximation. As mentioned above, Jackson (1975) states that the magnetic field change should be small over one cyclotron orbit. This idea is transformed by Kruit and Read (1983) into an adiabaticity parameter given by

$$\chi = \left| \frac{\Delta B_z}{B_z} \right| = \frac{2\pi m v_{\|}}{e B_z^2} \left| \frac{dB_z}{dz} \right| \tag{7.5}$$

and representing the fractional change of the magnetic field over one pitch of the trajectory. As long as $\chi_{max} < 1$ the beam passing through the magnetic field gradient in the application of (Kruit and Read, 1983) has the same diameter as well as intensity distribution as in the adiabatic case. Since it has to be investigated by ion trajectory simulations whether one can talk about an adiabatic conversion, no further effort will be spent to define a good adiabatic condition.

It is good to note, however, that the only particle related parameter in expression 7.5 is the momentum. Assume a collection of singly charged particles, being emitted isotropically inside the high magnetic field region B_1 with a momentum p If their trajectories can be considered as adiabatic then all other particles having a momentum smaller than p will perform an adiabatic energy conversion. This statement can be applied to the WITCH spectrometer and nuclear β-decay: if there is no adiabaticity violation for the trajectories of the recoil ions originating from a β-transition with Q-value Q_{ad}, then this will also be the case for recoil ions and β particles from a decay with $Q < Q_{ad}$.

7.1.2 Retardation potential

After the ions have arrived in the low magnetic field region, their recoil energy is almost completely converted into axial energy. By applying an axial electrostatic retarding field, a filter is created that only allows the most energetic ions to pass and reach a detector that is positioned behind this barrier. To assure that the energy conversion is adiabatic in the magnetic field gradient region it is however preferable that the retardation of the ions is performed as soon as they leave the high field region. As can be seen from the adiabaticity parameter defined in equation 7.5 its value will be high in the region close to the low field region due to the presence of the factor B_z^2 in the denominator. Therefore the retardation potential should increase as soon as the magnetic field decreases and reach a smooth maximum in the low magnetic field region. The plane perpendicular to the magnetic axis in the low magnetic field region at the position where the retardation potential reaches its maximum, is called the analysis plane. On the other hand it should be taken care of that a too fast increase of the electrostatic retardation potential, would not reflect the ions in the intermediate zone due to incomplete energy conversion, although they would have sufficient axial energy to cross the retardation barrier in the analysis plane. Furthermore the electrostatic potentials in the spectrometer region should be generated in such away that the retarding electric field is parallel to the magnetic field lines. In the design of the electrode structure of a retardation spectrometer all those considerations have to be taken into account.

7.1.3 Response of a mono-energetic peak

To be able to fit the measured recoil energy spectrum to the $\beta - \nu$ correlation coefficient a, it is important to know how the set-up itself affects the initial energy distribution of the recoil ions in the decay trap. If the response of the spectrometer to a mono-energetic collection of recoiling ions is known, it is sufficient to fold the initial energy distribution of the recoil ions with this response function to find the shape of the measured spectrum. Good knowledge of the behavior of the response function is therefore of extreme importance for a successful interpretation of an experimental spectrum obtained with the WITCH set-up.

Assume an ideal retardation spectrometer in which the retardation field is everywhere parallel to the magnetic field, which itself falls off smoothly between two homogenous field regions. The axial kinetic energy distribution of a mono-energetic collection of isotropically emitted recoil ions with energy T_r can be written as

$$\frac{dN}{dT_{\|2}} = \frac{dN}{d\theta}\frac{d\theta}{dT_{\|2}}. \tag{7.6}$$

Note that in this expression $N = N(T_{\|2})$ represents the number of ions that have an axial energy smaller than $T_{\|2}$. By exploiting the fact that the charged particles are emitted isotropically and by using expression 7.4 one can show that

$$\frac{dN}{dT_{\parallel 2}} = \frac{\sin\theta}{\sin\theta\cos\theta}\frac{\pi}{T_r}\frac{B_1}{B_2}. \tag{7.7}$$

By performing a variable transformation $\theta \to T_{\parallel 2}$, the axial energy distribution function is defined in the interval $\left]T_r\left(1-\frac{B_2}{B_1}\right), T_r\right]$ as

$$\frac{dN}{dT_{\parallel 2}} = R_d\left(T_{\parallel 2}, T_r\right) = \frac{B_1}{B_2}\frac{\pi}{T_r\sqrt{1-\left[1-\frac{T_{\parallel 2}}{T_r}\right]\frac{B_1}{B_2}}} \tag{7.8}$$

and 0 elsewhere. The response function $R_d(T_{\parallel 2}, T_r)$, that is exactly the axial energy distribution function for a mono-energetic peak, is labelled with index $_d$ following the convention of the recoil spectra of chapter 3 since it is the differential equivalent of the spectrum one would measure with the spectrometer. Expression 7.7 has not been simplified intentionally, because it gives insight in the shape of the response function. The $\sin\theta\cos\theta$ in the denominator comes from the fact that when approaching the angles θ=0° and 90° a small energy interval $dT_{\parallel 2}$ corresponds to an increasing interval $d\theta$ as can be seen from equation 7.4. At θ=0° this effect is however cancelled, since for isotropic emission the number of emitted particles decreases when approaching 0°. This explains why the differential response function $R_d\left(T_{\parallel 2}, T_r\right)$ goes to infinity at low axial energies but stays finite at T_r.

The actual response function $R_i(T_{\parallel 2}, T_r)$ of the ideal retardation spectrometer can be found by integrating $R_d(T_{\parallel 2}, T_r))$ from $T_{\parallel 2}$ till ∞. This is shown in figure 7.2.

7.2 Layout of the spectrometer

7.2.1 Design phase

The WITCH spectrometer shares the principle of magnetic energy conversion and electrostatic retardation to perform the recoil energy analysis with the Mainz and Troitsk set-ups . Apart from the fact that the WITCH set-up exploits the Penning trap technology to contain the source, the most important difference with the other set-ups is the way the particles are focussed onto the

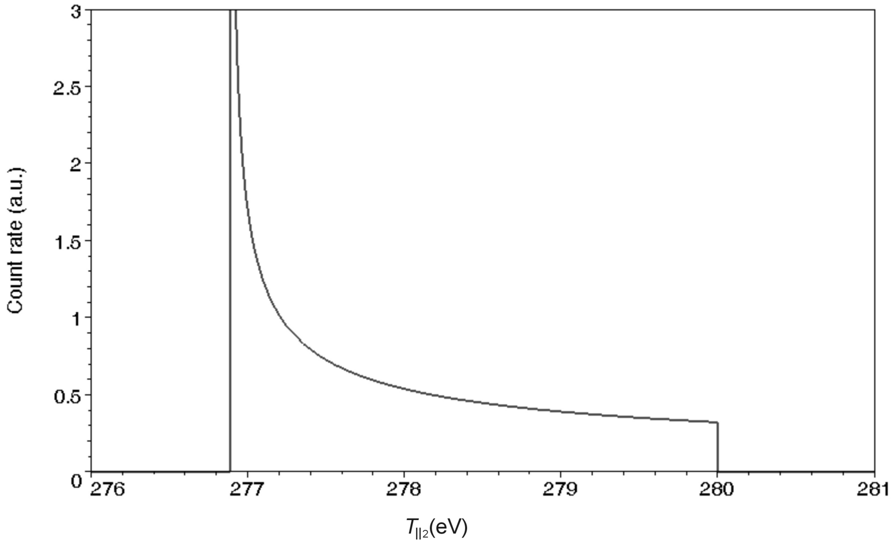

Figure 7.1: Differential form of the response function $R_d\left(T_{\|2}, T_r\right)$ of an ideal retardation spectrometer (endpoint kinetic energy T_r=280 eV, B_1=9T, B_2=0.1T).

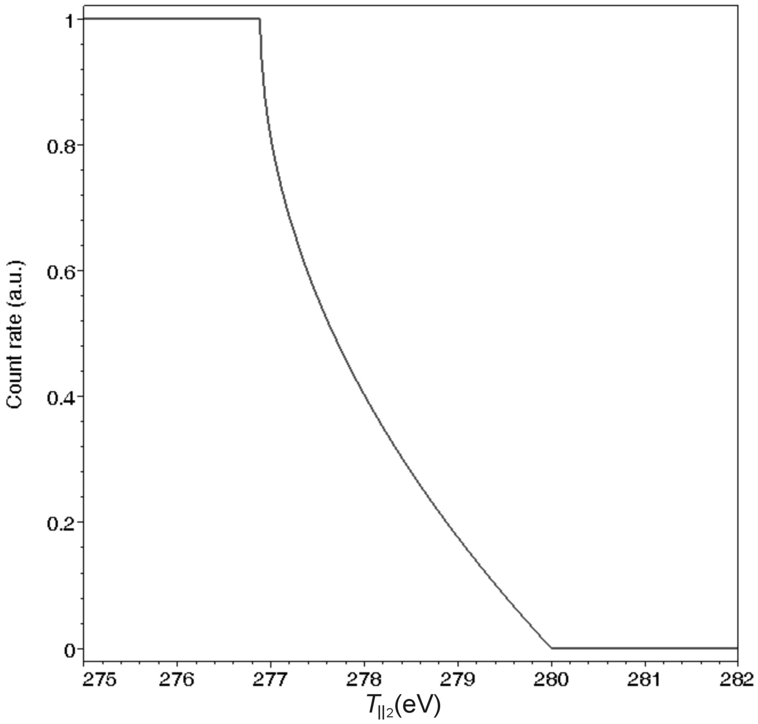

Figure 7.2: Integral response function $R_i(T_{\parallel 2}, T_r)$ of an ideal retardation spectrometer (endpoint kinetic energy T_r=280 eV, B_1=9T, B_2=0.1T).

detector. In the Mainz and Troitsk experiments this is done magnetically by placing the detector inside a strong magnetic field which causes the inverse energy conversion as the one described below. Figure 7.3 shows a schematic overview of the Mainz retardation spectrometer. Simulations of this approach for the WITCH-set-up have shown, however, that a fraction of the ions would not reach the detector due to reflection at the magnetic field gradient. This is due to the non-perfect adiabatic conversion of the energy. To avoid this problem the focussing in WITCH is performed electrostatically by an accelerating potential difference of 10 kV. The strong electric field that is created in this way takes the recoil ions off the magnetic fieldlines and an einzellens focusses the ions onto the detector. A second advantage of this solution is that the focussing electrostatic field does not influence the majority of the β particles which simply just continue their spiraling motions around the magnetic field lines. As the magnetic field has become very weak in this region the field lines strongly bend outward here so that most of the β particles end up on the wall. This prevents the measurement detector from suffering from a large β-background. A disadvantage of this approach, however, is that the beam of ions that is taken off the magnetic field lines gets large radial dimensions. This requires a detector with a large sensitive area. An interesting solution in this respect is the approach that has been chosen for the aSPECT spectrometer (Glück *et al.*, 2003) with which one intends to measure the integral recoil energy spectrum of the proton from free neutron decay. In this set-up the detector is placed into a magnetic field that is about twice as strong as the one in the source region. Accelerating the protons into the direction of the detector overcomes the magnetic mirror effect. Furthermore, the proton spot at the detector is in this case smaller than the source volume and the electron background significantly reduced by the magnetic mirror that is created.

The design of the WITCH spectrometer was an iterative process. In a first step a preliminary magnetic field configuration was chosen. Then a tentative electrode arrangement was determined taking into account the magnetic field plot for that magnet configuration. The potential of each electrode was determined by a relaxation method with the program SIMION (see section 5.2), respecting the boundary conditions imposed by the other electrodes. A Stokes force was added to the equation of motion in order to simulate the damping of the ion motion by rest gas atoms. In a next step a set of ions having a

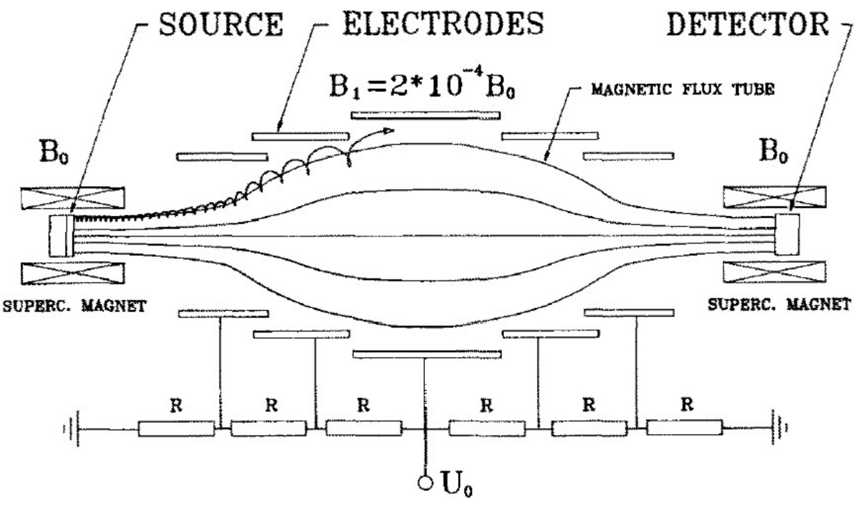

Figure 7.3: Schematic overview of the Mainz retardation spectrometer (from (Picard *et al.*, 1992)).

monochromatic energy and an isotropic emission was placed in an ion cloud in the center of the Penning trap. The recoil ion trajectories from the trap to the detector were then obtained by solving the equation of motion numerically using a 5th order Runge Kutta with adaptive step size (adopted from Press and coworkers (1996)). Typically around 10^8 trajectories were calculated for a given electrode structure. As a result, the properties of the spectrometer were obtained for a given configuration. This process was repeated for different arrangements of electrodes and magnets in order to maximize the transmission of the spectrometer and to get the best possible resolution.

The resulting retardation electrode design consists of six electrodes on which gradually increasing voltages are applied up to the maximal value U_{ret} on the last electrode. The values of these voltages as well as the dimensions of the electrodes are listed in table 7.1. Figure 7.4 shows the electrode structure of the retardation spectrometer as well as the electrostatic potential lines and the magnetic field on the magnet axis. One can see that the strongest retardation is performed shortly after the decay trap. In order to minimize the radial dependence of the potential in the analysis plane, the last retardation electrode

Table 7.1: Dimensions and voltages being applied on the retardation spectrometer electrodes.

Electrode name	Voltage [% of U_{ret}]	Diameter [mm]	Length [mm]
SPRETA01	0	120	145.5
SPRETA02	30	120	48.5
SPRETA03	60	120	48.5
SPRETA04	80	120	3
SPRETA05	80	240	140
SPRETA06	100	358	1193

has a length of almost 1200 mm. This reduces the relative deviation of the central potential from the applied voltage to less than 0.2%.

7.2.2 Electrode structure

The electrode structure of the retardation spectrometer is consists of cylindrical symmetric stainless steel pieces that are electrically insulated by Macor spacers. The complete structure is shown in figure 7.5 and can be subdivided into three sections:

- retardation section
- post-acceleration section
- detector chamber

The retardation section is located just after the decay trap and is built up from six electrodes (SPRETA01-06). The first three electrodes are located in the small bore tube of the 9T magnet, the last three in the 420 mm diameter bore tube. The retardation section is ”closed” by a thin electrode (SPRETA07). This electrode, at a potential U_{ret}, is installed to screen the post-acceleration potentials that are located higher up from the retardation region. In between the first and second post-acceleration stage (i.e. SPACCE01 and SPACCE02) an MCP detector can be moved in and out in order to perform diagnostics of

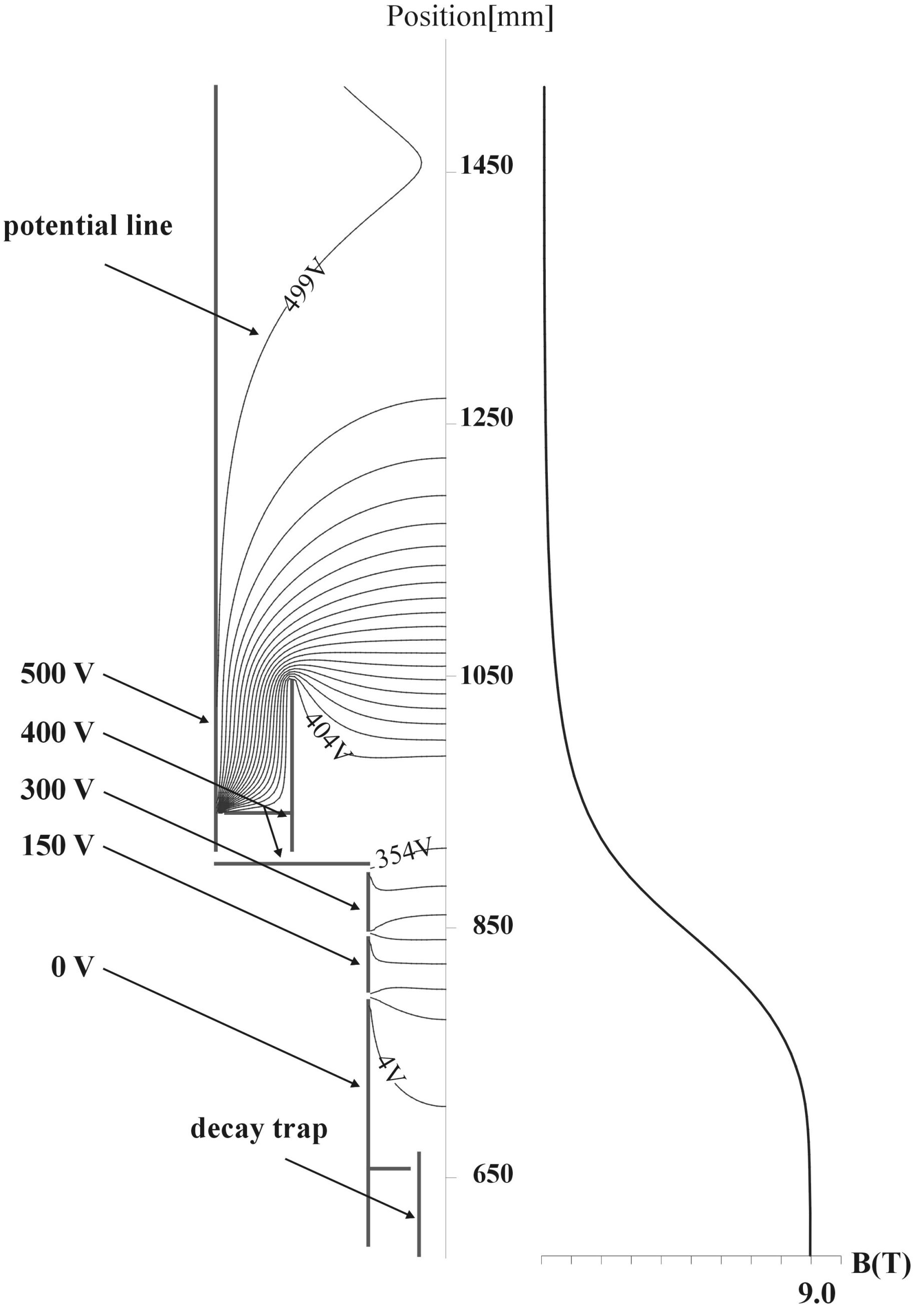

Figure 7.4: Electrostatic retardation equipotential lines and axial magnetic field strength in the spectrometer for a retardation potential U_{ret}=500 V. In the interval [4V,404V] equipotential lines are drawn for every 50V, in the interval [404V,499V] this is done for each 5V.

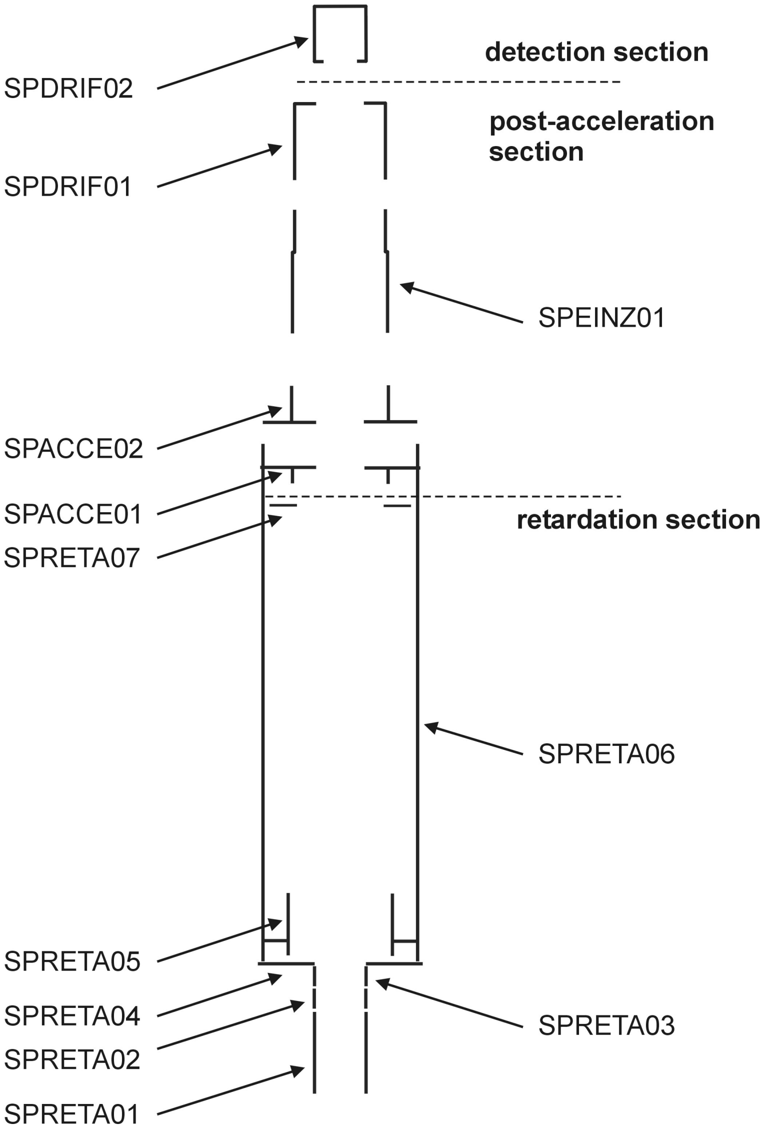

Figure 7.5: Overview of the electrode structure of the retardation spectrometer.

the ion beam coming from the decay trap. After being accelerated the beam is focussed by means of an einzellens-like structure. The central electrode (SPEINZ01) of this is cut into four pieces to allow a deflection of the ion beam. The upper part of this einzellens (SPDRIF01) has four wide and four narrow slits. The wide slits allow efficient pumping of the vacuum section. Through the narrow slits pin-diode detectors are inserted to measure the β count rate for normalization purposes.

The retardation and post-acceleration electrodes are positioned into the vacuum section of the large diameter vacuum tube of the superconducting magnet system. The complete structure is hanging at a flange that can be moved in the horizontal plane and tilted with respect to the axis of the magnet system to allow good alignment of the electrode structure. This is shown in figure 7.6.

The detector chamber is separated by a valve from the rest of the spectrometer structure. It contains an electrode that provides the -10 kV drift potential for the ions. An MCP detector is positioned onto a small trolley that can perform a translational motion in one direction. This feature allows to scan the ion beam spot on the detector during the commissioning period if the beam would exceed the sensitive area of the detector. Besides the MCP detector to measure the recoil count rate, the chamber is equipped with p-i-n-diodes for detection of the β-particles. Figure 7.7 shows the layout of the detector chamber.

7.3 Systematic effects

In section 7.1 the differential response function $R_d(T_{\|2}, T_r)$ of an ideal retardation spectrometer has been derived. In reality deviations from this theoretical shape can be expected. The real differential response of the WITCH set-up will be noted as $\tilde{R}_d(T_{\|2}, T_r)$. In this section an overview is given of six sources of systematic effects that will affect the response of the set-up:

- violation of adiabatic invariance
- influence of rest gas in the decay trap and the spectrometer
- doppler broadening due to initial ion energy

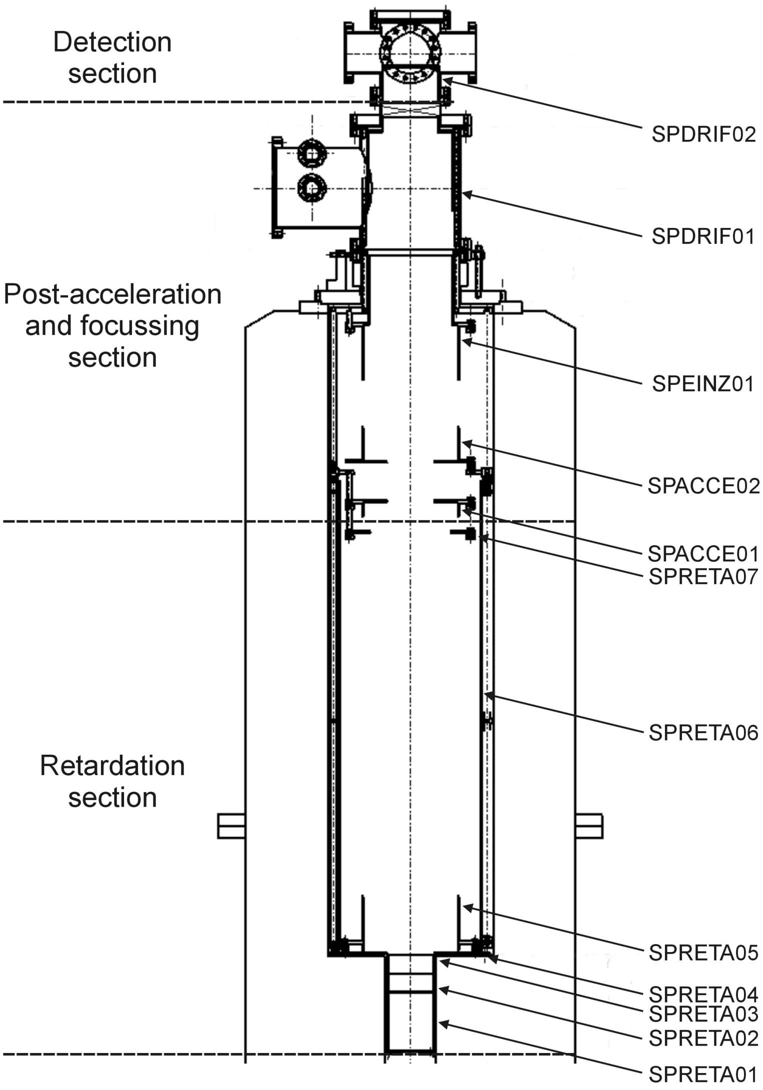

Figure 7.6: Overview of the retardation spectrometer.

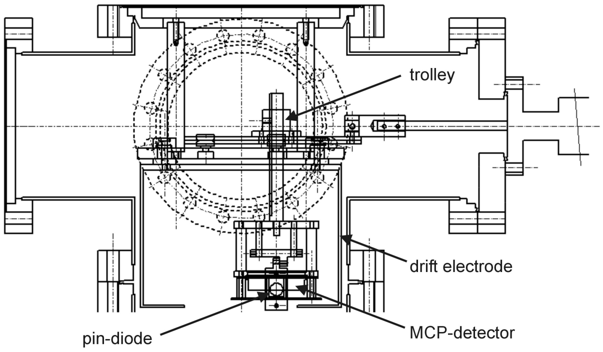

Figure 7.7: Detector chamber of the retardation spectrometer.

- trap potential
- radius dependence of retardation potential in the analysis plane
- detector related effects

A good understanding of the effects that influence the response function of the retardation spectrometer, will be crucial for controlling the systematic effects of the experiment. In what follows, the deformation of the response function for the above mentioned topics will be discussed. A powerful probe for this study is EC decay as this decay is characterized by a mono-energetic recoil peak. The EC recoil spectrum is exactly the response function of the set-up so that the study of the EC lines allows to investigate possible deformations of the retardation spectrometer. The small ratio of EC/β^+, however, could make it difficult to use the EC peaks for the systematic effect studies since it is not possible to get good statistics on a reasonable time scale. A good candidate is to be found. As soon as the deformation of the response function is well understood, an estimate has to be made on how it influences the accuracy on the a-parameter. This has not yet been performed.

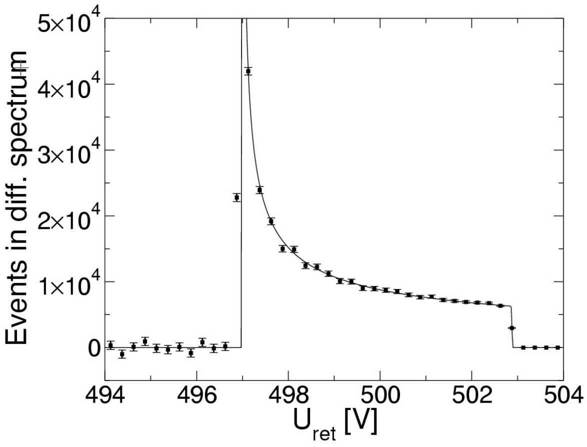

Figure 7.8: Comparison between a simulated response function for a mono-energetic recoil peak and the analytical expression $R(T_{\|2}, T_r)$.

7.3.1 Violation of adiabatic invariance

All considerations up to now have been performed within the adiabatic approximation, in which the conversion from radial into axial energy occurs perfectly and the retarding electric field is parallel to the magnetic field lines. In reality a perfect situation cannot be realized. However, one should investigate how good these assumptions are. This has been performed by simulating ion trajectories through the electromagnetic fields of the spectrometer and comparing this spectrum to the theoretical response function. This is shown in figure 7.8. The agreement between the simulated shape and the theoretical expression is very good, which can be interpreted as a prove that the adiabatic approximation describes the electromagnetic environment of the spectrometer very well.

It is important to note here that the adiabaticity check is only performed for a mono-energetic peak and not for all ions in a continuous recoil spectrum. It can be expected that the adiabaticity of the trajectories from ions close to the endpoint of the spectrum worsens when the retardation barrier is e.g. at half the endpoint energy since in this case the ion will travel with a larger momentum through the spectrometer. This is thought to be the reason why the use of a magnetic field to focuss the ions onto the measurement detector as is done in the Mainz an Troitsk spectrometer, does not work in the case of the WITCH spectrometer. For the energy filtering performed in the spectrometer the worse adiabaticity of the endpoint ions is, however, not crucial since they any how be able to pass the low retardation barrier.

7.3.2 Presence of rest gas

The presence of rest gas atoms and molecules inside the decay trap and the spectrometer volume can disturb the recoil energy measurement in two ways. First of all, the kinetic energy of the recoil ions can be disturbed by scattering (both elastic and inelastic). Secondly charge exchange processes will lead to neutralization of a number of ions that are then lost for the experiment.

To estimate the effect of scattering onto rest gas atoms, ion trajectories have been simulated, taking into account the rest gas as a Stokes force as discussed in subsection 6.1.3. Figure 7.9 shows the effect of this drag force on the shape of the response function for different pressures. With increasing pressure the energy distribution broadens and shifts to lower energies. The small deviation between the curve corresponding to $p = 10^{-6}$ mbar and the absence of the Stokes force ($p = 0$ mbar) suggests that a pressure below $p = 10^{-6}$ mbar should be sufficient to minimize the effect of the rest gas. One should however keep in mind that the Stokes force approach is a good approximation as long as the mean effect of different scattering events can be described as a retardation along the ion velocity. Going to lower pressures the validity of this approximation can be questioned. Although the calculations that have been performed in the context of the aSPECT spectrometer cannot be applied directly on the WITCH set-up circumstances, it is still interesting to note that the critical pressures that should be reached to allow a measurement of the a parameter with a precision of $5 \cdot 10^{-4}$ is of the order of 10^{-8} mbar (Glück *et al.*, 2003).

For the effect of charge exchange no quantitative estimates has been made so far for the WITCH experiment. Based on the observations at ISOLTRAP, that have been discussed in subsection 6.1.4, the ion loss due to charge exchange is expected to be negligible. Simulations performed in the context of the aSPECT set-up result in a critical pressure of the order of 10^{-8} mbar for most molecules present in air and 10^{-6} mbar for He. Again, the results which are specifically

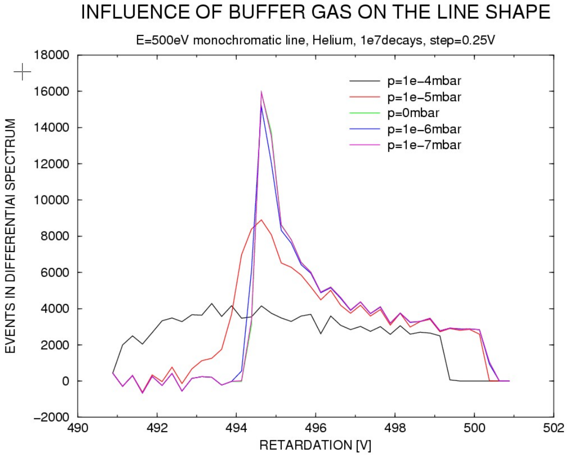

Figure 7.9: Effect of rest gas atoms at different pressure on the shape of the response function in the Stokes force approximation.

for the proton cannot be applied to the WITCH circumstances but should rather be considered as an order of magnitude estimate. For both processes further investigation is necessary.

7.3.3 Doppler broadening

Since the ions stored in the decay trap are not at rest, the velocity $\mathbf{v_f}$ with which they leave the trap after beta decay is given by the vector sum $\mathbf{v}_f = \mathbf{v}_i + \mathbf{v}_r$ where the indices $_i$ and $_r$ refer to initial, respectively recoil velocity. If T_r denotes the recoil energy of the ion in its center of mass frame then the kinetic energy of the ion in the laboratory frame is shifted by the amount ϵ given by

$$\epsilon = T_f - T_r = \frac{m}{2}\left[(v_{ix} + v_r)^2 + v_{iy}^2 + v_{iz}^2\right] - \frac{m}{2}v_r^2 = T_i + m v_{ix} v_r, \tag{7.9}$$

assuming the axis system is chosen to have the x-axis parallel to the recoil direction. For an ion cloud at room temperature the initial ion velocity is typically two orders of magnitude smaller than the recoil velocity. In this case the energy change is $\epsilon \approx m v_{ix} v_r$.

To determine how this energy shift is distributed one should note that

$$\frac{dN}{d\epsilon} = \frac{dN}{dv_{ix}} \frac{dv_{ix}}{d\epsilon}. \tag{7.10}$$

Assuming that the initial velocity component in the x-direction obeys a one-dimensional Maxwell velocity distribution, one can write that

$$\frac{dN}{dv_{ix}} = \frac{1}{\sqrt{2\pi}\sigma_x} \exp\left(\frac{-v_{ix}^2}{2\sigma_x^2}\right), \tag{7.11}$$

with

$$\sigma_x = \sqrt{\frac{kT}{m}}. \tag{7.12}$$

This results in the Gaussian distribution function for the energy shift ϵ

$$f_\epsilon = \frac{dN}{d\epsilon} = \frac{1}{\sqrt{2\pi}\sigma_\epsilon} \exp\left(\frac{-\epsilon^2}{2\sigma_\epsilon^2}\right), \tag{7.13}$$

with

$$\sigma_\epsilon = m v_r \sigma_x. \tag{7.14}$$

This indicates that the initial thermal energy of the ions in the trap broadens the energy of mono-energetic recoil ions significantly. For a given recoil energy the broadening is independent of the mass of the ion as can be seen from the mass dependencies of the three factors in equation 7.14. For a cloud of ions at room temperature in which the ions gain a recoil energy of T_r=280 eV σ_ϵ= 3.8 eV. The dependence of the width of the Doppler broadened mono-energetic recoil peak is shown in figure 7.10 as a function of the temperature for recoil energies T_r=140 eV and 280 eV.

The response function of the spectrometer that includes the effect of the initial ion energy can be found by folding the broadened energy distribution by the ideal response function

$$\tilde{R}_d(T_f) = \int_0^\infty f_\epsilon(y) R_d(y, T_f) dy \tag{7.15}$$

Figure 7.11 shows the shape of the response function taking into account the initial energy of the ions, and this for four different temperatures. For an ion cloud at room temperature as well as at liquid nitrogen temperature the

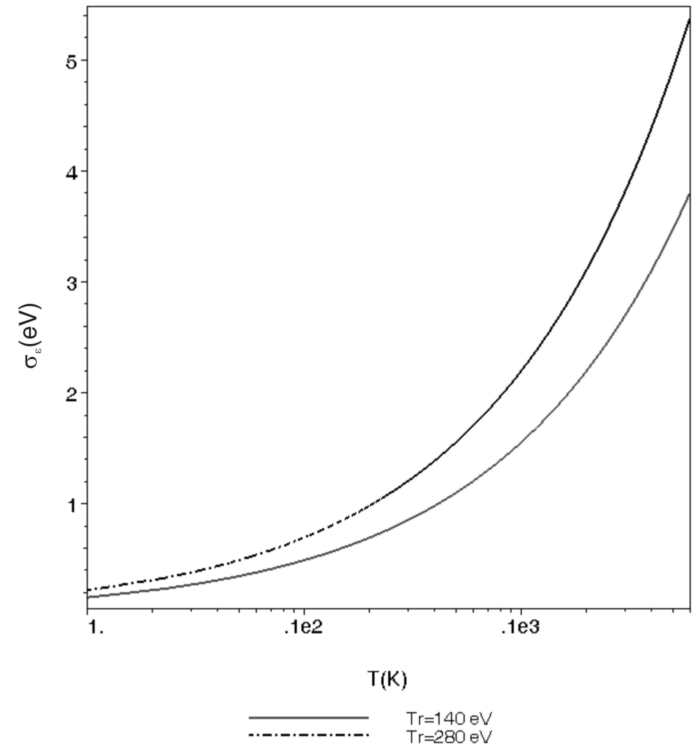

Figure 7.10: Dependence of the energy spread σ_ϵ for two mono-energetic recoil peaks (with T_r =140 eV and 280 eV) as a function of temperature of the ion cloud, caused by the initial thermal energy.

response function is completely determined by the energy broadening of the cloud. It is only at really low temperatures of the order of 1K, that the shape of the ideal response function can be distinguished from the initial energy distribution.

Note that in this treatment the ion cloud has been assumed to be a gas of non-interacting particles in thermal equilibrium. No effects due to the trap potential or the Coulomb repulsion have been taken into account. Therefore the derivation of the effect of the Doppler broadening on the response function can only be considered as a first order approach that needs further refinement to get a more accurate description.

7.3.4 Trapped after decay

Since the ions are still located inside the potential well of the Penning trap just after their decay, they need to have sufficient axial kinetic energy to reach the spectrometer. Since the axial kinetic energy of the recoil ions depends on the recoil angle θ with respect to the magnetic field axis via

$$T_{\parallel 1} = T_r \cos^2 \theta, \tag{7.16}$$

it is clear that for each energy a critical angle exists above which no ions can escape the electrostatic well. This angle is called the cut-off angle and can be calculated as

$$\theta_c = \arccos \sqrt{\frac{eU_C}{T_r}}, \tag{7.17}$$

where U_C is the cut-off voltage defined by the potential difference between the maximal potential in the center of the end cap electrode and the center of the trap. Figure 7.12 shows how the cut-off angle θ_C changes for different recoil energies. When the recoil energy $T_r = eU_C$, $\theta_C = 0$ and no ion can escape from the trap potential.

Assuming an isotropic distribution of recoil directions, the fraction P_C of ions that stay trapped is given by

$$P_C = \sqrt{\frac{eU_C}{T_0}} \tag{7.18}$$

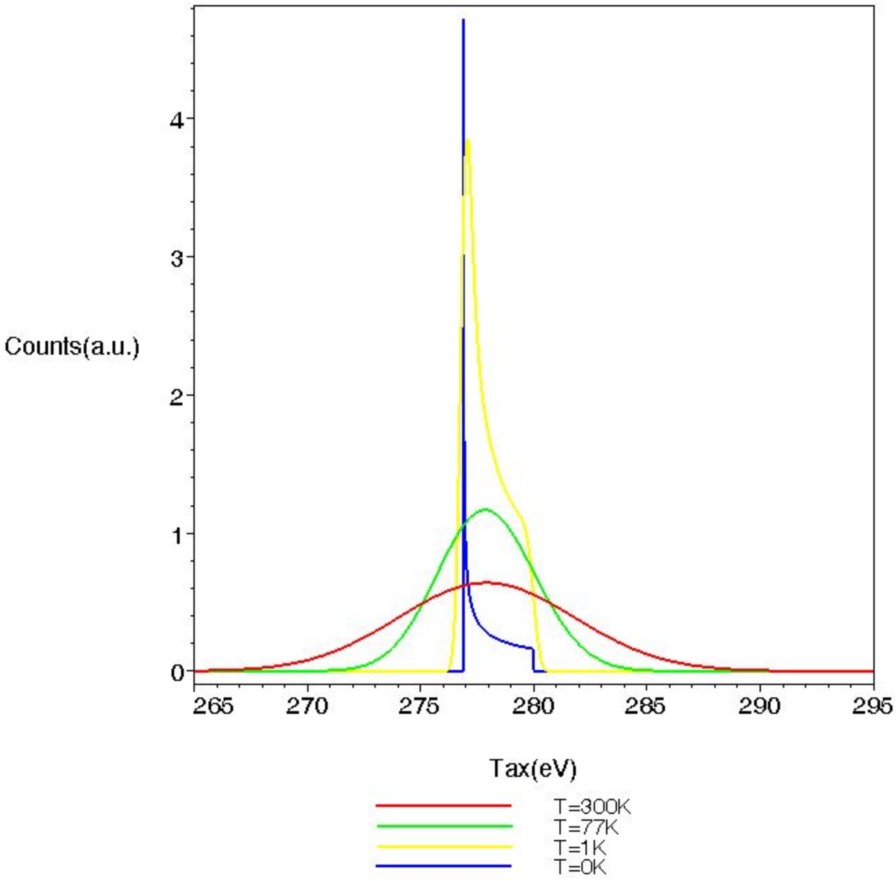

Figure 7.11: Response function of the spectrometer for a mono-energetic peak of recoil ions inside an ion cloud at four different temperatures.

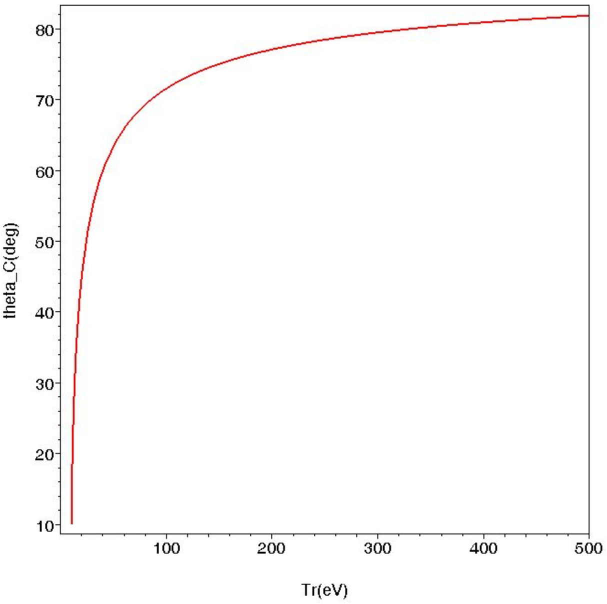

Figure 7.12: Cut off angle θ_C as a function of the recoil energy T_r with cut-off barrier $U_C = 10V$.

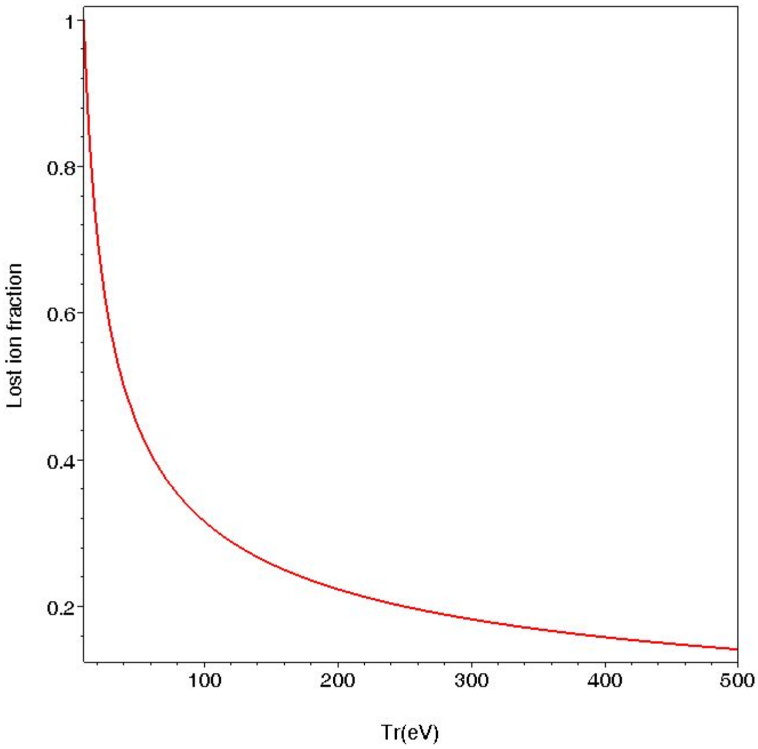

Figure 7.13: Fraction of a collection of isotropically emitted recoil ions with energy T_r that stay trapped, as a function of the recoil energy T_r (U_C=10V).

Figure 7.13 shows the fraction of the ions that does not reach the spectrometer. Focussing on the upper half of the spectrum that will be measured in the first experiments with the WITCH set-up, figure 7.13 shows that the ion loss will be of the order of 20% for a recoil spectrum with endpoint of 300 eV and for a cut-off barrier U_C=10 V.

Since the ideal differential response function $R_d(T_{\|2}, T_r)$ depends in a clear way on the emission angle θ it is easily seen that the cut-off effect will remove the left tail of the response function and this depending on the recoil energy of the mono-energetic peak. Inserting expression 7.17 into equation 7.4 gives the

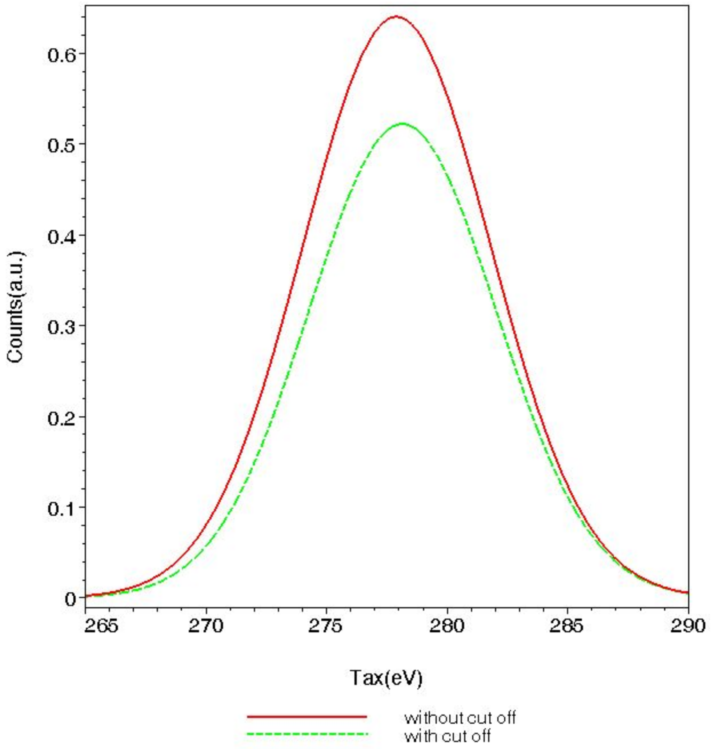

Figure 7.14: Response function with and without cut-off due to the trap potential for a mono-energetic peak at T_r=280 eV. (U_C=10V).

lower limit for the interval over which the response function is non zero as

$$T_C^{min} = T_r \left[1 - \frac{B_2}{B_1} \left(1 - \frac{eU_C}{T_r} \right) \right] \tag{7.19}$$

The effect on the Doppler modified response function is shown in figure 7.14 for a 280 eV mono-energetic peak. Two differences can be noted. First of all the area under the curve decreases when introducing the cut-off. This is due to the fact that a fraction of the ions cannot escape out of the potential well. The trap potential acts as an electrostatic collimator blocking the ions that are emitted at an angle larger than θ_C. Secondly the curve shifts slightly to higher energies.

7.3.5 Radius dependence of retardation potential in analysis plane

Since the large retardation electrode on which the maximal retardation voltage U_{ret} is applied has a finite length, the potential in the analysis plane is not constant in radial direction but increases when approaching the electrode wall. This is shown in figure 7.15 for an applied retardation potential of 500V. The potential difference between the center and the wall of the electrode is 1.01V in this case. This will imply that ions spiraling close to the magnetic axis will encounter a lower retardation barrier then the ions following a field line at a bigger radius. The effect of this on the response function can be described by a shift to lower retardation values for larger radii.

7.3.6 Detector related effects

The detector that is used to count the recoil ions that pass the retardation barrier is also a possible source of systematic effects.

A direct energy dependent effect between two ions with different recoil energies is not expected. The reason is that the ions are accelerated up to 10 keV such that the energy difference between ions in the beginning and at the end of the recoil spectrum,is reduced to 5% for an endpoint energy of 500 eV. Furthermore in this energy range the efficiency of an MCP detector is energy independent. However, two ions starting at the same position but with different recoil momenta will follow different trajectories and might hit the MCP detector at a different position. If the detection efficiency would be position dependent then the recoil energy difference will indirectly affect the measurement. Therefore a study of the position dependence of the efficiency of an MCP detector has been started (Coeck, 2003).

7.4 Spectral shape

Due to the shake-off process the daughter nucleus will end up in different ionic states. The height of the retardation barrier which the ions encounter in the

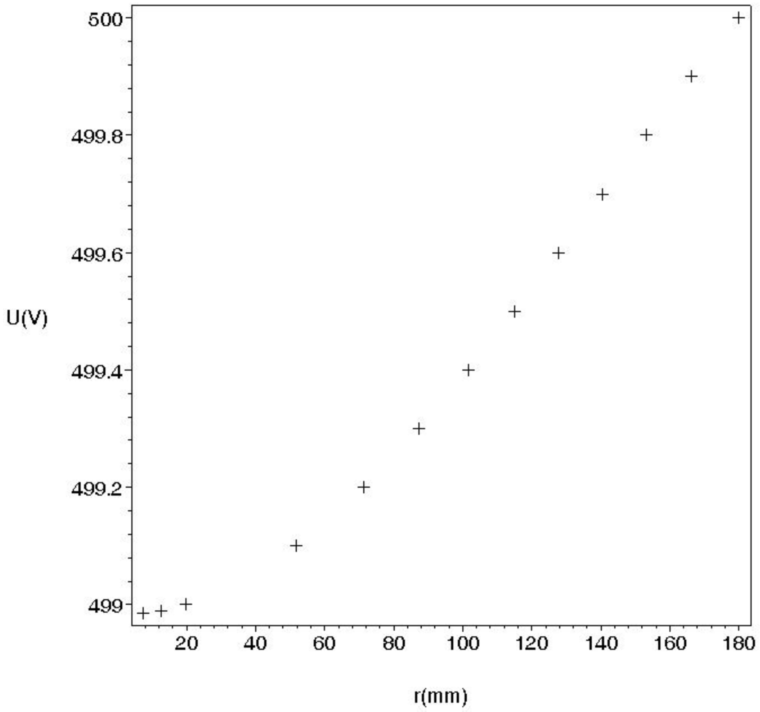

Figure 7.15: Electrostatic potential in the analysis plane of the retardation spectrometer as a function of the radius.

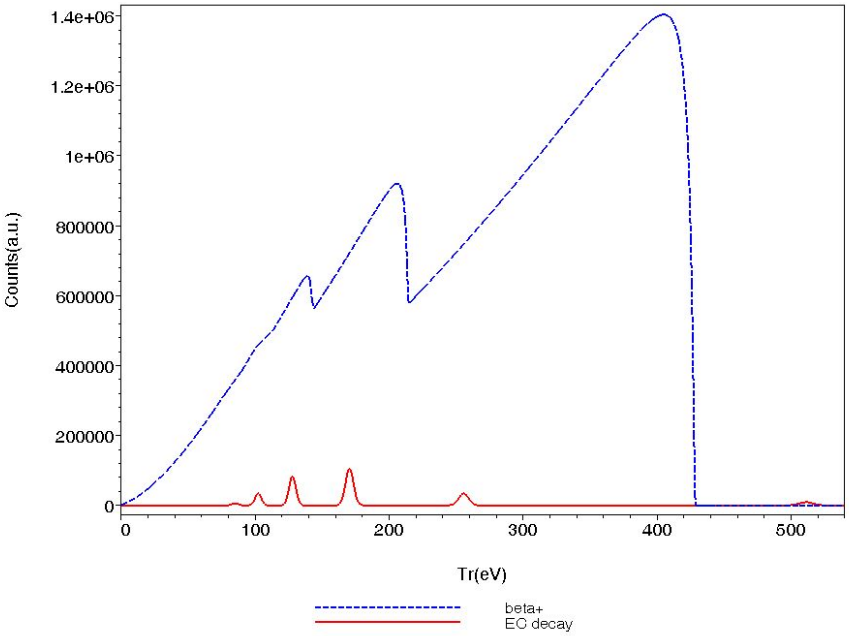

Figure 7.16: Differential recoil energy spectrum for the decay of ^{38m}K for different charge states. The charge distribution for β^+ decay is taken from Gorelov *et al.* (2000), the charge distribution for EC decay is estimated by the distribution from the pure EC-decay of ^{37}Ar (Snell and Pleasonton, 1955).

spectrometer will depend on this charge state. The neutral atoms will not be affected at all and will follow straight trajectories. The fraction of these atoms that will reach the MCP detector can be estimated to be of the order of 10^{-5} based on solid angle considerations. If the endpoint energy of singly charged ions corresponds to a retardation voltage U_{ret} then the minimal retardation voltage that blocks all daughter ions with charge q^+ is U_{ret}/q. The total spectrum will be a superposition of all charge state spectra. In the case of ^{38m}K, for which the charge state distribution has been experimentally measured (Gorelov *et al.*, 2000), figure 7.16 shows the calculated continuous differential recoil spectrum due to β^+ decay and the EC peaks with P_{EC}=0.082%. Since no data on the EC transition of ^{38m}K are available, the experimental charge state distribution of ^{37}Ar has been used (Snell and Pleasonton, 1955).

Chapter 8

WITCH experiment

In the previous three chapters a detailed overview was given on the beamline system, the double Penning trap structure and the retardation spectrometer. Taking into account the specific features of the set-up, it will be shown in the current chapter that the set-up indeed allows to achieve the statistical requirements that have been extracted from the simulations as discussed in section 3.2.

First of all a few words will be spent on the structure of a measurement cycle. This is followed by a discussion of the overall efficiency of the WITCH set-up. By combing the conclusions of those two topics an estimate will be made of the total measurement needed to achieve a statistical precision of 0.5% on the $\beta-\nu$ correlation coefficient a. This will be applied to different candidate isotopes for scalar current searches. At the end the contamination, normalization and calibration of the spectrum will be briefly touched.

8.1 Measurement cycle

An experiment with the WITCH set-up consists of a continuous repetition of the same measurement cycle for a different ion bunch stored in the decay trap. This cycle consists of a number of steps that are schematically shown in

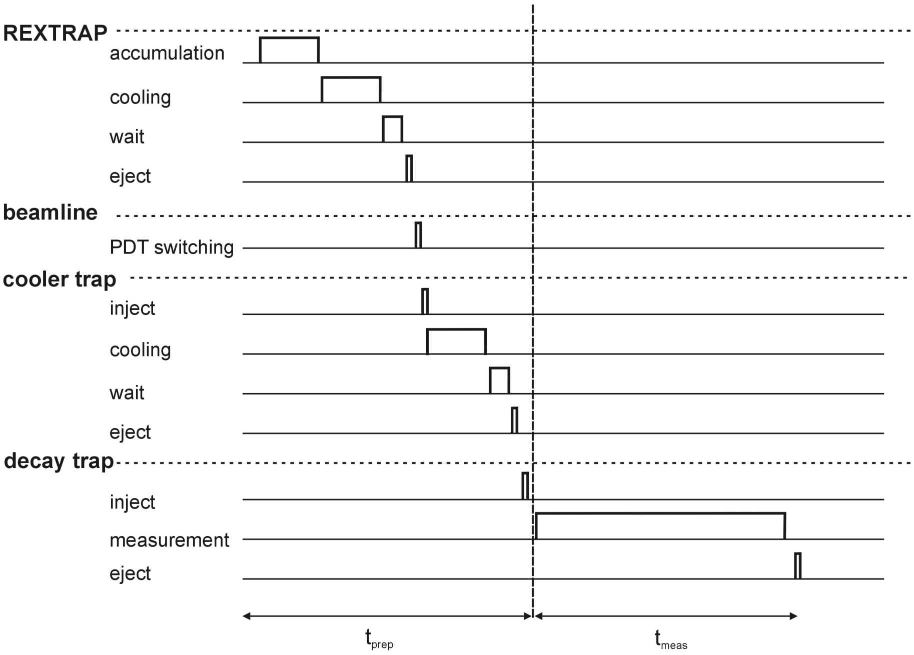

Figure 8.1: Schematic overview of the different steps contained in one measurement cycle. The time axis is not to scale.

figure 8.1.

REXTRAP accumulates the DC ISOLDE beam during a time t_{acc} after which the ions are cooled for a time period t_{coolR} by applying an RF quadrupole electric field in combination with the presence of buffer gas atoms. The quadrupole excitation is followed by a waiting period to let the cyclotron motion be cooled by means of collisions with the buffer gas atoms. The REXTRAP task ends after ejection of the ion bunch.

After passing through the pulsed drift section, the ion bunch is injected into the cooler trap where the same cooling scenario takes place as in REXTRAP with cooling time noted as t_{coolW}. Then the ion bunch is transferred to the decay trap where it is stored for a time period t_{meas} during which the number of recoil ions that cross the retardation barrier in the spectrometer is counted. After this measurement period the ions that are left in the decay trap are ejected.

To determine the cycle period of the WITCH set-up one should note that the preparation of one ion bunch can be performed while another one is stored in the decay trap and recoil ions are detected. This means that one cycle period t_{cycle} is defined by the maximum of t_{prep} and t_{meas}. In its present configuration a lower limit of 1 s on the cycle duration is placed by the switching system of the pulsed drift section as discussed in subsection 5.3.2.

8.2 Total efficiency

The total efficiency of the WITCH set-up is defined by the fraction of ions in the bunch delivered by REXTRAP that is counted at the measurement detector of the WITCH set-up in the case no retardation potential is applied. Table 8.1 lists the estimated efficiencies for different parts of the set-up. In the text the different contributions to the overall efficiency are discussed for the current WITCH set-up. For some aspects possible improvements that can increase the efficiency are mentioned.

Transfer and injection into cooler trap This contains the transfer of an ion bunch ejected from REXTRAP, the transport through the beamline system and injection into the cooler trap. This efficiency is estimated in the context of the pulsed drift cavity to be 30 % (see section 5.3).

Ion loss during cooling Due to charge exchange with rest gas atoms and molecules, trapped ions can get neutralized as discussed in 6.1.4. It is hard to make any estimate concerning this loss. It should however be noted that the difference in charge exchange rate can vary over an order of magnitude depending on the element that is trapped. The effect of charge exchange during the cooling process can be investigated experimentally by measuring the number of ions before and after cooling. This test should be performed without differential pumping diaphragm to avoid that ions that are cooled to a radius, larger than this diaphragm opening, would be considered as lost due to charge exchange.

Decay during cooling A fraction of the ions will decay during the time they are being cooled, increasing for larger cooling times. For isotopes with half lives of the order of seconds the loss is one to a few percent (t_{coolW}=20ms).

Transfer to decay trap As discussed in subsection 6.3.3 this loss depends on the radial extension of the ion cloud. For an ion cloud of 3 mm FWHM in radial direction and a diaphragm radius of 2 mm the transmission efficiency is of the order of 80%.

Ion loss in decay trap Also in the decay trap charge exchange can neutralize ions. The pressure inside the decay trap will be lower than in the cooler trap but on the other hand the storage time times will be much longer (of the order of seconds) as is discussed further down. This efficiency factor can also be measured.

Acceptance of upper hemisphere In the current experimental configuration the ions recoiling into the lower hemisphere of the decay trap, i.e. the one that is oriented to the cooler trap, will hit the electrode of the differential pumping diaphragm and get lost. This corresponds to an efficiency of 50%. By introducing an electrostatic mirror in the lower half of the decay trap, it should be possible to accept decays in a solid angle of 4π.

Shake-off In order to end up with a singly charged ion, the daughter nucleus of the β decay should shake-off one orbital electron. To get an estimate from data in the literature one should however look for rates that represent two electron loss since the mother ion was in a 1^+ charge state in the WITCH set-up. Two measurements of the shake-off charge state distribution for β^+ emitters give 18.6 % (Scielzo *et al.*, 2003) for ^{21}Na and of the order 10% on ^{38m}K (Gorelov *et al.*, 2000). One should note that when performing experiments on β^- emitters or EC decays no neutral daughter atoms are produced. In this way the daughter ions that have not lost any orbital electron can also be detected, increasing the efficiency with a factor of the order of 5.

Trapped after decay When the axial velocity component of the recoil ion does not allow to leave the potential well of the Penning trap then the ions do not reach the spectrometer. The fraction of ions in the upper half of the spectrum (with 300 eV endpoint energy) that stays trapped is expected to be 20% (see subsection 7.3.4)

Ion loss in spectrometer Possible loss mechanism of ions in the spectrometer are charge exchange with rest gas atoms or ion trajectories that touch electrode surfaces. By keeping the radial dimensions of the ion cloud small the latter effect is expected to be small. The former is also expected to be small from the observations at ISOLTRAP discussed in subsection 6.1.4.

Detector efficiency The MCP detector that is planned to be used in the first experiments has an efficiency of 30%. More advanced MCP detectors can have efficiencies of the order of 60%. This can lead to a gain of a factor of two in future.

Without taking into account the two loss factors due to charge exchange in the two traps, the overall efficiency of the WITCH set-up is $eff(\infty) = 2.8 \cdot 10^{-3}$ for a measurement that would last till all nuclei have decayed. If the measurement time is finite the efficiency should be multiplied with the time dependent function that gives the number of decayed nuclei during t_{meas}:

$$eff(t_{meas}) = eff(\infty)\left[1 - \exp\left(\frac{-\ln(2)t_{meas}}{t_{1/2}}\right)\right] \tag{8.1}$$

8.3 Total measurement time

As is shown in figure 3.5 the accuracy of the fitted a-parameter from an experimental recoil spectrum depends on the number of counts N_{stat} in the corresponding differential spectrum. This can be realized by letting N_{stat} nuclei decay and measuring the recoil energy for each of them. If the experimental apparatus measures the count rate in only one energy interval at the time, the total number of necessary decays is given by $N_{dec} = N_{stat}N_{bin}$, where N_{bin} is the number of bins to cover the complete energy range of the spectrum. For an integral measurement technique in which the content of two neighboring bins is subtracted to reconstruct the original spectrum, this increases to $N_{dec} = N_{stat}(N_{bin} + 1)$.

Table 8.1: Summary of efficiency of WITCH set-up. The two factors related to REXTRAP have not been included in the total efficiency calculation.

Description	Efficiency
transport ISOLDE to REXTRAP (Schmidt, 2001)	0.85
REXTRAP efficiency (Ames *et al.*, 2002)	0.4
transfer + injection into cooler trap	0.3
loss during cooling	?
decay during cooling (20 ms)	≈0.99
transfer to decay trap	0.8
loss in decay trap	?
acceptance of half a hemisphere	0.5
trapped after decay	0.8
shake-off of 1 orbital electron	0.1
loss in spectrometer	1
detector efficiency	0.3
total efficiency $eff(t_{meas=\infty})$	0.0028

To apply this to a real experiment one should take into account the efficiency of the set-up. Therefore the total number of ions that have to be delivered to the set-up to obtain N_{dec} useful decays, is given by $N_{tot} = N_{dec}/eff(t_{meas})$. If the number of ions in one REXTRAP bunch for one measurement cycle is represented by N_{bun}, the total measurement time becomes

$$t_{tot} = \frac{N_{tot}}{N_{bun}} t_{cycle} = \frac{N_{stat}(N_{bin} + 1)}{N_{bun} eff(t_{meas})} t_{cycle}. \tag{8.2}$$

Aiming at a precision of 0.5% means that N_{stat} should be of the order of $10^7 - 10^8$. All values that will be mentioned further down for measurement times assume $N_{stat} = 10^8$.

For a certain isotope with half-life $t_{1/2}$ and production rate I_{IS}, an important parameter that allows to optimize the total measurement time is the time one keeps the ions in the decay trap t_{meas}. Since in an exponential decay the highest count rate is achieved close to $t = 0$ one would expect that t_{tot} would decrease for shortened individual measurements t_{meas}. This is indeed the case as long as $t_{meas} > t_{prep}$. In case the preparation period is longer than t_{meas} the period of one cycle is now determined by t_{prep} and will stay roughly constant for decreasing t_{meas}. Therefore, in this time region the total measurement time increases as the individual measurement time is shortened. This behavior is shown in figure 8.2 for the isotope ^{35}Ar where $N_{stat} = 10^8$ and $N_{bin} = 20$. The four curves represent the total measurement time for four different REXTRAP bunches, which are varied by changing the accumulation period t_{acc}. All curves have a minimum around $t_{meas} \approx t_{acc}$ representing the optimal choice of t_{meas}. Assuming that 10^6 ions can be handled in the cooler trap, the total measurement time for the set-up efficiencies as stated in table 8.1 and t_{meas}=1 is 8.17 days .

Another interesting conclusion can be drawn from this figure by looking to the evolution of the curve as a function of the different decay trap fillings. Even if it would be possible to handle 10^7 ions into the cooler trap then the current production yield of ^{35}Ar does not allow to reduce the measurement time with respect to the case where $5 \cdot 10^6$ are stored. The reason is that during the long accumulation time t_{acc} to reach 10^7 ions in one bunch the fraction of ion that has decayed is significant. This situation could be improved by increasing the REXTRAP efficiency as well as the transmission rate through the beamline between REXTRAP and the WITCH set-up, which reduces the t_{acc}. As discussed in section 8.2 at several positions in the set-up, improvements of the set-up could be performed. It is expected that the beamline, the recoil solid angle and detector efficiency all can be improved by about a factor of roughly 2, leading to a total efficiency of a factor of 8.

In this improved set-up it is interesting to investigate the influence of the half life $t_{1/2}$ on the total measurement time. Assuming the yields of ^{26m}Al, ^{35}Ar, ^{38m}K and ^{50}Mn would all be $I_{IS} = 2.1 \cdot 10^7$ part/s, figure 8.3 presents the total measurement time. The figure clearly shows that it is much more efficient to use shorter lived isotopes, as could be expected. This conclusion should be kept in mind if one would invest effort in target development to increase the production rate of one of the candidate isotope for the WITCH set-up. Furthermore, the effect of reducing the measurement time T_{meas} is most pronounced for the shorter half-lives.

For the improved set-up a comparison can be made between the two isotopes that are presently produced sufficiently to perform a reasonably accurate measurement on the a-parameter: ^{35}Ar and ^{38m}K. Given their present yields (^{35}Ar: $2.1 \cdot 10^7$ part/s; ^{38m}K: $6.3 \cdot 10^6$ part/s) the total measurement time is

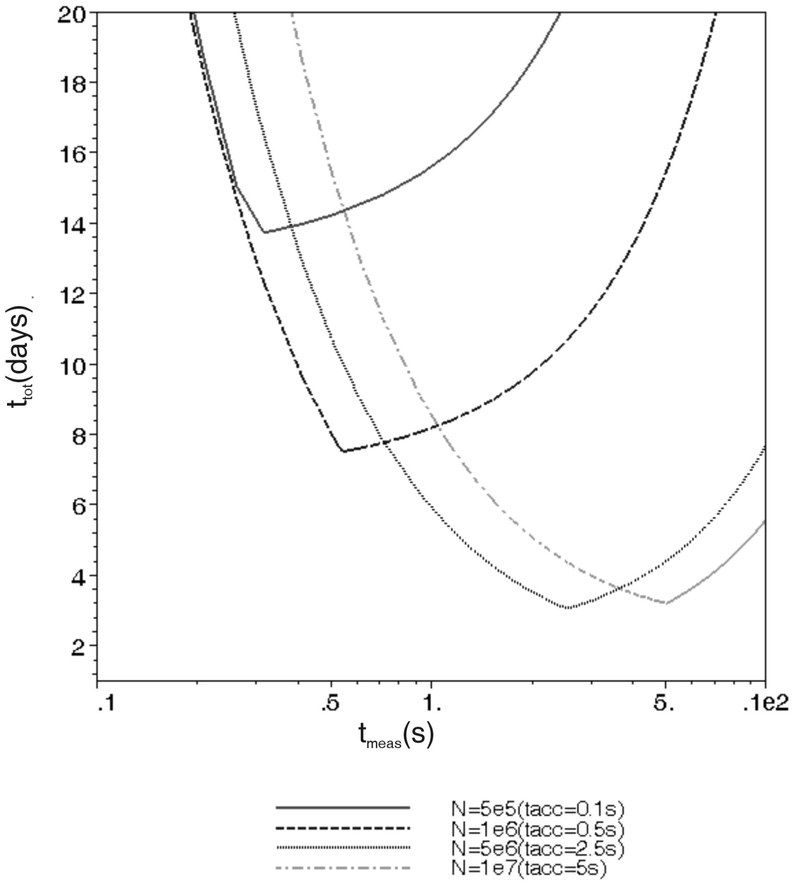

Figure 8.2: Total measurement time to achieve 10^8 ions in the differential recoil spectrum (with 20 bins) as a function of the storage time t_{meas} of one ion bunch in the decay trap for the isotope ^{35}Ar. Efficiencies are as given in table 8.1, parameters for ^{35}Ar as given in table 3.3. N denotes the number of ions in a REXTRAP bunch.

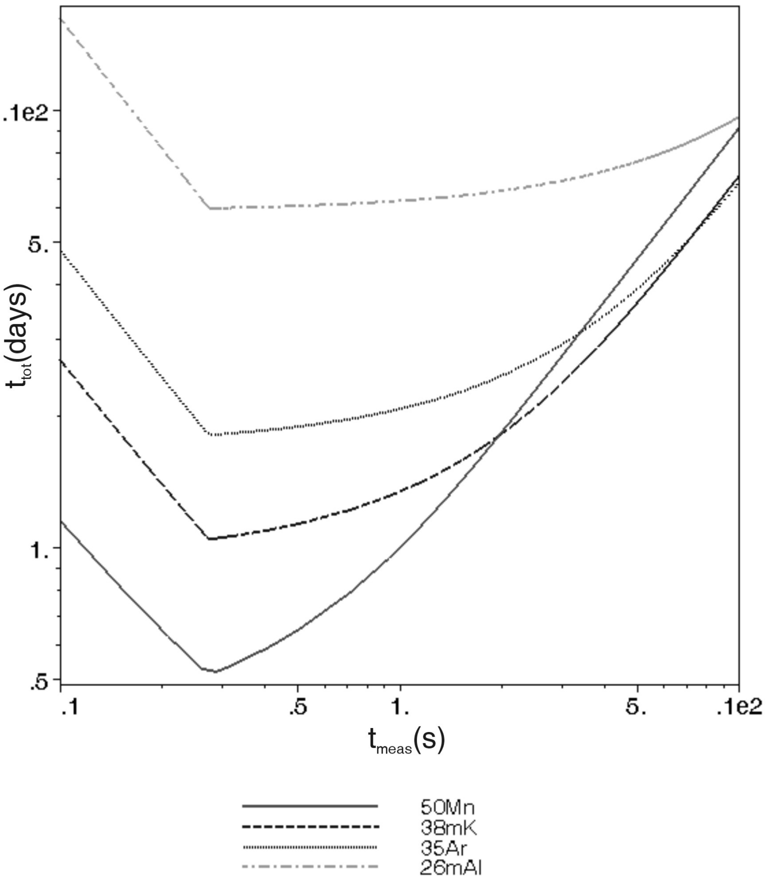

Figure 8.3: Total measurement time as a function of the storage time t_{meas} of one ion bunch in the decay trap for the isotopes ^{26m}Al ($t_{1/2}$=6.345 s), ^{35}Ar ($t_{1/2}$=1.775 s), ^{38m}K ($t_{1/2}$=0.923 s) and ^{50}Mn ($t_{1/2}$=0.283 s) assuming equal yields I_{IS}. Improved efficiencies (see text) have been used. Efficiencies are as in table 8.1 The parameters for ^{35}Ar are as given in table 3.3. $N_{stat} = 10^8$, $N_{bins} = 20$ and $N_{bun} = 10^6$.

given in figure 8.4. As can be seen from this figure, the optimal isotope choice depends on the number of ions that can be handled in the trap. If the REX-TRAP bunch contains 10^6 ions then a measurement on ^{38m}K would be finished after 1.5 days when $t_{meas} = 1$ s, while it takes slightly less than about two days in the case of ^{35}Ar. If the WITCH set-up can accept bunches with $5 \cdot 10^6$ ions then ^{35}Ar is the better candidate. One should note that in the calculation with $5 \cdot 10^6$ ions, it is assumed that there are no additional losses in cooler, decay trap or spectrometer due to the large number of ions. The charge exchange loss being larger for ^{35}Ar than for ^{38m}K is also not included.

8.4 Contamination

Up to now it has always been assumed that the isotope of interest is the only one being present in the decay trap. In practice ions of a different type can be present which can be both radioactive or stable. The stable ions take space in the decay trap that cannot be taken by the ions of interest. The same holds for radioactive ions but in addition they can also contaminate the recoil spectrum that is to be measured. To avoid having isobaric contaminants in the decay trap the HRS separation magnet should be used.

8.5 Energy calibration

The energy calibration of the recoil energy spectrum can be performed in different ways. If one measures the upper half of the spectrum the endpoints of the recoil spectrum of the singly charged ions as well as the doubly charged ions can be used. These provide a calibration at both sides of the spectral part that is to be fitted. If the EC branch of the decay is sufficiently strong, the 1^+ and 2^+ EC peaks can also be used. If necessary, additional calibration can be performed by trapping other isotopes and measuring their EC peaks.

An advantage of the EC decay for energy calibration is that although broadening of the peak occurs due to the Doppler effect from the initial motion of the ions, the central position does not shift. The endpoint of the spectrum

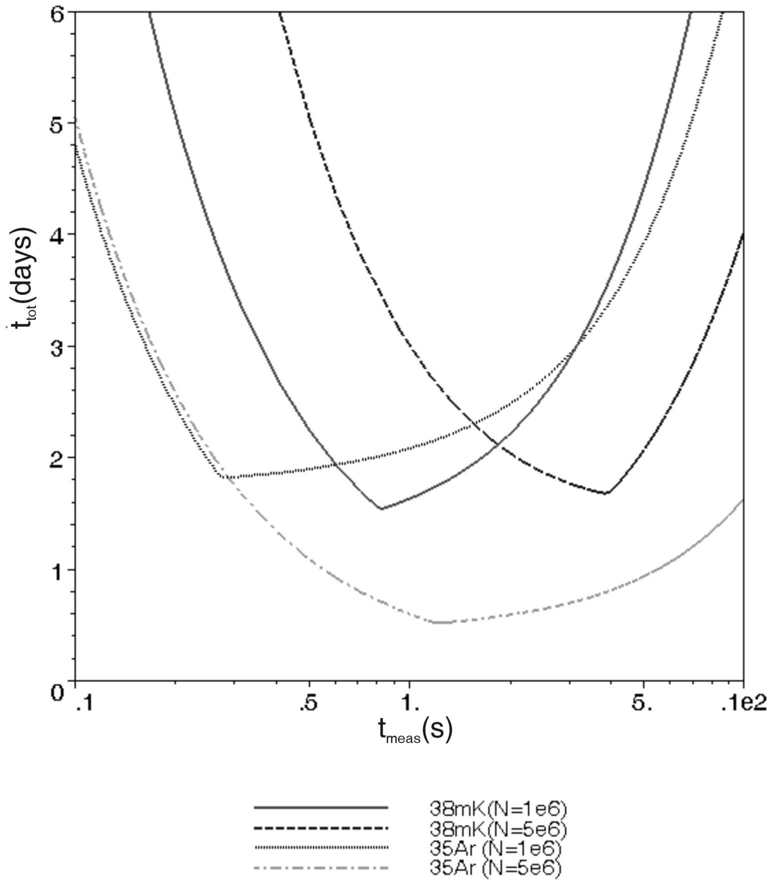

Figure 8.4: Total measurement time as a function of the storage time t_{meas} of one ion bunch in the decay trap for the isotopes ^{35}Ar ($I_{IS} = 2.1 \cdot 10^7$ part/s) and ^{38m}K ($I_{IS} = 6.3 \cdot 10^6$ part/s) and for different ion numbers in one bunch. Improved efficiencies (see text) have been used. The parameters for ^{35}Ar and ^{38m}K are as given in table 3.3. $N_{stat} = 10^8$, $N_{bins} = 20$.

however will shift to higher energies due to this Doppler effect, implying that an accurate calibration needs a good understanding of this Doppler shift.

8.6 Normalization

Since the source strength in the decay trap will vary from bunch to bunch, it is important to normalize the recoil count rate. At present three possible scenario's are envisaged:

- β particle count rate
- measurement of the remaining ions in the decay trap
- scanning the retardation voltage during one cycle

Since the β particle count rate in a detector behind the retardation barrier is not disturbed by this electrostatic potential, it is a good observable to correct for source strength fluctuations. The package GEANT4 will be used to perform β particle tracking inside the spectrometer to determine the optimal position and dimensions for the β detectors. As discussed in chapter 7 the spectrometer is equipped with p-i-n diode detectors located at different positions to measure the β particles. This will allow to get an idea of the count rate in the first experiments and check the simulations.

By counting the ions that remained in the decay trap after t_{meas} one can get an estimate of the number of ions that have not yet decayed. Care should be taken in this approach, since also the ions that could not escape from the trapping potential after β decay will remain in the Penning trap. An important disadvantage of this approach, however, is that one implants radioactive ions onto the measurement MCP which could induce a background in the detected signal.

By scanning the retardation voltage during one measurement cycle it is possible to take ratio's of the different count rates. As an example one could normalize the count rate for each retardation potential by the counts one would get for retardation potential corresponding to the lowest part of the recoil spectrum that is to be fitted. Corrections for the time-dependence of the count rate should be performed in this case.

During first radioactive tests with the set-up the feasibility of the different methods should be tested.

Chapter 9

Future physics goals

During the design phase of the WITCH set-up special attention has been paid to keep the set-up as versatile as possible to allow a wide range of experimental studies besides the search Scalar currents. Apart from using the retardation spectrometer for a reconstruction of the recoil energy spectrum after nuclear β-decay, other types of experiments can be performed with the set-up. Especially the strong focussing of charged particles that is performed by the 9T magnetic field might have good prospects for a number of experiments. In this chapter five possible experiments have been selected and are briefly discussed. This list is however far from exhaustive. For all of them a thorough study is to be made to determine what the prospects are and find the best isotope candidates.

9.1 Tensor current search

Besides the Scalar current search, the set-up can also be used to study Gamow-Teller decays in order to investigate the possible presence of a Tensor component in the weak interaction. From equation 2.4, which expresses the dependence of the a parameter on the Scalar and Tensor interaction strength, it can be seen that the sensitivity to Y_T is a factor of 1/3 reduced with respect to Y_S. Figure 9.1 shows to what Tensor strength an anomaly $\epsilon_{\beta\nu}$ would correspond in the case of a pure Gamow-Teller decay. Measuring the Standard Model prediction $a = -1/3$ with a uncertainty of 1% restricts the Vector strength to about 10 % of the vector strength (at 68%C.L.).

9.2 Mixing ratio Fermi/Gamow-Teller

In the Scalar current search the a-parameter is fitted from the shape of the recoil energy spectrum. If the result is in agreement with the Standard Model prediction, the uncertainty on a yields limits on the coupling constants for the scalar interaction. Assuming however Standard Model predictions ($C_S = C'_S = C_T = C'_T = 0$) the experimental a value can also be used to determine the Fermi to Gamow-Teller mixing ratio y. Rewriting equation 2.4 yields

$$y = \sqrt{\frac{a + \frac{1}{3}}{1 - a}}. \tag{9.1}$$

This dependence is shown in figure 9.2.

The Fermi to Gamow-Teller mixing ratio gives information on the isospin mixing that is present in the initial or final state of $J^\pi \rightarrow J^\pi (J \neq 0)$ β-transitions caused by the electromagnetic interaction or charge dependent parts in the nucleon-nucleon interaction (Raman *et al.*, 1975; Schuurmans and coworkers, 2000; Severijns and coworkers, 1999).

9.3 Charge state distribution after shake-off

In the sixties the charge state distribution of a number of noble gas isotopes has been measured with a set-up similar to the Oak Ridge spectrometer described in subsection 2.2.2, being able to handle isotopes in the gas state.

The WITCH set-up has the capabilities for being a versatile tool to study the charge state distribution after shake-off for a whole range of candidates. With the application of a Penning trap as source container, in principle each isotope can be studied. Furthermore the set-up is designed to handle large number of ions and can accept emission in a solid angle of almost 2π. Finally it should be

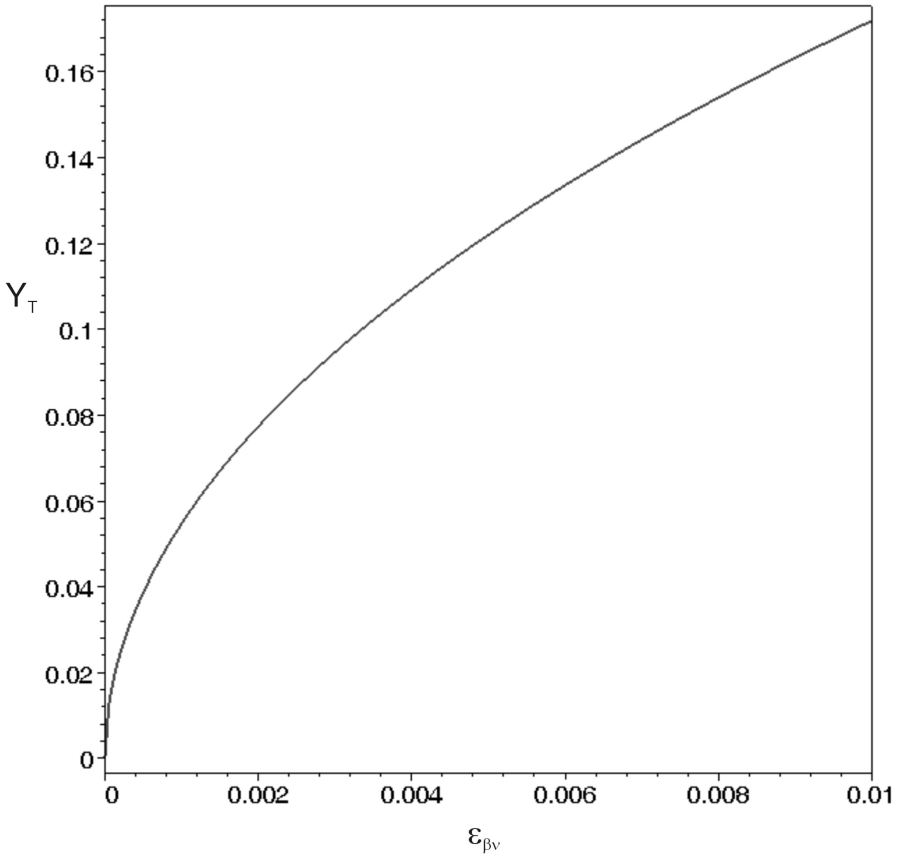

Figure 9.1: Tensor strength Y_T as a function of the $\beta - \nu$ anomaly $\epsilon_{\beta\nu}$.

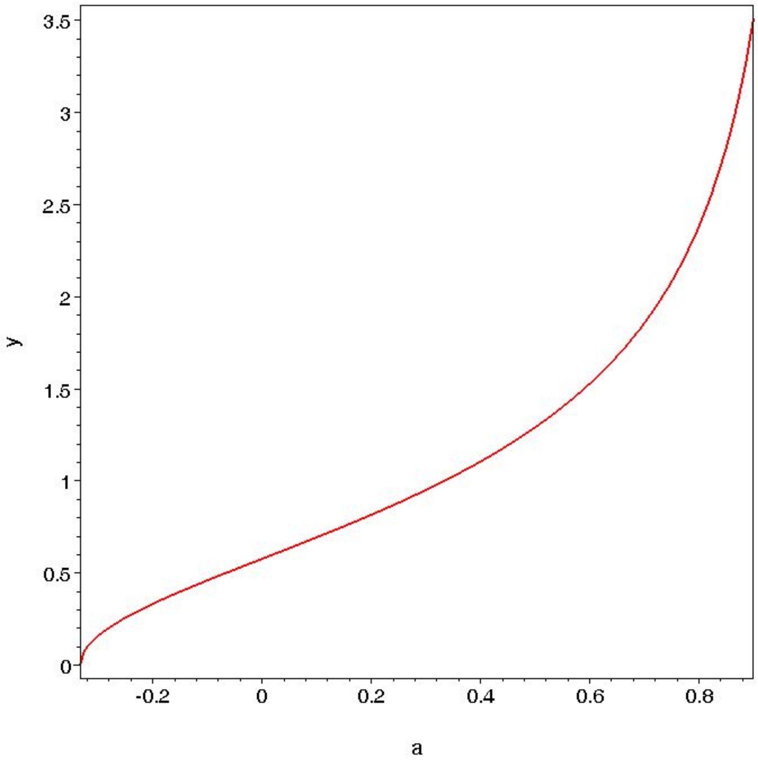

Figure 9.2: Fermi to Gamow-Teller mixing ratio y as a function of the $\beta - \nu$ angular correlation coefficient a.

noted that using the retardation spectrometer also allows to study the charge state distribution after EC-decay, which is not possible if the charge state is determined by a TOF measurement with the β-particle as start trigger.

A WITCH-experiment would differ fundamentally from all other measurements that have been performed as far as known, in the sense that the particles that are stored are ions and not atoms. In this way it is possible to compare the shake-off probabilities of one electron in the ionic case with two electron loss when initially dealing with an atom.

Besides using the retardation spectrometer an alternative approach could be followed using the decay trap. The principle of such an experiment is shown in 9.3. An ion cloud of β-emitters is stored in the decay trap. By applying a sufficiently high potential on the outer end cap electrodes, the daughter ions cannot escape out of the electrostatic potential well. After a storage period of a couple of half-lifes, the ion cloud is then ejected from the trap by applying a strong accelerating electric field. By means of the TOF method the different charge states can be separated. The advantage with respect to the approach with the retardation spectrometer is the simplicity of the method, which does not depend on the systematic effects that influence the response function of the spectrometer and has a recoil angle acceptance of 4π. Furthermore all charge states can be measured in a single shot now and normalization for each ion bunch is obtained by taking ratio's of different charge states. A disadvantage with respect to the retardation spectrometer technique lies in the fact that the measurement time for one ion bunch should be long enough to ensure that the largest fraction of the mother nuclei, that cannot be distinguished from the 1^+ daughter ion, has decayed. This effect is not present in the case of β^- decay where mother and daughter ion always have a different charge. Furthermore no distinction can be made between recoils originating from β^+ and EC decay.

To allow this type of experiment the Penning trap structure should have an open structure at the ejection, which is possible to realize in the case a cylindrical trap. The rest gas pressure should be as low as possible to reduce the effect of charge exchange.

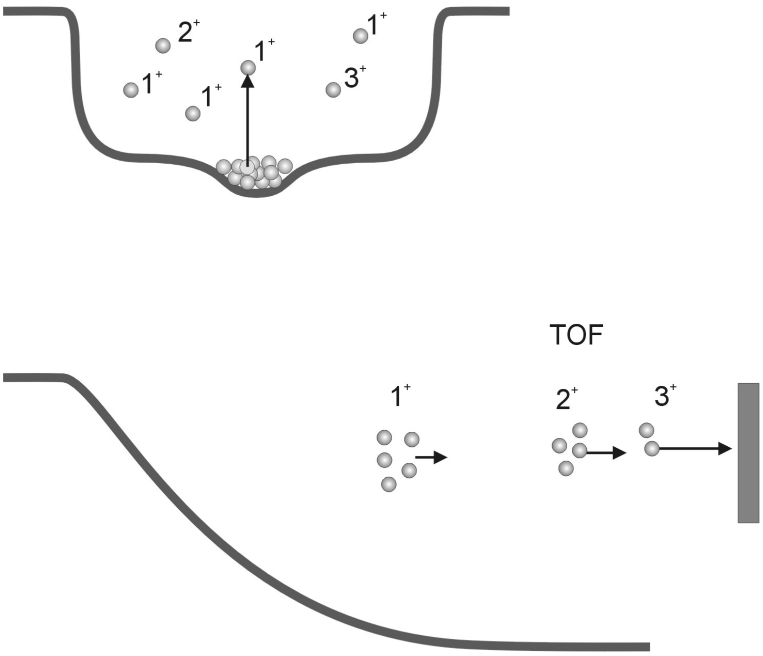

Figure 9.3: Experimental principle to measure the charge state distribution after shake-off by means of a Penning trap.

9.4 In trap spectroscopy

The 9 T magnetic field of the Penning trap provides, apart from the radial confinement of the scattering free source, also a strong focussing effect. Charged particles that are emitted inside a solid angle of 2π, are thus guided in their spiraling motion around the field lines onto a detector, located on the magnetic axis. By placing the detector at a reasonable distance from the Penning trap a possible background of γ rays can be greatly reduced.

This approach can be exploited to carry out precise β spectrum shape measurements. This allows to measure the so-called weak magnetism contribution, as discussed in subsection 1.2.3 and by (Holstein, 1974), that will slightly deform the spectral shape. Also conversion electron spectroscopy can be performed in such a configuration. A first experiment in this respect was performed already with the REXTRAP-set-up (Weissman *et al.*, 2002).

9.5 EC/β^+ ratio

Due to the fact that the WITCH set-up allows to distinguish recoil ions originating from β^+ and EC-decay with the retardation spectrometer, it is possible to measure the EC/β^+ branching ratio. Since the charge state distribution of the two decay branches differs significantly it is necessary to measure the continuous recoil spectrum over its full range. The sum of all charge states gives the EC/β^+ ratio.

Conclusion

This work has presented the development and realization of the WITCH set-up, which is designed to measure the recoil energy spectrum of the daughter ions originating in nuclear β-decay. The spectral shape reveals the angular correlation between the neutrino and the β-particle, which is sensitive to the nature of the weak interaction. A precise determination of the corresponding correlation parameter provides a test of the Vector minus Axial-vector description of the weak interaction and the possible presence of Scalar or Tensor interactions beyond the Standard Model assumptions.

In order to allow detection of the low energy recoil ions, the set-up is equipped with a Penning trap which is in principle able to confine ions of each element in a scattering free environment. This storage device for the radioactive source is coupled to a retardation spectrometer, which performs the energy analysis of the recoil ions and has a solid angle acceptance of almost 2π. The set-up is installed at the ISOLDE/CERN facility, were a large variety of intense radioactive beams is available. The absence of restrictions in the species that can be trapped, allows to select the best isotope for a certain type of experiment.

It has been demonstrated that a determination of the a-parameter with a statistical accuracy of 0.5% requires the experimental recoil spectrum to contain at least 10^8 recoil ions. Taking into account the ISOLDE production yields, a study of the possible candidates to search for a Scalar-type weak interaction proposes to perform a recoil spectrum measurement of the superallowed $0^+ \rightarrow 0^+$ decay of ^{38m}K or the mirror transition of ^{35}Ar. With the current design of the set-up, a measurement will last for about 8 days.

At present, the set-up installation is close to completion and commissioning of the apparatus has started. The first transfer tests with stable $^{39}\mathrm{K}^{+}$-ions have proven that a beam transfer up to the first stage of the vertical beamline can be carried out without significant loss. First injection tests of ions into the cooler trap are scheduled for the beginning of 2004. A first experiment with a radioactive beam is planned for the second half of 2004.

In order to control the systematic effects of the setup affecting the shape of the recoil energy spectrum, a good understanding of the response of the spectrometer is of utmost importance. For this reason, the response function of an ideal spectrometer has been derived analytically. The presently known systematic effects manifest themselves in distortions of the ideal spectrometer response. The study of those effects have revealed the Doppler broadening, due to the initial ion velocity in the Penning trap, to be the most dominant process. Smaller deviations come from the trap potential that prevents a fraction of the recoil ions from leaving the potential well, the radius dependence of the retardation potential in the analysis plane and scattering due to rest gas particles. Most of the response function distortions depend on the properties of the radioactive source, like the energy and density distribution of the ion cloud. Therefore, space charge effects that occur due to Coulomb repulsion when a large number of ions is stored in a Penning trap, should be well understood.

For an experimental study of the systematic effects of the WITCH set-up the electron capture transition is a powerful tool since the corresponding recoil spectrum is a mono-energetic peak. The spectrum that is measured for such a decay would reveal the combined effect of all distortions of the response function.

Already during the design phase, a lot of care was taken to develop a set-up with a broader field of applications than measurements of the $\beta - \nu$ angular correlation. Besides the scattering free source, the strong focussing properties of the Penning trap magnetic field provides interesting possibilities for different types of experiments. Therefore, it can be concluded that also beyond the Scalar and Tensor interaction search, the WITCH set-up allows to explore a broad range of physics questions.

Appendix A

Helicity projection operators

The Dirac equation for relativistic spin-1/2 particles can be written in covariant form as

$$\left(\beta\frac{\partial}{\partial x_4} - i\beta\alpha\cdot\nabla + \frac{m_0c}{\hbar}\right)\psi = 0 \tag{A.1}$$

where $x_4 = ict$ and the matrices β and α defined as in (Wu and Moszkowski, 1966). In the same work general solutions to the Dirac equation can be found.

For a massless particle with momentum pointing along the positive z-axis the solution for both spin and energy states can be calculated to be

$$\begin{aligned}
\psi_{\uparrow}^{+} &= \frac{1}{\sqrt{2}}\begin{pmatrix}1\\0\\1\\0\end{pmatrix},\\
\psi_{\downarrow}^{+} &= \frac{1}{\sqrt{2}}\begin{pmatrix}0\\1\\0\\-1\end{pmatrix},\\
\psi_{\uparrow}^{-} &= \frac{1}{\sqrt{2}}\begin{pmatrix}-1\\0\\1\\0\end{pmatrix},
\end{aligned}$$

$$\psi_\downarrow^- = \frac{1}{\sqrt{2}} \begin{pmatrix} 0 \\ 1 \\ 0 \\ 1 \end{pmatrix}.$$

Using the γ_5-matrix matrix as defined in (Wu and Moszkowski, 1966)

$$\gamma_5 = \begin{pmatrix} 0 & 0 & -1 & 0 \\ 0 & 0 & 0 & -1 \\ -1 & 0 & 0 & 0 \\ 0 & -1 & 0 & 0 \end{pmatrix} \tag{A.2}$$

one can easily show that

$$\begin{aligned} \frac{1+\gamma_5}{2}\psi_\uparrow^+ &= 0, \\ \frac{1+\gamma_5}{2}\psi_\downarrow^+ &= \psi_\downarrow^+, \\ \frac{1+\gamma_5}{2}\psi_\uparrow^- &= \psi_\uparrow^-, \\ \frac{1+\gamma_5}{2}\psi_\downarrow^- &= 0. \end{aligned}$$

Adopting the helicity definition such that it is positive for parallel spin and momentum vector and negative in the antiparallel case one can interpret the operator as a helicity projection operator in the following way: $\frac{1+\gamma_5}{2}$ is the negative helicity state projector for massless Dirac particles in the positive energy state and the positive helicity state projector for massless Dirac particles in the negative energy state. In a similar way it can be calculated that

$$\begin{aligned} \frac{1-\gamma_5}{2}\psi_\uparrow^+ &= \psi_\uparrow^+, \\ \frac{1-\gamma_5}{2}\psi_\downarrow^+ &= 0, \\ \frac{1-\gamma_5}{2}\psi_\uparrow^- &= 0, \\ \frac{1-\gamma_5}{2}\psi_\downarrow^- &= \psi_\downarrow^-. \end{aligned}$$

This means that $\frac{1-\gamma_5}{2}$ is the positive helicity state projector for massless Dirac particles in the positive energy state and the negative helicity state projector for massless Dirac particles in the negative energy state.

Appendix B

Energy considerations in nuclear beta decay

B.1 Available energy

Consider a nucleus ${}^{A}_{Z}X$ that decays by the emission of a β^{+} particle

$$ {}^{A}_{Z}X \rightarrow {}^{A}_{Z-1}X + \beta^{+} + \nu_e \tag{B.1}$$

The energy that is available for the reaction products is determined by the difference in the nuclear mass of initial and final state, i.e.

$$\Delta E = \left[M_{nucl}({}^{A}_{Z}X) - M_{nucl}({}^{A}_{Z-1}X)\right] c^2 = m_e c^2 + T_\beta + p_\nu c + T_r \tag{B.2}$$

However not the nuclear mass but the atomic mass is normally tabulated. So one has to find the relation between the available energy for the reaction products and the atomic mass difference of mother and daughter particle. An important remark one has to make here is that the charge state of the mother and daughter particle changes due to nuclear beta decay. If the mother particle is a 1^{+} ion then the daughter will be a neutral atom (β^{+} decay), a 1^{+} ion (EC-decay) or a 2^{+} ion (β^{-} decay).

Coming back to the β^+ decay of nucleus ${}^A_Z X$, this means that

$$\begin{aligned} M_{at}({}^A_Z X) &= M_{nucl}({}^A_Z X) + Zm_e + E_{bind} \qquad \text{(B.3)} \\ M_{at}({}^{A}_{Z-1} X) &= M_{nucl}({}^{A}_{Z-1} X) + (Z-1)m_e + E'_{bind} \qquad \text{(B.4)} \end{aligned}$$

Inserting this in equation B.2 and neglecting the differences in e^- binding energies, gives

$$\Delta E = \left[M_{at}({}^A_Z X) - M_{at}({}^{A}_{Z-1} X) - m_e\right] c^2 = m_\beta c^2 + T_\beta + p_\nu c + T_r \qquad \text{(B.5)}$$

In a similar way expressions can be derived for β^- and EC decay. Defining ΔM_{at} as the atomic mass difference one can write for the three transitions:

$$\begin{aligned} \beta^+ : \quad & \Delta M_{at} = T_\beta + E_\nu + T_r + 2m_e c^2 \\ \beta^- : \quad & \Delta M_{at} = T_\beta + E_\nu + T_r \\ EC : \quad & \Delta M_{at} = T_\beta + E_\nu + T_r \end{aligned} \qquad \text{(B.6)}$$

This can be written as a function of the Q-value of the transition by replacing ΔM_{at} by Q_{EC} in the case of β^+ and EC-decay and by Q_β^- when dealing with β^- decay.

B.2 Maximal recoil energy

For $\beta^\pm$-decay the maximal recoil energy corresponds to the case in which the momentum of the neutrino is zero and the β-particle takes all kinetic energy. This implies that $\mathbf{p_r} = \mathbf{p}_\beta$. So one finds that

$$T_r^{max} = \frac{p_\beta^2}{2M_{at}({}^{A}_{Z\pm1} X)}, \qquad \text{(B.7)}$$

neglecting the electron mass with respect to the atomic mass in the denominator. Upper signs correspond to β^--, lower sign to β^+-decay. If one combines equation B.6 with B.7 and one neglects the recoil energy T_r in equations B.6 with respect to the decay energies then the expression for the maximal recoil energy can be written as:

$$T_r^{max} = \frac{(\Delta M_{at} c^2 \pm m_e c^2)^2 - m_e^2 c^4}{2M_{at}({}^{A}_{Z\pm1} X) c^2}, \qquad \text{(B.8)}$$

Including the recoil energy in B.6 gives:

$$\begin{aligned} T_r^{max} &= \Delta M_{at}c^2 \pm m_e c^2 + M_{at}({}^{A}_{Z\pm 1}X)c^2 \\ &\quad -\sqrt{\left(M_{at}({}^{A}_{Z\pm 1}X)c^2 \pm m_e c^2\right)^2 + 2M_{at}({}^{A}_{Z\pm 1}X)c^2 \Delta M_{at}c^2}. \end{aligned} \tag{B.9}$$

In the case of the β^+ decay of ^{26}Al the recoil correction to the maximal recoil energy (280.7 eV) is 43 meV or a relative correction of $1.5 \cdot 10^{-4}$

For EC decays the energy of the two decay products have a fixed energy. The recoil energy is given by

$$T_r = \frac{p_\nu^2}{2M_{at}({}^{A}_{Z\pm 1}X)}. \tag{B.10}$$

Neglecting the recoil energy in B.6 gives:

$$T_r = \frac{(\Delta M_{at}c^2)^2}{2M_{at}({}^{A}_{Z-1}X)c^2}. \tag{B.11}$$

Including recoil order effect implies:

$$T_r^{max} = \Delta M_{at}c^2 + 1 - \sqrt{\left(M_{at}({}^{A}_{Z\pm 1}X)c^2 + 1\right)^2 - (\Delta M_{at}c^2)^2} \tag{B.12}$$

Appendix C

Isotope candidates

This appendix contains a table with more data on the superallowed transitions that are mentioned in table 3.3. This data is intended to allow a more detailed comparison between the different candidates. Besides the transition of interest, located in the first row for each isotope, the decay branch with the highest recoil energy endpoint is also indicated. This allows to determine that part of the recoil energy spectrum, that is undisturbed.

mother	state	$t_{1/2}$ (s)	yield (part/s)	daughter	state	$t_{1/2}$ (s)	M_{at} (MeV)	ΔE (MeV)	$E_r(max)$ (eV)	P_{EC} %	BR %
^{26}Al	isom	6.345	$3.95{\cdot}10^4$	^{26}Mg	gs	stable	$2.42 \cdot 10^4$	4.232	280.7	0.083	100
	gs	$7.4\ 10^5$y			excit	476 fs		2.20	53.2		97.3
^{34}Cl	gs	1.525	$1.26 \cdot 10^3$	^{34}S	gs	stable	$3.16 \cdot 10^4$	5.492	387.9	0.078	100
	isom	1920	$7.9 \cdot 10^7$		excit	325 fs		3.511	138		28.5
^{38}K	isom	0.923	$6.3 \cdot 10^6$	^{38}Ar	gs	stable	$3.54 \cdot 10^4$	6.0435	429.1	0.082	100
	gs	458	$7.9 \cdot 10^7$		excit	470 fs		3.7456	144.2		99.8
					gs	stable		5.9131	408.9		<0.6
^{42}Sc	gs	0.6813	0	^{42}Ca	gs	stable	$3.91 \cdot 10^4$	6.425	444.2	0.095	99.9926
	excit	61.7	0		excit	250 fs		3.8528	139.5		100
^{46}V	gs	0.42237	0	^{46}Ti	gs	stable	$4.28 \cdot 10^4$	7.0514	496.6	0.096	100
^{50}Mn	gs	0.283	$7.6 \cdot 10^5$	^{50}Cr	gs	$1.8\ 10^{17}$y	$4.65 \cdot 10^4$	7.633	542.3	0.104	99.9
	isom	105	$2.9 \cdot 10^5$		excit	1.25 ps		4.6983	185.6		8.0
^{54}Co	gs	0.193	0	^{54}Fe	gs	stable	$5.03 \cdot 10^4$	8.24309	592.3	0.104	100
	isom	88.8	0		excit	1.215 ns		5.49289	244.4		8.0
^{33}Cl	gs	2.511	$1.41 \cdot 10^2$	^{33}S	gs	stable	$3.07 \cdot 10^4$	5.583	414.5	0.074	98.6
					excit	1.17 ps		4.742	287.1		0.48
^{35}Ar	gs	1.775	$2.1 \cdot 10^7$	^{35}Cl	gs	stable	$3.26 \cdot 10^4$	5.9653	452.6	0.072	98.1
					excit	150 fs		4.7458	271.3		1.23

Table C.1: Information on candidate isotopes. ΔE is the energy difference between the initial and final nuclear state. Lifetimes, atomic masses, decay energies and branching ratio's (BR) are obtained from Firestone and Shirley (1996), P_{EC} from Hardy *et al.* (1990) (except for ^{33}Cl and ^{35}Ar which are from Navilat-Cuncic *et al.* (1991)) and yield information from ISOLDE collaboration (2003)

Appendix D

Electrodes

This appendix gives and overview of the different electrodes in the beamline system as well as the voltages that have been applied for the simulations. In the case of the horizontal beamline the voltages that have been applied during the beamline test are also listed. The positioning of the electrodes is schematically shown in figures **??**. The abbreviations used in the names of the electrodes are explained further down.

- HB: horizontal beamline
- VB: vertical beamline
- TR: trap region
- SP: spectrometer

- KICK: kicker plate
- BEND: bender electrode
- EINZ: central einzellens electrode
- STEE: steerer plate
- DRIF: Drift electrode

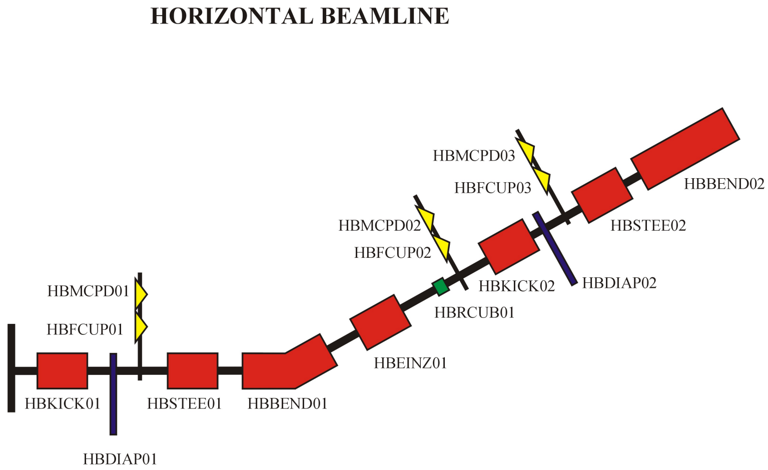

Figure D.1: Schematic overview of the horizontal beamline components.

- RETA: retardation electrode
- PDTU: pulsed drift tube
- ACCE: acceleration electrodes

- U: up
- D: down
- L: left
- R: right

- FCUP: Faraday cup
- MCPD: MCP detector
- RCUB: rotating cube
- DIAP: diaphragm strip
- IONS: ion source

Table D.1: Overview of all beam optical components of the horizontal beamline with code name and specifications.

Name	Voltage (Sim) (kV)	Voltage (exp) (kV)	Power supply
REX ejec stee hor	0	0	/
REX ejec stee ver	0	0	/
REX ejec kick hor	0	0.120	/
REX ejec kick ver	0	-0.180	/
REXTRAP-lens	28.5	30.5	
HBKICK01L	-1.41	-2	ISEG EHQ 16cha 1
HBKICK01R	1.41	2.1	ISEG CPS-P 7 kV
HBSTEE01U	0	0	Elec. worksh. KUL +/-2 kV
HBSTEE01D	0	0.150	Elec. worksh. KUL +/-2 kV
HBBEND01L	-4.495	-4.235	ISEG CPS-N 7 kV
HBBEND01R	4.495	4.235	ISEG CPS-P 7 kV
HBEINZ01	23	30	Spellmann 30 kV
HBKICK02U	-1.42	-2	ISEG EHQ 16cha 2
HBKICK02D	1.42	2	ISEG CPS-P 7 kV
HBSTEE02L	0	0	Elec. worksh. KUL +/-2 kV
HBSTEE02R	0	0	Elec. worksh. KUL +/-2 kV
HBBEND02U	-4.74	-4.45	ISEG CPS-N 7 kV
HBBEND02D	4.74	4.45	ISEG CPS-P 7 kV

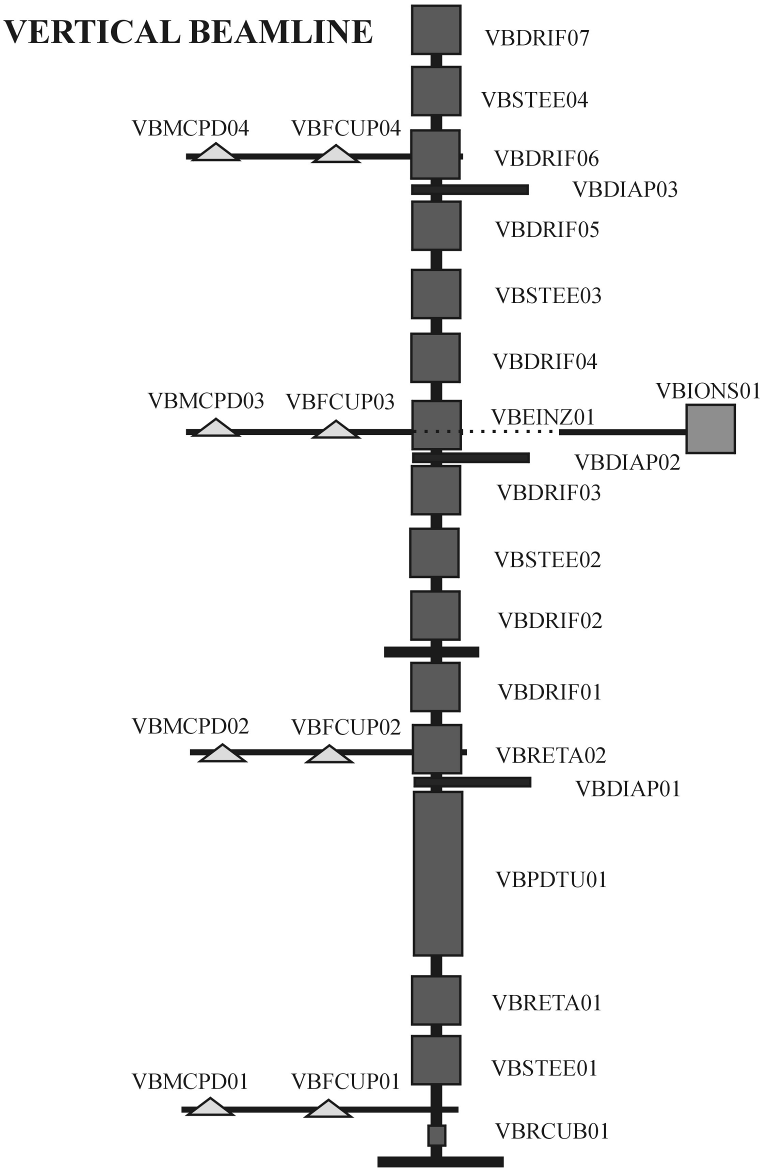

Figure D.2: Schematic overview of the vertical beamline components.

Table D.2: Overview of all beam optical components of the vertical beamline with code name and specifications.

Name	Voltage (Sim) (kV)	Power supply
VBSTEE01L	0	Elec. worksh. KUL +/-2 kV
VBSTEE01R	0	Elec. worksh. KUL +/-2 kV
VBSTEE01U	0	Elec. worksh. KUL +/-2 kV
VBSTEE01D	0	Elec. worksh. KUL +/-2 kV
VBRETA01	40	Spellmann SL50P10/220/LR/LL(20)
VBPDTU01	52	FUG HCN 6.5M 65000
	-8	ISEG CPS-N 10 kV
VBRETA02	-2.5	ISEG CPS-N 7 kV
VBDRIF01	-2	ISEG EHQ 16cha 3
VBDRIF02	-1.5	ISEG EHQ 16cha 4
VBSTEE02L	-1.5	Elec. worksh. KUL -5 kV
VBSTEE02R	-1.5	Elec. worksh. KUL -5 kV
VBSTEE02U	-1.5	Elec. worksh. KUL -5 kV
VBSTEE02D	-1.5	Elec. worksh. KUL -5 kV
VBDRIF03	-1.5	ISEG EHQ 16cha 5
VBEINZ01	-1.5	ISEG EHQ 16cha 6
VBDRIF04	-0.4	ISEG EHQ 16cha 7
VBSTEE03L	-1.5	Elec. worksh. KUL -5 kV
VBSTEE03R	-1.5	Elec. worksh. KUL -5 kV
VBSTEE03U	-1.5	Elec. worksh. KUL -5 kV
VBSTEE03D	-1.5	Elec. worksh. KUL -5 kV
VBDRIF05	-1.5	ISEG EHQ 16cha 8
VBDRIF06	-1.5	ISEG EHQ 16cha 9
VBSTEE04L	-1.5	Elec. worksh. KUL -5 kV
VBSTEE04R	-1.5	Elec. worksh. KUL -5 kV
VBSTEE04U	-1.5	Elec. worksh. KUL -5 kV
VBSTEE04D	-1.5	Elec. worksh. KUL -5 kV
VBDRIF07	-1.5	ISEG EHQ 16cha 10
VBDRIF08	-1.5	ISEG EHQ 16cha 11
VBDRIF09	-1.5	ISEG EHQ 16cha 12
VBDRIF10	-1.5	ISEG EHQ 16cha 13
VBDRIF11	-1.5	ISEG EHQ 16cha 14
VBDRIF12	-1.5	ISEG EHQ 16cha 15

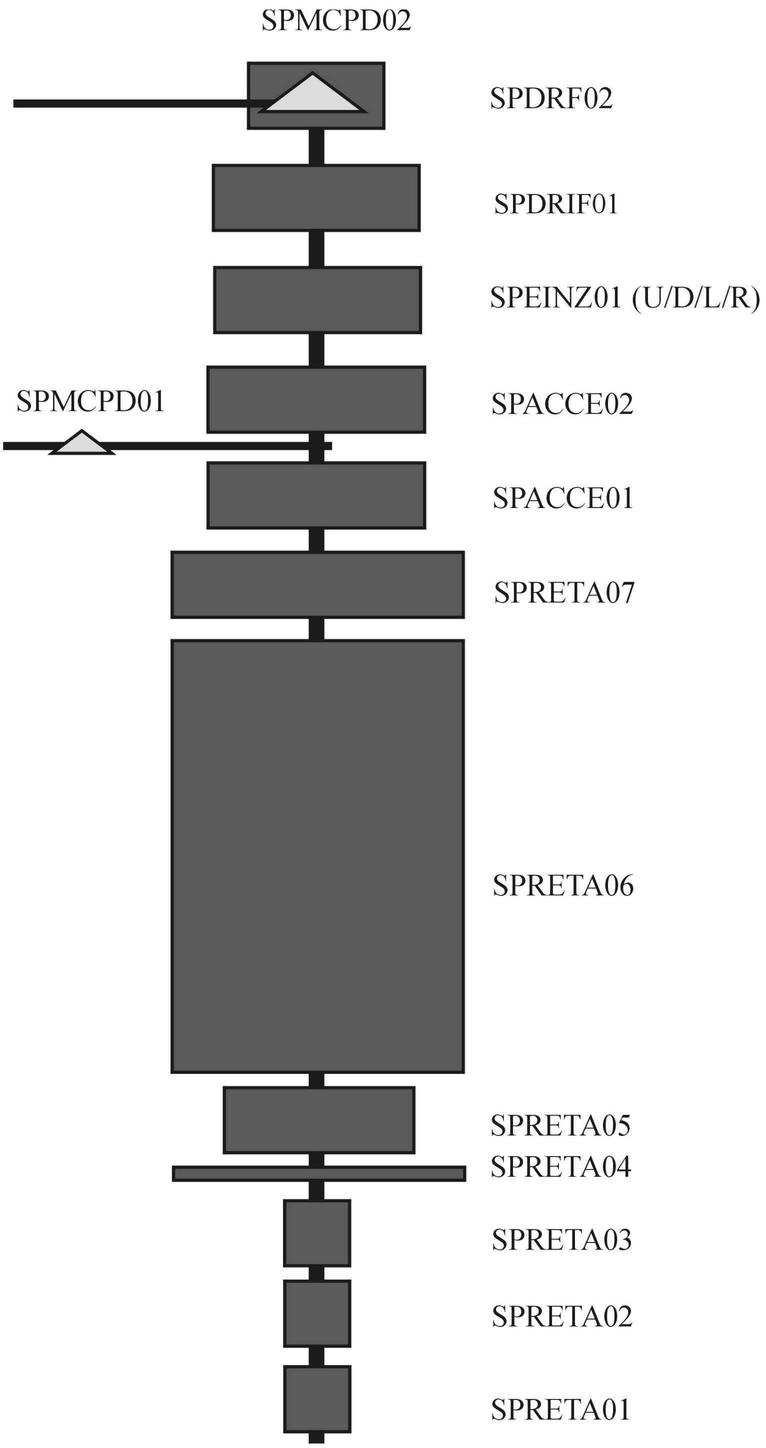

Figure D.3: Schematic overview of the retardation spectrometer components.

Table D.3: Dimensions and voltages being applied on the retardation spectrometer electrodes.

Electrode name	Voltage(sim) [% of U_{ret}]	Power supply
SPRETA01	0	ISEG NHQ-cha1
SPRETA02	30	ISEG NHQ-cha1
SPRETA03	60	ISEG NHQ-cha1
SPRETA04	80	ISEG NHQ-cha1
SPRETA05	80	ISEG NHQ-cha1
SPRETA06	100	ISEG NHQ-cha1
SPRETA06	100	ISEG NHQ-cha1
Electrode name	**Voltage(sim) [kV]**	**Power supply**
SPACCE01	-2	ISEG EHQ 16cha 16
SPACCE02	-10	
SPEINZ02	-0.2	ISEG NHQ-cha2
SPDRIF01	-10	
SPDRIF02	-10	

Appendix E

Vacuum system

A schematic overview of the vacuum system of the WITCH set-up can be found in figure E.1. The upper part of the vertical beamline, the traps and the spectrometer form one big vacuum section. Since the biggest volume is part of the spectrometer, this vacuum section is called spectrometer vacuum section.

- UHVV: UHV valve
- PREV: Pre-vacuum valve
- TURP: Turbo pump
- ROTP: Rotary pump
- PIRA: Pirani gauge
- PENN: Penning gauge

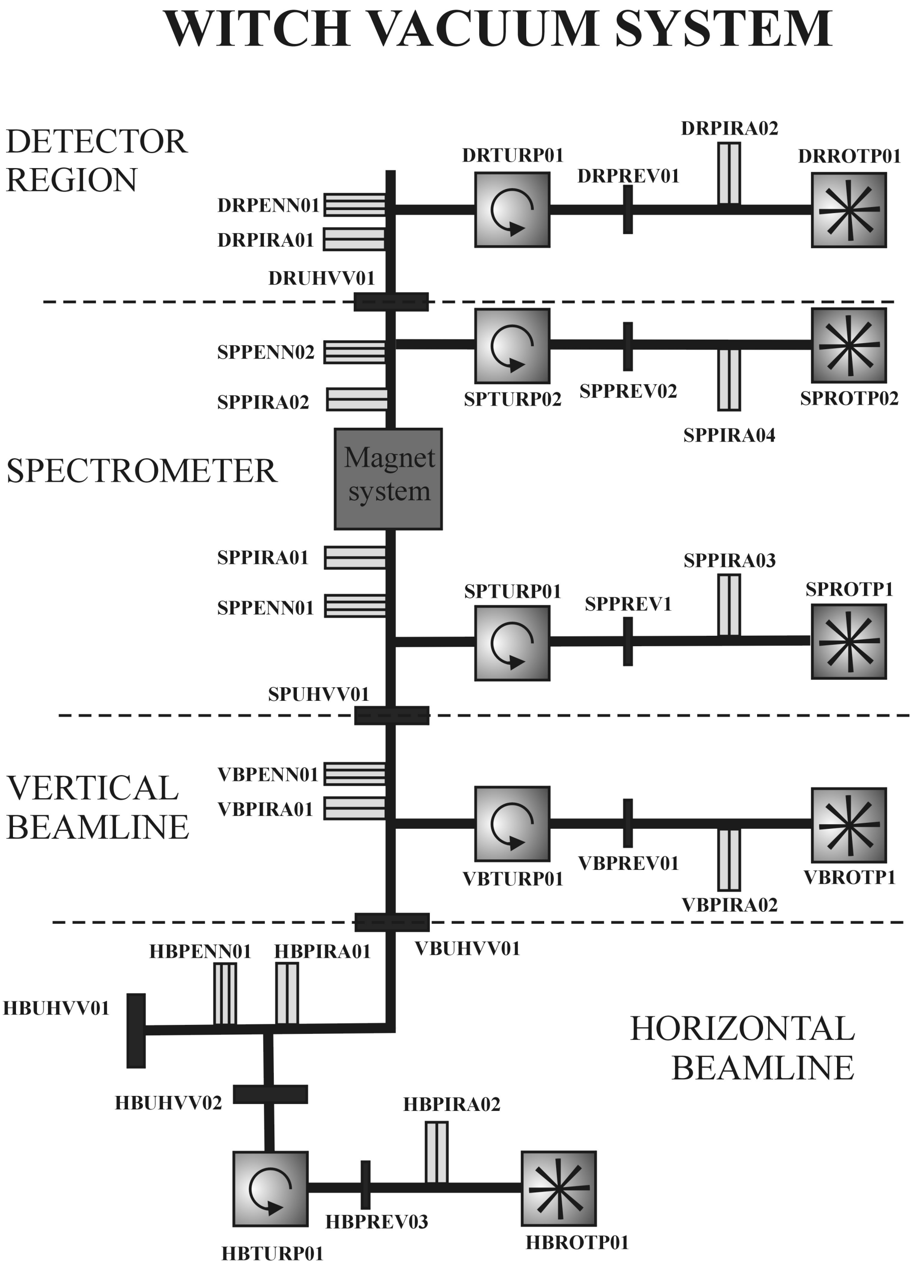

Figure E.1: Vacuum system of the WITCH set-up

Bibliography

Adelberger, E. G., C. Ortiz, A. García, H. E. Swanson, M. Beck, O. Tengblad, M. J. G. Borge, I. Martel, H. Bichsel, and the ISOLDE Collaboration, 1999, Phys. Rev. Lett. **83**, 1299.

Alheit, R., X. Z. Chu, M. Hoefer, M. Holzki, and G. Werth, 1997, Phys. Rev. A **56**(5), 4023.

Allen, J. S., R. L. Burman, W. B. Herrmannsfeld, P. Stähelin, and T. H. Braid, 1959, Phys. Rev. **116**, 134.

Ames, F., 2003, Private communications.

Ames, F., G. Bollen, O. Forstner, G. Huber, D. Habs, and K. Reisinger, 2002, Contribution to the 3^{rd} International Conference on Trapped Charged Particles and Fundamental Interactions, Wildbad Kreuth, Aug 25-30 2002 .

Ames, F., G. Bollen, G. Huber, P. Schmidt, and the REX-ISOLDE collaboration, in *Proceedings of the Exotic Nuclei and Atomic Masses, Bellaire, USA, 1998, AIP Conference Proceedings 445 (1998), 927-932*.

Ames, F., P. Schmidt, O. Forstner, G. Bollen, O. Engels, D. Habs, G. Huber, and the REX-ISOLDE collaboration, 2001, Hyp. Int. **132**, 469.

Batkin, I. S., K. A. Bushahma, T. Churakova, and S. L. Demakov, 1992, J. Phys. G **18**, 1995.

Beamson, G., H. Q. Porter, and D. W. Turner, 1980, J. Phys. E **13**, 64.

Beck, D., 1997, *Massenbestimmung instabiler Isotope der Seltenen Erden um* 146*Gd mit dem ISOLTRAP-spektrometer*, Ph.D. thesis, Johannes Gutenberg Universität Mainz.

Beck, D., F. Ames, M. Beck, G. Bollen, B. Delauré, P. Schuurmans, S. Schwarz, P. Schmidt, N. Severijns, and O. Forstner, 2001, Hyp. Int. **132**, 473.

Beck, M., F. Ames, D. Beck, G. Bollen, B. Delauré, V. V. Golovko, V. Y. Kozlov, I. S. Kraev, A. Lindroth, T. Phalet, W. Quint, P. Schuurmans, *et al.*, 2003, Nucl. Instr. and Meth. in Phys. Res. A **503**, 567.

Behr, J., 2003a, Private communications.

Behr, J. A., 2003b, Nucl. Instr. and Meth. in Phys. Res. B **204**, 526.

Blaum, K., 2003, Private communications.

Blaum, K., G. Audi, D. Beck, G. Bollen, F. Herfurth, A. Kellerbauer, H.-J. Kluge, E. Sauvan, S.Schwarz, and the ISOLDE Collaboration, 2003, submitted for publication .

Bollen, G., S. Becker, H.-J. Kluge, M. König, R. B. Moore, T. Otto, H. Raimbault-Hartmann, G. Savard, L. Schweikhard, H. Stolzenberg, and the ISOLDE Collaboration, 1996, Nucl. Instr. Meth. Phys. Res. A **368**, 675.

Bollinger, J. J., D. J. Heinzen, F. L. Moore, W. M. Itano, and D. J. Wineland, 1993, Phys. Rev. A **48**(1), 525.

Brioullin, L., 1945, Phys. Rev. **67**, 260.

Brown, L. S., and G. Gabrielse, 1986, Rev. Mod. Phys. **58**, 233.

Byrne, J., P. G. Dawber, M. G. D. van der Grinten, C. G. Habeck, F. Shaikh, J. A. Spain, R. D. Scott, C. A. Baker, K. Green, and O. Zimmer, 2002, J. Phys. G: Nucl. Part. Phys. **28**, 1325.

Carlson, T. A., 1963a, Phys. Rev. **130**, 2361.

Carlson, T. A., 1963b, Phys. Rev. **131**, 676.

Carlson, T. A., C. W. Nestor Jr., and T. C. Tucker, 1968, Phys. Rev. **169**, 27.

Carlson, T. A., F. Pleasonton, and C. H. Johnson, 1963, Phys. Rev. **129**, 2221.

Coeck, S., 2003, *Karakterisering van detector en ionenbron voor het WITCH experiment*, Master's thesis, Katholieke Universiteit Leuven.

Cowan, C. L., F. Reines, F. B. Harrison, H. W. Kruse, and A. D. McGuire, 1956, Science **124**, 103.

Dahl, D. A., 1995, *SIMION 3D 6.0: users manual* (Princeton Electronic Systems, Inc.).

Delahaye, P., 2002, *Etudes et tests preliminaires a une mesure de la correlation angulaire $\beta - \nu$ dans la desintegration du noyau ^{6}He a l'aide d'un piege de Paul*, Ph.D. thesis, Université de Caen/Basse Normandie.

Delahaye, P., G. Ban, D. Durand, V. Kumar, C. L. Brun, E. Liénard, F. Mauger, O. Naviliat, J. Szerypo, and B. Tamain, 2000, Hyp. Int. **132**, 479.

Dezfuli, A. M. G., R. B. Moore, and P. Varfalvy, 1996, Nucl. Instr. and Meth. in Phys. Res. A **368**, 611.

Driscoll, C. F., J. H. Malmberg, and K. S. Fine, 1988, Phys. Rev. Lett. **60**(13), 1290.

Dubin, D. H. E., and T. M. O'Neil, 1999, Rev. Mod. Phys. **71**(1), 87.

Egorov, V., C. Brianç, V. Brudanin, J.Dionisio, J. Deutsch, V. Gorozhankin, Y. Gurov, R.Prieels, V. Sandukovsky, N.Severijns, M.Simoes, Y. Shitov, *et al.*, 1997, Nucl. Phys. A **621**, 745.

Egorov, V., O. Naviliat-cuncic, G. Auger, G. Ban, M. Beck, C. Brianç, V. Brudanin, P.Delahaye, J. Deutsch, D. Durand, F.Landré, N.Lecesne, *et al.*, 2001, proposal for an experiment at GANIL .

Ellis, H. W., E. W. McDaniel, D. L. ALbritton, L. A. Viehland, S. L. Lin, and E. A. Mason, 1978, Atomic Data and Nuclear Data Tables **22**, 197.

Ellis, H. W., R. Y. Pai, E. W. McDaniel, E. A. Mason, and L. A. Viehland, 1976, Atomic Data and Nuclear Data Tables **17**, 177.

Ellis, H. W., M. G. Thackston, E. W. McDaniel, and E. A. Mason, 1984, Atomic Data and Nuclear Data Tables **31**, 113.

Feinberg, E. L., 1941, J. Phys. (USSR) **4**, 423.

Firestone, R. B., and V. S. Shirley, 1996, *Table of isotopes, eigth edition* (John Wiley and Sons (New York)).

Forstner, O., 2001, *Beam-Preparation with REXTRAP for the REX-ISOLDE Experiment*, Ph.D. thesis, Technischen Universität Wien.

Gamow, G., and E. Teller, 1936, Phys. Rev. **49**, 895.

García, A., E. G. Adelberger, C. Ortiz, H. E. Swanson, M. Beck, O. Tengblad, M. J. G. Borge, I. Martel, H. Bichsel, and the ISOLDE Collaboration, 2000, Hyp. Int. **129**, 237.

Gell-Mann, M., 1958, Phys. Rev. **111**, 362.

Glashow, S. L., 1961, Nucl. Phys. **22**, 579.

Glück, F., 1998, Nucl. Phys. A **628**, 493.

Glück, F., 2004, to be published .

Glück, F., S. Baessler, J. Byrne, M. G. D. van der Grinten, F. J. Hartmann, W. Heil, I. Konorov, G. Petzoldt, Y. Sobolev, and O. Zimmer, 2003, to be published .

Gorelov, A., J. A. Behr, D. Melconian, M. Trinczek, P. Dubé, O. Häusser, U. Giesen, K. P. Jackson, T. Swanson, J. M. D'Auria, M. Dombsky, G. Ball, *et al.*, 2000, Hyp. Int. **127**, 373.

Groom, D. E., and coworkers, 2000, Eur. Phys. J. C **15**, 1.

Grünert, J., 2002, *Ultracold Metastable Calcium Atoms in a Bi-chromatic Magneto-Optical Trap*, Ph.D. thesis, Universität Hamburg.

Habs, D., and coworkers, 2000, Hyp. Int. **129**, 43.

Hardy, J. C., and I. S. Towner, 1975, Nucl. Phys. A **254**, 221.

Hardy, J. C., I. S. Towner, V. T. Koslowsky, E. Hagberg, and H. Scheming, 1990, Nucl. Phys. A **509**, 429.

Herfurth, F., J. Dilling, A. Kellerbauer, G. Bollen, S. Henry, H.-J. Kluge, E. Lamour, D. Lunney, R. B. Moore, C. Scheidenberg, S. Schwarz, G. Sickler, *et al.*, 2001, Nucl. Instr. and Meth. in Phys. Res. A **469**, 254.

Holstein, B. R., 1974, Rev. Mod. Phys. **46**, 789.

Holstein, B. R., 1984, Phys. Rev. C **29**, 623.

Holstein, B. R., and S. B. Treiman, 1971, Phys. Rev. C **3**, 1921.

’t Hooft, G., 1971a, Nucl. Phys. **B33**, 173.

’t Hooft, G., 1971b, Nucl. Phys. **B35**, 167.

Humphries Jr., S., 1990, *Charged Particle Beams* (John Wiley and Sons, New York).

Intemann, R. L., 1983, Phys. Rev. A **28**, 1288.

ISOLDE collaboration, 2003, Sc isolde production yiels, URL `http://isolde.web.cern.ch/ISOLDE/`.

Jackson, J. D., 1975, *Classical electrodynamics* (John Wiley and Sons, New York).

Jackson, J. D., S. B. Treiman, and H. W. Wyld, 1957a, Nucl. Phys. **4**, 206.

Jackson, J. D., S. B. Treiman, and H. W. Wyld, 1957b, Phys. Rev. **106**, 517.

Johnson, C. H., F. Pleasonton, and T. A. Carlson, 1963, Phys. Rev. **132**, 1149.

Kluge, H.-J., 2002, Nucl. Phys. A **701**, 495c.

Kofoed-Hansen, O., 1954, Dan. Mat. Fys. Medd. **28**(9), 1.

König, M., G. Bollen, H.-J. Kluge, T. Otto, and J. Szerypo, 1995, Int. J. Mass. Spectrom. Ion. Proc. **142**, 95.

Kraus, C., J. Bonn, B. Bornschein, L. Bornschein, B. Flatt, A. Kovalik, B. Müller, E. W. Otten, T. Thümmler, J. P. Schall, and C. Weinheimer, 2004, Eur. Phys. J. (accepted for publication) .

Kruit, P., and F. H. Read, 1983, J. Phys. E **16**, 313.

Kuckein, M., 2002, *Phase-locked magnetron excitation and implementation of a SWIFT-cleaning mechanism at ISOLTRAP*, Master's thesis, Technische Universitat Munchen.

Kugler, E., 2000, Hyp. Int. **129**, 23.

Kugler, E., D. Fiander, B. Johnson, H. Haas, A. Przewloka, H. L. Ravn, D. J. Simon, and K. Zimmer, 1992, Nucl. Instr. Meth. Phys. Res. **70**, 41.

Lai, C. H., 1981, *Gauge Theory of Weak and Electromagnetic Interactions* (World Scientific, Singapore).

Lee, T. D., and C. N. Yang, 1956, Phys. Rev. **104**, 254.

Lobashev, V. M., V. N. Aseev, A. I. Belesev, A. I. Bewrlev, E. V. Geraskin, A. A. Golubev, O. V. Kazachenko, Y. E. Kuznetsov, R. P. Ostroumov, L. A. Rivkis, B. E. Stern, N. A. Titov, *et al.*, 1999, Phys. Lett. B **460**, 227.

Lobashev, V. M., and P. E. Spivak, 1985, Nucl. Instr. and Meth. in Phys. Res. A **240**, 305.

Moore, R. B., A. M. G. Dezfuli, P. Varfalvy, and H. Zhao, 1995, Phys. Scr. **T59**, 93.

Morse, P. M., and H. Feshbach, 1963, *Methods of Theoretical Physics* (McGraw-Hill, New York).

Navilat-Cuncic, O., T. A. Girard, J. Deutsch, and N. Severijns, 1991, J. Phys. G **17**, 919.

Ormand, W. E., B. A. Brown, and B. R. Holstein, 1989, Phys. Rev. C **40**, 2914.

Osipowicz, A., and coworkers, 2001, Technik und Umwelt Wissenschaftliche Berichte FZKA 6691 .

Paasche, P., T. Valenzuela, D. Biswas, C. Angelescu, and G. Werth, 2002, Eur. Phys. J. D **18**, 295.

Penning, F. M., 1936, Physica(Utrecht) **3**, 873.

Picard, A., H. Backe, H. Barth, J. Bonn, B. Degen, T. Edingen, R. Haid, A. Hermanni, P. Leiderer, T. Loeken, A. Molz, R. B. Moore, *et al.*, 1992, Nucl. Instr. and Meth. in Phys. Res. B **63**, 345.

Press, W. H., and coworkers, 1996, *Numerical Recipies in C: The Art of Scientific Computing* (Cambridge Univ. Press., Cambridge).

Raimbault-Hartmann, H., D. Beck, G. Bollen, M. Konig, H.-J. Kluge, E. Schark, J. Stein, S. Schwarz, and J. Szerypo, 1997, Nucl. Instr. and Meth. in Phys. Res. B **126**, 378.

Raman, S., T. A. Walkiewicz, and H. Behrens, 1975, At. Data and Nucl. Data Tables **16**, 451.

Reisinger, K., 2002, *Emittance Measurements on the Sideband Cooling Technique and Introduction of the Rotating Wall Cooling Technique at REXTRAP*, Master's thesis, Technische Universitat München.

Savard, G., R. C. Barber, F. Buchinger, J. E. Crawford, X. Feng, S. Gulick, G. Hackman, J. C. Hardy, J. K. P. Lee, R. B. Moore, K. S. Sharma, and J. Uusitalo, 1999, Nucl. Phys. A **654**, 961c.

Savard, G., S. Becker, G. Bollen, H.-J. Kluge, R. B. Moore, T. Otto, L. Schweikhard, H. Stolzenberg, and U. Wiess, 1991, Phys. Lett. A **158**, 247.

Schardt, D., and K. Riisager, 1993, Z. Phys. A **345**, 265.

Schmidt, P., 2001, *REXTRAP: Ion Accumulation, Cooling and Bunching for REX-ISOLDE*, Ph.D. thesis, Johannes Gutenberg Universität Mainz.

Schmidt, P., F. Ames, G. Bollen, O. Forstner, G. Huber, M. Oinonen, J. Zimmer, and R.-I. collaboration, 2002, Nucl. Phys. A **701**, 550c.

Schnatz, H., G. Bollen, Dabkiewicz, P. Egelhof, F. Kern, H. Kalinowsky, L. Schweikhard, and H. Stolzenberg, 1986, Nucl. Instr. Meth. Phys. Res. A **251**, 17.

Schuurmans, P., and coworkers, 2000, Nucl. Phys. **A 672**, 89.

Scielzo, N., 2003, *Measurement of the β-ν Corrleation in Laser Trapped ^{21}Na*, Ph.D. thesis, University of California, Berkeley.

Scielzo, N. D., S. J.Freedman, B. K. Fujikawa, and P. A. Vetter, 2003, Phys. Rev. A **68**, 022716.

Severijns, N., 2003, Private communications.

Severijns, N., M. Beck, and O. Naviliat-Cuncic, 2004, Rev. Mod. Phys., to be published .

Severijns, N., and coworkers, 1999, Isospin mixing in $N \approx Z$ nuclei.

Sirlin, A., 1967, Phys. Rev. **164**, 1767.

Snell, A. H., and F. Pleasonton, 1955, Phys. Rev. **100**, 1396.

Snell, A. H., and F. Pleasonton, 1957, Phys. Rev. **107**, 740.

Superconductivity, O. I., 2002, *Superconducting Magnet System: Operators Handbook* (Oxford Instruments).

Towner, I. S., and J. C. Hardy, 1995, *Symmetries and Fundamental Interactions in Nuclei* (W.C. Haxton and E.M. Henley (World Scienctific)).

Towner, I. S., and J. C. Hardy, 2003, J.Phys.G **29**, 197.

Van Dyck Jr., R. S., P. B. Schwinberg, and H. G. Dehmelt, 1984, *Atomic Physics 9* (World Scientific, Singapore).

Viehland, L. A., and E. A. Mason, 1995, Atomic Data and Nuclear Data Tables **60**, 37.

Vorobel, V., C. Brianç, V. Egorov, J. Deutsch, R. Prieels, N. Severijns, Y. Shitov, C. Vieu, T. Vylov, I. Yutlandov, and S. Zaparov, 2003, Eur. Phys. J. A **16**, 139.

Weinberg, S., 1967, Phys. Rev. Lett. **19**, 1264.

Weissman, L., F. Ames, J. Äysto, O. Forstner, K. Reisinger, and S. Rinta-Antila, 2002, Nucl. Instr. Meth. Phys. Res. A **492**, 451.

Wilkinson, D. H., 2000, Eur. Phys. J. **A 7**, 307.

Wilkinson, D. H., and B. E. F. Macefield, 1974, Nucl. Phys. A **232**, 58.

Wineland, D. J., W. M. Itano, J. C. Bergquist, and R. G. Hulet, 1987, Phys. Rev. A **36**, 2220.

Wu, C. S., E. Ambler, R. W. Hayward, D. D. Hoppes, and R. P. Hudson, 1957, Phys. Rev. **105**, 1413.

Wu, C. S., and S. A. Moszkowski, 1966, *Beta decay* (John WIley and Sons, New York).

Zimmer, O., J. Byrne, M. G. D. van der Grinten, W. Heil, and F. Glück, 2000, Nucl. Instr. and Meth. in Phys. Res. A **440**, 548.